UNIVERSITAT POLITÈCNICA DE CATALUNYA BARCELONATECH

Advancing in the characterization of coastal aquifers. A multimethological approach based on fiber optics distributed temperature sensing

Laura del Val Alonso

Universitat Politècnica de Catalunya

Doctoral Thesis

Advancing in the characterization of coastal aquifers.

A multimethological approach based on fiber optics distributed temperature sensing

Author:
Laura del Val Alonso

Supervisor:
Dr. Albert FOLCH
Dr. Maarten SAALTINK

A thesis submitted in fulfillment of the requirements for the degree of Doctor of Philosophy in Geotechnical Engineering

in the

Groundwater Hydrology Research Group
Department of Environmental and Civil Engineering

May 6, 2020

This thesis is part of the project MEDISTRAES (Mixing and Dispersion in the Transport of Energy and Solutes) funded by the Spanish Government through the project grants CGL2013-48869-C2-1-R/2-R and CGL2016-77122-C2-1-R/2-R. And it has been funded by the Spanish Governement through the FPI fellowship BES-2014-069329.

I would like to thank SIMMAR (Serveis Integrals de Manteniment del Maresme) and the Consell Comarcal del Maresme for allowing us to use their facilities for the construction of the field site, and to assist us through out the process.

Finally, I would like to thank Sensornet (UK) for their trust, support and advise, through the process of acquiring, installing and deploying their Oryx + Distributed Temperature Sensor unit.

Laura del Val Alonso
"Advancing in the characterization of coastal aquifers. A multimethological approach based on fiber optics distributed temperature sensing"
Ph.D. Thesis, May, 2020
External reviewers: Dr. Vincent Post, Dr. Carlos Duque and Dr. Christoph Schüth.
Advisors: Dr. Albert Folch and Dr. Maarten Saaltink.

Universitat Politècnica de Catalunya
Groundwater Hydrology Group (UPC - CSIC/IDAEA)
Department of Civil and Environmental Engineering
Carrer Jordi Girona 1-3, D-2, 005
08034 Barcelona (Spain)

Cover design by Arauna Studio (Dani Rubio)

Acknowledgements

The PhD thesis has been a life changing experience for me. It has been not only a professional challenge, but also a personal journey, through which I would not have been able to go without the help of many people.

I would like to start by thanking my supervisors, Albert Folch and Maarten Saaltink. I would like to thank Albert for trusting me in first place to do this research, giving me unconditional support and advise through the whole process. I would like to thank Maarten for sharing with me his endless knowledge with patience and understanding. And, in general, I would like to thank them both for their availability and commitment.

I would specially like to acknowledge the role of Jesus Carrera through the whole thesis. He is definitely the one person that most influenced the research, providing invaluable ideas and knowledge. His commitment to the hydrogeology research and his broad view of the field is admirable. I feel fortunate to have been able to work with him side by side.

In general, I would like to thank the whole MEDISTRAES team. This project has been a great challenge in which many people from different organizations, disciplines and countries have join forces. I would like to thank everyone, not only because of their direct help, but much more for their understanding and commitment specially through the difficult moments. Thank you: Laura Martinez, Tybaud Goyeche, Andrea Palacios, Marc Feliu, Hugo Le Lay, Maria Pool, Lurdes Martinez Landa, Valenti Rodellas, Linda Luquot, Juanjo Ledo, Jordi Garcia Orellana, Olivier Bour and Philippe Pezard. In this group I would also like to include Luis (whose surname unfortunately I do not know), who lives close to the field site and help by keeping us save and providing us with help whenever was necessary. Certainly, he is also part of the research team.

I would like to thank Olivier Bour and John Selker for teaching me how to work with the Fiber Optics technology. I spend three wonderful months in Rennes with them, trying to absorb as much knowledge as possible. They are impressive personally and professionally. Continuing with the geographic connection, I would like to thank all the Géosciences Rennes research group, specially Joris Heyman. He adopt me and introduced me to the most lovely and crazy group of researchers. Maria, Yanis, Rosa and Wendy, thank you for the endless fun.

Back to Barcelona, I would like to specially thank to Sebastià Olivella and Alfonso Rodríguez-Dono for helping me with the numerical modelling and for being always ready to help.

I would like to thank the people from the Groundwater Hydrology Group (UPC - CSIC / IDAEA). They are an impressive bunch of researchers and friends. I would like to specially thank former and current members of the group that have help me in one way or another: Michela, Núria, Carme, Paula, Marc, Arnau, Guillem, Oriol, Yufei, Bieito, las Sonias, Albert Carles, Jingjing, Quim , Jordi, Cristina, Rotman, Tere, Daniel and Xavi.

During these years some people have had an important mentoring role in my professionally career, which have driven me where I am now. For their advise and inspiration I would like to thank Andrea Merla, Geert-Jan Nijsten, Jasper Griffioen, Boris van Breukelen and Josep Mas-Pla.

In Barcelona I was lucky enough to meet a wonderful and interesting set of people, with whom I have spend the most hilarious and meaningful moments in the past years. Thank you for being so close: Rubia, Leon, Nuria, Angels, Raul, Pollo, Laurita, Lara, Ana, Jaume, Albert, Romina, Carles, Mireia and Lola. Thank you also to my friends in Cantabria and abroad, who were always there although in the distance: Tamara, Zaira, Debo, Victor, Borja, Sara, Veronica, Meidan, Juste, Vitas, Bea and Kirtin. I pretend to pay a visit to all of them once I am done defending this work.

Finally, the most important ones. Thanks to Nabil for improving my life in all senses. I could have mention you in all paragraphs of this acknowledgements. Thank you for helping me to grow. Thank you to my parents Jose y Ana, to my grandma Isabel, and to my Catalan family, Juan Carlos, Montse, Adria, Nadia and Irene, and in general to all my family. They are all examples of effort and perseverance, and have always been supportive through all my life.

"*We cannot win this battle to save species and environments without forging an emotional bond between ourselves and nature, as we will not fight to save what we do not love.*"

Stephen Jay Gould

To my family

Abstract

Detailed characterization of coastal aquifers is essential for proper management of coastal groundwater resources, and coastal areas in general. Still, there is a general lack of systematic monitoring and detailed characterization of the seawater intrusion (SWI). Part of this lack is related to the limitations of traditional tools and methodologies. In this thesis we aim to provide new approaches and methodologies for the characterization of coastal aquifers, and in particular for the SWI dynamics.

At a first stage, three relatively new monitoring systems were tested to characterise the SWI: Cross-Hole Electric Resistivity Tomography (CHERT), Time Laps Induction Logging (TLIL) and Fiber Optics Distributed Temperature Sensing (FO-DTS). We did that by installing the fiber optic cable and CHERT electrodes outside the borehole casing, and allowing to deploy additional tools through the borehole. This multipurpose approach allowed to deploy multiple tools in parallel, decreasing installation costs and improving characterization by combining complementary information. In fact, the combination of the three methods allowed to discern the SWI multiple dynamics and locations.

From these techniques we were interested in further exploring the use of FO-DTS. However, before that we had to study the use of temperature as a tracer of the SWI. Although the fundamentals of heat transport in groundwater are well known, the use of temperature as a natural tracer for SWI is limited. Numerical modelling was used to explore the potential of temperature for studying SWI dynamics at field scale. The results were used to propose a framework for the interpretation of thermal data at the SWI. The framework gives some guidelines to identify preferential paths of the SWI, flow direction and even roughly estimate groundwater flux rates, in multilayered coastal aquifers. We concluded that temperature has a potential for SWI monitoring largely unexplored.

Based on the promising results from the modelling exercise, we tested the FO-DTS for continuously monitoring of the SWI during one year and a half. This is commonly called a passive application of the FO-DTS. We were able to identify different levels of the SWI, flow directions and short and long term

dynamics. The interpretation confirmed the framework proposed previously.

FO-DTS can also be used actively, thus by heating the fiber optic cable and measuring the evolution of the heating and cooling of the cable. An active FO-DTS application was designed to measure groundwater fluxes and thermal properties of the media. The obtained flux rates are in agreement with independent estimates. Further research is needed to adapt the analytical approach used for the interpretation of the heating curves to account for the effect of the heat storage in the cable materials and surrounding elements. Still, the method shows great potential for its application in quantifying discharge fluxes towards the sea, and in general, to quantify groundwater fluxes in porous media.

Additionally, traditional methods for the interpretation of pumping testing data were revised. A new approach to extract drawdowns from measured heads during pumping in coastal aquifers is proposed. This approach ease and reinforce the use of this traditional hydraulic characterization technique in coastal aquifers.

Many questions remain unanswered, and many others arise from the exploration of these new and traditional techniques. The wide range of information that can be obtained with FO-DTS well deserves more research, in order to facilitate its general use. The revision of traditional methods, such as the classic pumping test, or well-known theories, like the use of temperature as a natural tracer, may be necessary for their application in coastal aquifers. Still, the set of methods proposed in this document expands the tools and the resolution available to characterise the SWI, contributing to expand the available knowledge about coastal aquifers.

Resumen

La caracterización detallada de los acuíferos costeros es esencial para una adecuada gestión de los recursos hídricos, y en general de las zonas costeras. A pesar de su importancia, existe una falta generalizada de monitoreo sistemático y de caracterización detallada de la zona de intrusión salina (SWI). Parte de esta carencia se debe a las limitaciones propias de las herramientas y metodologías tradicionalmente empleadas. El objetivo de esta tesis es proporcionar nuevos enfoques y herramientas para la caracterización de los acuíferos costeros, y en particular de la SWI.

Inicialmente, tres sistemas de monitoreo relativamente nuevos fueron testados en campo para caracterizar la SWI: Cross-Hole Electric Resistivity Tomography (CHERT), Time Laps Induction Logging (TLIL) and Fiber Optics Distribute Temperature Sensing (FO-DTS). Para poder operar las tres herramientas en paralelo, optamos por instalar el cable de fibra óptica y los electrodos de la CHERT entre el entubado del pozo y los materiales del acuífero. De este modo reducimos costes y mejoramos el proceso de caracterización mediante la combinación de fuentes de información complementarias. De hecho, la combinación de las tres permitió detectar diferentes niveles y dinámicas de la SWI en el acuífero.

De estas tres técnicas, nos concentramos en explorar el uso de la FO-DTS. Pero antes, tuvimos que estudiar en mayor profundidad el uso de la temperatura como trazador de la SWI. A pesar de que los fundamentos del transporte de calor en agua subterránea están de sobra establecidos, el uso de la temperatura como trazador natural de la SWI es limitado. El potencial de la temperatura para estudiar la SWI se ha estudiado por medio de modelos numéricos. Los resultados sea han usado para proponer un marco teórico con el que interpretar los datos de temperatura de la SWI. De este modo, usando la distribución vertical de temperaturas podríamos diferenciar niveles de SWI o la dirección de flujo dominante en cada capa del acuífero, e incluso aproximar la velocidad de flujo. Con estos resultados llegamos a la conclusión de que el uso de la temperatura para el seguimiento de la SWI tiene todavía un gran potencial sin explorar.

Basándonos en los prometedores resultados que obtuvimos gracias a los

modelos numéricos, procedimos a testar la FO-DTS para el monitoreo de la SWI en nuestro emplazamiento experimental durante un año y medio. Con los datos obtenidos fuimos capaces de identificar la respuesta térmica de la SWI a eventos a distintas escala temporales. De este modo, los datos confirmaron las conclusiones obtenidas con los modelos numéricos.

La FO-DTS puede ser usada también de forma activa, es decir, calentando el cable de fibra óptica y midiendo la evolución del calentamiento y posterior enfriamiento. En la tesis proponemos una metodología activa de la FO-DTS para medir la velocidad del flujo de agua subterránea y estimar las propiedades térmicas del medio. Los valores obtenidos concuerdan con estimaciones independientes. Sin embargo, debería investigar cómo mejorar el tratamiento del almacenamiento de calor en los materiales del cable en la solución analítica usada para la interpretación de los datos. En cualquier caso, el método tiene gran potencial para ser aplicado tanto para la caracterización del flujo de descarga al mar en acuíferos costeros, como en cualquier medio poroso saturado.

Asimismo, se ha revisado la interpretación de los tradicionales ensayos de bombeo. De esta revisión surge proponer una alternativa para separar los descensos de los niveles medidos durante el bombeo. Esta metodología debería facilitar y reforzar el uso de ensayos de bombeo para la caracterización hidráulica de acuíferos costeros.

Muchas preguntas permanecen sin ser contestadas y otras muchas surgen de la exploración de tecnologías de monitoreo nuevas y tradicionales. La FO-DTS proporciona diferentes tipos de información sobre la SWI, lo que bien justifica profundizar en su desarrollo para poder generalizar su uso. Por otro lado, la revisión de métodos tradicionales, como los ensayos de bombeo, o de metodologías establecidas, como el uso de la temperatura como trazador, podrían beneficiarse de cierta revisión para adaptarlas a las condiciones especificas de los acuíferos costeros. En cualquier caso, el conjunto de métodos presentados en este documento expande el número de herramientas y resolución disponibles para la caracterización de la SWI en acuíferos costeros.

Contents

List of Figures

List of Tables

List of Abbreviations

SWI	**S**ea**W**ater **I**ntrusion
SGD	**S**ubmarine **G**roundwater **D**ischarge
FO-DTS	**F**iber **O**ptics **D**istributed **T**emperature **S**ensing
CHERT	**C**ross **H**ole **E**lectric **R**esistivity **T**omography
ERT	**E**lectric **R**esistivity **T**omography
TLIL	**T**ime **L**apse **I**nduction **L**ogging

Chapter 1

Introduction

1.1 Background

1.1.1 Coastal aquifers

Coastal aquifers are aquifers where continental fresh groundwater and seawater meet (Post, 2005). Therefore, the main difference between coastal aquifers and any other type of aquifers is the hydraulic connection with the sea (Post and Abarca, 2010). This connection gives coastal aquifers a set of peculiarities: 1) flow patterns depend on the density variations, 2) they are usually located on geologically active environments, such as deltaic areas, 3) they are exposed to a wide range of periodic head fluctuations, 4) they show chemical zoning due to the mixing between saline and fresh groundwater, and 5) they present two defining features: an interface between both fresh and salt groundwater and a zone where submarine groundwater discharges (Jiao and Post, 2019; Post, 2005; Post and Abarca, 2010; Werner et al., 2013). These peculiarities render coastal aquifers a complexity that is far from being completely understood.

Coastal aquifers belong to the so-called coastal zones, which are defined as the areas where the complex interface between land and sea takes place (Michael et al., 2017). Although there are many other definitions (Jiao and Post, 2019; Council of the European Union, 2009), still all of them highlight the complex interactions. Because of these interactions, coastal aquifers have an enormous importance in sustaining coastal and marine ecosystems, such as coastal lagoons, marshes and shallow marine environments (Taniguchi et al., 2019). All groundwater dependent ecosystems are characterised by a delicate equilibrium between fresh and saline conditions, which largely depend on the groundwater contribution.

Coastal aquifers are also important for the human well-being. Almost half of the world's population lives within 100 km from the coast (Martínez et al., 2007; Jiao and Post, 2019). Such a large population density usually translates

into high economic activity, which results in a large demand for fresh water, which in many cases is supplied by groundwater. This necessity is exacerbated in arid regions, where coastal fresh groundwater resources cover most of the demand (UNEP/MAP, 2015). It is even more essential for small islands, where all groundwater reservoirs are small and - in most cases- are the only source of fresh water (IOC-UNESCO and UNEP, 2016). Coastal aquifers, as part of the coastal zone interlinked system, are an important asset for the global economy. In fact, coastal zones are estimated to contribute US28 trillion annually to the global economy (IOC-UNESCO and UNEP, 2016).

Despite our dependency on coastal groundwater resources and their importance for the environment and the global economy, coastal aquifers are subjected to a large number and variety of threats, of which saline groundwater seeping into the aquifer is the most important (Post, 2005). It may occur for several reasons. Over-exploitation of fresh groundwater resources is one of them (Konikow and Kendy, 2005). This is intimately related to the increase in population in coastal areas (Neumann et al., 2015; Jiao and Post, 2019). Increasing population leads to high risk of pollution from agricultural or industrial activities, waster water and solid waste disposal. Threats at larger scale include the effects of climate change, such as increase in the mean sea level or the decrease in freshwater recharge in some areas (Green et al., 2011; Oude Essink, Van Baaren, and De Louw, 2010).

Important managerial difficulties stem from this complex interaction between human and natural systems. Proper management requires sufficient knowledge and understanding of the coastal groundwater processes (Michael et al., 2017). Despite the large amount of research in the field of coastal hydrogeology (Jiao and Post, 2019), there is still plenty of room for improvement. The lack of systematic data collection or the lack of understanding of transient process at the fresh and saltwater interface are some of the identified knowledge gaps (Post and Abarca, 2010; Michael et al., 2017; Werner, 2017).

Generally speaking, research on coastal aquifers focused in the two abovementioned characteristic features of coastal aquifers: the interface between fresh and salt groundwater, and the discharge of groundwater to the sea. In hydrogeology coastal aquifers have been traditionally researched from the onshore point of view, thus focusing on the fresh-saltwater interface as an indicator of the quantitative and qualitative status of fresh groundwater body, while oceanographers have focused on quantifying the submarine groundwater discharge (SGD) fluxes. Increasing interest in the SGD has increased over the past two decades (Taniguchi et al., 2019). Probably, due to the implications of the discharging groundwater in marine environments. Both, fresh-saltwater interface and the SGD are features intimately related. For this reason, the

tendency in is to adopt more holistic and interdisciplinary approaches to the coastal aquifers research.

1.1.2 Onshore implications: Seawater intrusion

Under natural steady conditions fresh groundwater flows towards the sea driven by the difference in head between recharge areas and the mean sea level. At the point where fresh and saline groundwater meet, density contrast between both, forces fresh water to flow on top of the saline groundwater body, while a re-circulation cell is generated in the saline groundwater body. At this location both groundwater bodies partially mixed while flowing towards discharge, developing an interface between both. This interface is called transition zone, mixing zone, fresh-salt water interface, saltwater wedge, or seawater intrusion, depending on what processes are emphasized. In this document we will use the term seawater intrusion (SWI). The SWI term, has a negative connotation, implying that the interface between fresh and salt groundwater is moving inland, polluting the precious fresh groundwater resource. However, in this case we will refer also to the retreat of the SWI, when the interface moves towards the sea, due an increase of the fresh groundwater component.

The SWI has a highly dynamic nature. Its position extension and width responds to multiple external forces acting at a wide range of spatial and temporal scales. The positions of the SWI is usually defined by the position of the toe, that is the x and y coordinates where the 50% mixing isoline meets the aquifer bottom. This position depends on the discharge flux towards the sea, the aquifer hydraulic properties, the elevation of the sea and the aquifer morphology. In unconsolidated aquifers it is usually formed by an alternation of permeable and impermeable layers, each of them contacting the sea at different distances from the shore. Thus, several SWIs with their respective toes may be distinguished. Additionally, the width of the interface will depend mainly on the inland freshwater head and seawater level fluctuations (Werner et al., 2013), such as tides (Pool, Post, and Simmons, 2014) and the heterogeneity of the aquifer materials (Fahs et al., 2018).

Understanding the factors that control the SWI is the topic of an extensive number of publications. The urge to identify and understand these factors emanates from the necessity to minimize or correct the salinization of coastal aquifers, which is the most important problem threatening coastal aquifers. For example, in Spain 86% of the coastal groundwater bodies present salinization problems (Custodio, 2017). Despite the magnitude of the problem, there is still a lack of understanding of transient processes and timeframes affecting

the SWI, and the characterization and prediction of the SWI at regional scale and in highly heterogeneous and dynamic settings (Werner et al., 2013).

1.1.3 Offshore implications: Submarine groundwater discharge

Coastal aquifer's influence on marine environments takes place through the submarine groundwater discharge (SGD). SGD is defined by Moore (2010) as the flow of water through continental margins from the seabed to the coastal ocean, with scale lengths of meters to kilometers, regardless of fluid composition or driving force.

Although, discharge fluxes to the sea of rivers are much larger than those of aquifers, nutrients fluxes due to SGD are around 1.6-fold of those due to river discharge (Cho et al., 2018). Additionally, SGD is distributed along the coast affecting large extensions of territory. This influence to the coast may be positive by, for example, providing nutrients to oligotrophic areas (Rodellas et al., 2017). In other cases, an excess of nutrients may result into algal blooms or hypoxic conditions (Moore, 2010). In fact, 16% of the worlds large marine ecosystems are at a high risk of coastal eutrophication (IOC-UNESCO and UNEP, 2016). In Spain, the eutrophication of the Mar Menor in Murcia (Alcolea et al., 2019) is a recent example of this global problem .

Because of its implications for the marine ecosystems and coastal economies, coastal hydrogeologist interest in SGD has increased in the last decade. This dissertation mainly focuses on the characterization of the SWI. However, whenever possible, we will extend finding and conclusions on SWI to the knowledge and understanding of SGD.

1.2 Characterization of coastal aquifers

The characterization of an aquifer requires the collection of enough information to understand the properties of the system, such as the geology, hydraulic properties or mean water fluxes; and its dynamics, such as groundwater levels, temperature or geochemistry. Both require a high amount of resources (Jiao and Post, 2019). Therefore, the number of well-characterized examples of SI is small, and this has impeded understanding of field-scale processes (Werner et al., 2013).

There are many technologies and approaches for coastal aquifer characterization, such as geophysical, hydraulic and geochemical methods. For example, the fresh-salt water interface position can be identified interpretation of geochemical data (Andersen et al., 2005), with borehole logging, by the water

column pressures in boreholes (Kim, Chon, and Park, 2007), electrical tomography (Henderson and Harvey, 2009; Palacios et al., 2020) or even interpreting groundwater temperature-depth profile (Taniguchi, 2000). Each method provides advantages and limitations, and usually a combination of various of these methods is required to have a complete picture of the subsurface. Another example is the hydraulic characterization of the aquifer. In coastal aquifers this is especially difficult due to the influence of the sea on the groundwater heads oscillation. Tides induced oscillations allows the application of specific methods, like the tide response methods which are not completely reliable, but at the same time complicates the interpretation of traditional ones, like pumping test.

Characterization of dynamic processes is usually referred to as monitoring. Traditional monitoring of the SWI is usually based on measuring the groundwater heads and solute concentrations in piezometers. In most cases, down-hole sensors that are used to measure heads (pressure) and concentrations (electrical conductivity), provide high temporal resolution but low spatial coverage. Existing methods do not allow acquisition of data with high spatial resolution, and in most cases neither temporal resolution. This prevents the identification and study of processes affecting the SWI at multiple time scales. Some new techniques are being developed that allow more data to be collected. An example of this set of technologies are the fiber optic based sensors, such as Fiber Optic Distributed Temperature Sensing. In fact, an important part of the approaches we will explore in this manuscript are based on Q Q the use of Fiber Optic Distributed Temperature Sensing (FO-DTS).

1.3 Fiber Optic Distributed Temperature Sensing

FO-DTS is based on the principle that when a light pulse propagates along a fiber, it energizes the glass and molecules, which are then able to give off light at waveleghts different from the incident one (Smolen and Spek, 2003). The re-emitted wavelengths are above (Stokes) and below (Anti-Stokes) the emitted frequency. This process is called the Raman scattering (Selker et al., 2006). The intensity of the Anti-Stokes signal depends on the temperature of the fiber. Therefore, the ratio between the intensities of Stokes (which is not sensitive to the temperature) and Anti-Stokes can be related to the temperature of the cable.

FO-DTS provides simultaneous high spatial and temporal resolution temperature data. As light travels at a constant speed, it is possible to estimate the position from where it came based on the time it takes for the backscatter signal to reach the sensor. The distance cannot be calculated exactly, and thus

the sensors has a maximum sampling resolution, which ranges between 0.25 and 1 m depending from the lecture unit. Spatial resolution is however larger than the sampling resolution. Smolen and Spek (2003) define spatial resolution as the distance it takes for a system to fully response to a sudden change in temperature. As a rule-of-thumb, a minimum of two adjacent measurements should be averaged. Thus, if the DTS has a sampling resolution of 0.5m, the spatial resolution would be of 1m. Additionally, the distance covered by a DTS units can be of kilometers. If we add the fact that the offered sampling frequency is 10s, one can imagine the amount of data that can be collected with just one instrument.

Temperature resolution of a FO-DTS system may range from 0.01°C to 0.5°C, depending on the lecture unit manufacturer and model. Temperature resolution decreases with the cable distance and with sampling frequency. Therefore, currently available FO-DTS systems can achieve either a very long continuum of measurements, a very frequent sampling interval, oR very high accuracy, but all three cannot be achieved at the same time (Tyler et al., 2009; Shanafield et al., 2018). On the other hand, temperature resolution also depends on the amount of backscatter signal, which systematically decreases with distance, but also is reduced by imperfections in the fiber or connections. These are very important factors to bear in mind when choosing this technology for a specific application.

An important consideration in the adoption of this technology is the temperature calibration procedure. The ratio between the Stokes and Anti-Stokes signals is related to the temperature by a set of parameters that need to be calibrated based on a minimum of two known temperatures along the cable. Although this step is already implemented in most sensors, many practitioners perform it externally in order to increase the temperature accuracy. There are two main approaches: (1) single-ended calibration (Hausner et al., 2011), which implies deploying the fiber optic cable in one direction; and (2) double-ended calibration (Giesen et al., 2012), which implies deploying the cable through both ends. Single ended measurements are more precise close to the instrument and degrade with distance, while double-ended measurements are more precise in the middle and less at the ends. These two approaches have multiple variations to be adapted to the circumstances. Even in cases with complex installations or large noise, ad-hoc calibration procedures may be designed. In any case, a complete understanding of these procedures is needed to optimize the fiber installation, and obtain accurate temperature data.

Despite its limitations, since its appearance in the hydrology field (2006) (Tyler et al., 2009), a cascade of applications has appeared. Thus, FO-DTS seems to have fulfilled an urge for more in-situ data, which other technologies

have not been able to provide.

Two main types of applications can be found in the literature, passive and active. Passive FO-DTS applications are limited to measure natural changes in temperature, while active FO-DTS applications take advantage of heating the monitoring cable, or the surrounding materials, to increase resolution or measure processes otherwise hidden. Passive FO-DTS in hydrogeology has been used to characterize fractured aquifers (Klepikova et al., 2014; Klepikova et al., 2011), to study groundwater-surface water relations (Henderson and Harvey, 2009; Sebok et al., 2013; Vogt et al., 2010), to monitor managed aquifer recharge (Becker, Bauer, and Hutchinson, 2013) and to monitor geothermal installations (McDaniel et al., 2018; Jaaskelainen, 2010) among others. Active FO-DTS applications have been used to perform thermal resistance test (Freifeld et al., 2008), as a fluid logging technique (Banks, Shanafield, and Cook, 2014) and for heat tracing (Bakker et al., 2015; Hausner et al., 2016; Tombe et al., 2019). The only applications related to coastal aquifers concentrate on measuring changes in surface temperature in groundwater discharge areas that can be related to the occurrence of SGD.

1.4 Research objectives and outline

As we have seen in previous sub-sections, coastal aquifers and in particular SWI dynamics and characterization, remains a topic of intense research and open questions. Lack of in-situ data and detailed characterization of coastal sites have been identified by several authors as major obstacles to understand the factors controlling the SWI. Moreover, emphasis is placed on the connection between the SWI and the SGD dynamics, adding relevance to the study of the first in order to understand the second. We think that part of the knowledge gaps about the SWI, is related to limitations of available methodologies for coastal aquifers characterization.

In this document we will propose several tools and methodologies for the characterization of the SWI. Particularly, we will study the use of FO-DTS technology, but also combine it with other traditional and recently developed methods. The obtained data and results should help to improve understanding of the transient processes taking place at the SWI, and how these may affect the SGD dynamics.

This overall objective will be achieved in different ways:

- In Chapter 2, a new experimental site densely instrumented was constructed to study SWI as part of the MEDISTRAES project (Mixing and DISpersion in the TRAnsport of Energy and Solutes), in which this

dissertation is also a part of. New techniques were tested and combined for the detailed characterization of the SWI in the site.

- In Chapter 3, a new approach is proposed to remove environmental trends and noise from pumping tests data. The method is tested to interpret a pumping test performed at the research site. This approach may help practitioners in characterising the hydraulics of coastal aquifers.

- In Chapter 4, a new method for the quantification of groundwater fluxes using active FO-DTS is proposed. This approach provides direct measurements of the vertical distribution of groundwater fluxes, as well as estimates of the thermal properties of the aquifer.

- In Chapter 5, temperature is proposed as a natural tracer to monitor the SWI dynamics. We use two simplified numerical models to analyse the coupled behaviour of heat and solute transport at the SWI, and discuss the extent up to which temperature can be considered a good proxy to study the SWI dynamics and its implication the study the SGD.

- In Chapter 6, FO-DTS is used to monitor the SWI at the research site over one year and a half. The collected data is analysed in order to conclude the potential of this technology to study the SWI dynamics in a real site.

Chapter 2

Multimethodological approach to characterize and monitor a coastal aquifer [1]

This chapter describes the construction of a new experimental site and the initial results from testing and comparing different methods for the characterization and monitoring of the saline intrusion. The site is located close to Barcelona city (Catalunya, Spain) in a coastal alluvial aquifer. It is located between 30 and 90 m from the seashore, and comprises 16 shallow piezometers. The piezometers are organized in nests of three with depths ranging between 15 and 25 m and 4 solitary piezometers. The objective of this research is to combine different recently developed monitoring techniques to evaluate temporal variations in the aquifer of the site at different spatial scales before and after the dry season of 2015. At the site scale, fibre optic distributed temperature sensing (for the first time applied in coastal aquifers) and cross hole electrical resistivity tomography (first time at this scale) has been applied. At the meter/borehole scale, electrical conductivity of the formation has been applied not only in a repeated manner ("time lapse"), but also for the first time at relatively high frequency (tens of minutes). CHERT has provided a better characterization of the seawater intrusion than data obtained from

[1] This chapter is an edited version of: Albert Folch, Laura del Val, Linda Luquot, Laura Martínez-Pérez, Fabian Bellmunt, Hugo Le Lay, Valentí Rodellas, Núria Ferrer, Andrea Palacios, Sheila Fernández, Miguel A Marazuela, Marc Diego-Feliu, María Pool, Tybaud Goyetche, Juanjo Ledo, Phillipe Pezard, Olivier Bour, Pilar Queralt, Alex Marcuello, Jordi Garcia-Orellana, Maarten W Saaltink, Enric Vázquez-Suñe, Jesús Carrera. "Combining Fiber Optic DTS, Cros-Hole ERT and time-lapse induction logging to characterize and monitor a coastal aquifer." Journal of Hydrology (2020). (In press). The implementation of the CHERT and TLIL measurements and their initial interpretation was not carried out by the author of this dissertation.

piezometers. However, the combination of techniques has allowed improving the understanding of the system by: 1) differentiating two aquifer levels with different dynamics, separated by a silt layer, only few decimetres thick, and 2) identifying preferential flow paths over different time and spatial intervals. Future challenges and the application of these techniques in other areas are also discussed.

2.1 Introduction

About 41% of the world population lives in coastal areas (Martínez et al., 2007), where groundwater is the main source of freshwater. Intensive groundwater exploitation has caused seawater intrusion (SWI) in the past decades, bore and soil salinization with important losses in agricultural production globally. Moreover, the impact and magnitude of SWI is expected to be exacerbated by the increase in the freshwater demand due to the population growth, as well as by climate change and sea-level rise. Much progress has been made to characterize SWI in coastal aquifers and understand the reactions occurring in the subterranean estuary (Anwar, Robinson, and Barry, 2014; Moore, 2010; Moore, 1999; O'Connor et al., 2015; Santos et al., 2009; Spiteri et al., 2008). However, the understanding of the dynamics of mixing and dispersion and its impact on chemical reactions remains a challenge.

Transport processes in coastal aquifers have recently received increasing attention, particularly in relation to the threat of SWI as well as the complex aquifer-ocean interactions. Density-driven circulation significantly affects dispersion, mixing, and reaction behavior of nutrients and contaminants transported by freshwater, and thus, the supply of these compounds to the coastal sea (Brovelli, Mao, and Barry, 2007; Dror et al., 2003). The discharge of groundwater to the sea, commonly referred to as submarine groundwater discharge (SGD), has been recognized as a relevant source of dissolved nutrients (Kim, Kim, and Hwang, 2011; Rodellas et al., 2015) and metals to the ocean (e.g. (Bone et al., 2007; Trezzi et al., 2017; Windom et al., 2006) with important implications for coastal areas. Therefore, quantification of fluxes between coastal aquifers and oceans is critically important, both from a hydrogeological and oceanographic perspective. However, while studying the same process and addressing the same key questions, these two communities have evolved independently.

Fluctuations on the fresh-saltwater interface location and width depend on many factors (e.g. recent and past freshwater inputs, permeability of the aquifer, sea-level, and tidal range). The complexity of coastal systems under natural dynamics is aggravated by global change (e.g. sea-level rise, changes in precipitation, increased urbanization in coastal areas, increase on the demand of hydrological resources, etc.) (Michael et al., 2017; Rufí-Salís et al., 2019). The predicted climate change with its associated sea-level rise will modify flow regimes and groundwater discharge conditions in many coastal areas. All these changes and interactions will affect the inland extension and behaviour of SWI as well as the chemical composition and magnitude of SGD. Additionally, despite the transient behaviour of SWI, its current understanding is mainly

based on studies that assume steady-state conditions (Werner et al., 2013), and thus implicitly neglect the transient effects and processes that are occurring at different temporal and spatial scales, such as quality patterns (mixing, cation exchange and/or precipitation/dissolution of different minerals). Furthermore, the behaviour of SWI differs between passive and active SWI (Badaruddin, Werner, and Morgan, 2015; Werner, 2017), and rain events can also have an important influence in the dynamics of these systems at day time-scale (Cerdà-Domènech et al., 2017; Giambastiani et al., 2017).

The dynamics of the SWI are also affected by factors offshore, such as the morphology of the beach, the tidal regime, wave action and the flux of fresh groundwater that discharges offshore (Michael, Mulligan, and Harvey, 2005). Even a low permeable layer, as thin as a few decimeters, may form a confining layer dividing the system in two aquifers and modifying the dynamics of the system (Pauw et al., 2017). This kind of lithological structure with a low permeable layer changes the behaviour of the SWI and modifies the way in which groundwater discharges into the sea. Furthermore, layered aquifer systems may exhibit enhanced seasonal exchange due to an increase in the length of the fresh-saltwater interface (Michael, Mulligan, and Harvey, 2005). Therefore, due to the importance of lithological variability on groundwater flow and salinity patterns, detailed field studies are needed to understand these interactions (Pauw et al., 2017).

Traditional methods to characterize aquifers inland are also used to depict groundwater systems in coastal areas. Direct information is obtained from piezometers where hydraulic head, salinity, hydrochemistry and isotopes are measured/sampled to study the SWI and coastal groundwater systems (Re et al., 2014). However, as was stated already by Post (2005) already in 2005, in order to successfully apply existing and future models that describe three-dimensional flow, transport and geochemical interaction under variable density conditions, a detailed and accurate characterization of the subsurface is required. In recent years, there have been many new techniques focused on this characterization, which are summarized below.

Due to the correlation between water salinity and bulk or formation electrical conductivity, electrical methods such as electromagnetic methods and electrical resistivity tomography (ERT) represent are interesting tools to monitor SWI. Induction logging can also be used to effectively detect and monitor the saltwater wedge at the meter scale and in the near field around boreholes (Denchik et al., 2014; Garing et al., 2013; Pezard et al., 2015). ERT is widely used for hydrological purposes, such as monitoring contaminant plume migration or estimation of aquifer parameters (Camporese et al., 2011; Cassiani et al., 2006; Koestel et al., 2008; Muller et al., 2010; Nguyen et al., 2009; Perri

et al., 2012; Singha et al., 2015). Some examples of its successful application to image the freshwater-saltwater interface in different coastal areas are described by (Franco et al., 2009; Goebel, Pidlisecky, and Knight, 2017; Morrow, Ingham, and McConchie, 2010; Nguyen et al., 2009; Zarroca et al., 2014). Nevertheless, although widely used, the sensitivity of the ERT measurements depends on the acquisition methodology. One of the most widespread method consists on positioning the electrodes on the surface. The resolution under this configuration decreases as the acquisition depth increase, preventing the quantitative use of the data from a hydrogeological perspective. An alternative method consists of installing the electrodes along the piezometers, which contributes having better resolution acquisitions (Perri et al., 2012). Attempts to link bulk electrical conductivity obtained using surface or surface-to-borehole ERT are found in the literature (Beaujean et al., 2014; Huizer et al., 2017; Nguyen et al., 2009).These studies concluded that ERT-derived water salinity is usually underestimated. Therefore, attaching electrodes around and along the piezometers, allows to acquire data near the area of interest and cross-hole, limiting the loss of resolution in depth.

Temperature can also be used as a tracer of environmental processes in groundwater using the temperature contrast between two end-members. Fibre Optics Distributed Temperature Sensing (FO-DTS) has already proved to be a useful cost-effective tool to perform detailed monitoring of environmental processes (Selker et al., 2006; Tyler et al., 2009). At present, FO-DTS instruments provide a maximum temperature resolution of 0.01^{o}C, a spatial sampling of 0.25 m along the cable and a temporal resolution of fractions of a minute dependning on the configuration choosen (Selker et al., 2006; Simon et al., 2020). The application of this technology in groundwater environments, has been used in both fractured media and unconsolidated aquifers to determine river-aquifer interactions (Briggs et al., 2016; Rosenberry et al., 2016), evaluate groundwater preferential paths, identify fractures connectivity, and approximate aquifer hydraulic and thermal properties (Bakker et al., 2015; Bense et al., 2016; Hausner et al., 2016; Klepikova et al., 2014). In coastal aquifers, temperature may be a good indicator for mixing due to the different temperatures of fresh groundwater and seawater. Based on this contrast, Taniguchi (2000) used temperature as a proxy to monitor dynamics in the fresh-saltwater interface at a coastal aquifer in Japan. The same principle was used by Debnath et al. (2015) and Henderson et al. (2008) to monitor interactions between groundwater and sea water using temperature probes and FO-DTS respectively. Based on these natural differences in temperature, FO-DTS may be used as a passive sensor to monitor the spatial distribution and temporal fluctuations of the fresh-salt

water interface with high definition. Despite some examples that combine marine ERT and FO-DTS to monitor tidal pumping and SGD (Henderson et al., 2010), FO-DTS has not been applied yet to characterize SWI.

Given the importance of the fresh groundwater preservation and the complexity of coastal aquifer settings, it is doubtful that a single technique is enough to understand the whole system. For this reason, we have developed a research site in a Mediterranean alluvial aquifer (North of Barcelona, Catalunya, Spain), between 40 and 90 m from the seashore, to compare the performance of different characterization methods and provide new insights to be shared among the SWI and SGD scientific communities. Unlike most studies conducted elsewhere, the selected are presents a microtidal regiome, which allows focusing on other physical driving forces (waves, storms, groundwater table elevation, etc).

In this paper we present the preliminary results of the jointly application of different novel monitoring techniques with the objective to evaluate temporal variations of a coastal aquifer at different spatial scales. At the site scale, the selected techniques are: 1) Cross hole electrical resistivity tomography (CHERT) and 2) FO-DTS, as a first attempt to apply this technique to characterize SWI. At meter/borehole scale, for the first time according to the authors knowledge, we deployed a time lapse induction logging (TILL) with an electromagnetic probe to obtain formation conductivity logs at relatively high frequency (one sample every ten minutes) to study aquifer processes at these time scales. These techniques are compared with traditional measures in piezometers (electrical conductivity and temperature) and applied to obtain two snapshots at different times to characterize the beginning and the end of the dry season (June and September 2015).

2.2 Experimental site

The experimental area is located at the Mediterranean coast close to the mouth of the ephemeral stream Riera d'Argentona, 40 km to the NE of Barcelona (Catalunya, Spain), between the urban areas of Mataró and Vilassar de Mar (Figure 2.1). The area is subjected to a Mediterranean semi-arid climate with an average annual precipitation of 610 mm (period 2010-2013). The land use is manly divided into agriculture and urban and natural forest (Rufí-Salís et al., 2019). The watercourse is characterized by torrential and non-permanent water flow, which only develops in case of heavy rain events.

The site is located in the lower part of the Argentona stream alluvial aquifer. The geology of the experimental site is dominated by layers of quaternary gravels, sands and clays which are the product of the weathering of the

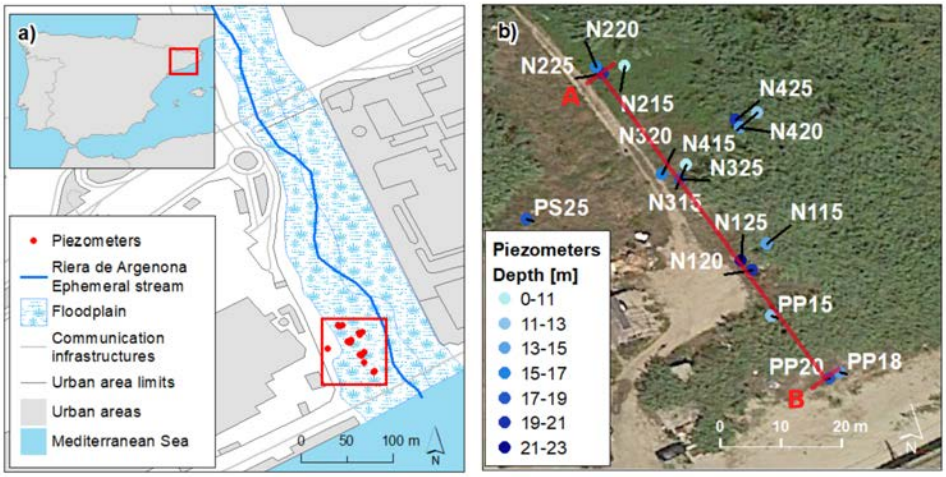

Figure 2.1: Location and pilot site setup in the NW Mediterranean basin. a) Maps depicting the location of the field site with respect to the surrounding water bodies and infrastructures. b) Map showing the distribution of the installed piezometers at the experimental site. The color scale indicates the depth of the screened section of each borehole. The red line depicts the position of the vertical cross-sections shown throughout the article, from A (inland) to B (seawards).

surrounding granitic outcrops (Figure 2) (Martínez-Pérez et al. 2018, Internal communication).

In a distance of 30 to 90 m from the seashore, 16 shallow piezometers were installed in a small area of 30 by 20 meters, 30 m inland from the seashore. Most piezometers are gathered in nests (N1, N2, N3 and N4) of three (15, 20, 25), with depths of around 15, 20 and 25 m (e.g. nest N1 is composed of piezometers N115, N120 an N125). Four stand-alone piezometers were also installed (PS25, PP15, PP18, and PP20, with depths of 25, 15, 18, and 20 m, respectively). All piezometers were equipped with at least 2 m of blind pipe at the bottom, followed by 2 m of screened tube just above. The only exceptions were piezometers PP15 and PP20, which were screened 11 and 15 m respectively. The study presented here focuses on a cross-section perpendicular to the sea following the piezometers N225, N325, N125, PP15 and PP20 (Figure 2.2).

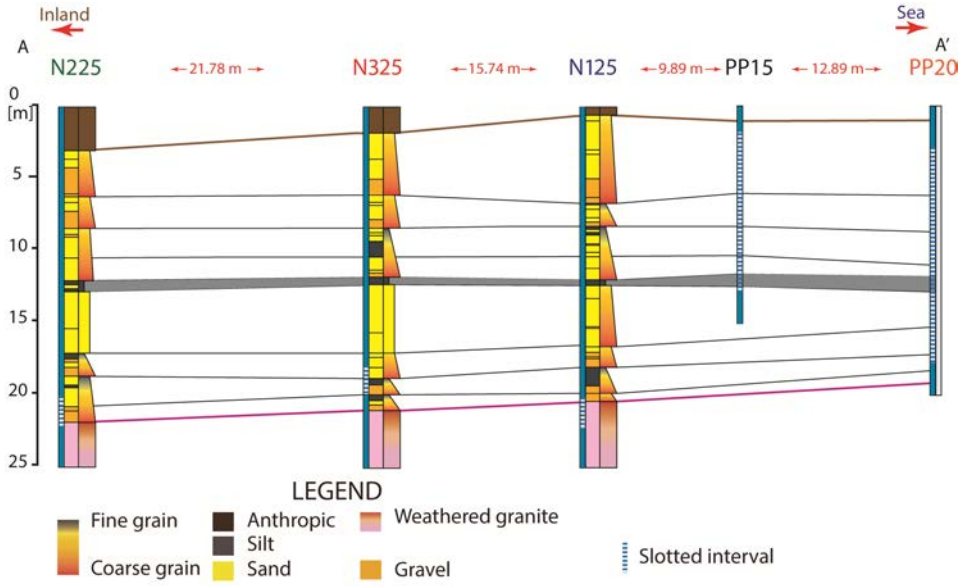

Figure 2.2: Cross section of the experimental site perpendicular to the seashore (Figure 1b). The different color lines represent the contact between weathered granite and the alluvial formation (red) and between the anthropic materials and the alluvial sediments (Brown). Black lines represent the correlation between fine materials levels in the different piezometers integrating gamma log data for all boreholes (data not shown). Grey layer indicates a continuous layer of silt that crosses all piezometers

2.3 Methodology

The methodology described below describes the two stages of the study: (1) initial downhole set-up of both FO-DTS and the distribution of electrodes to perform CHERT, and (2) field surveys of FO-DTS, CHERT and time-lapse induction logging.

2.3.1 1.1. Installation of annulus fiber optic cable and electrodes during site construction

The fiber optic cable (Brugg Kabel AG, Switzerland) and CHERT electrodes lines were placed during piezometers installation in the annular space between the PVC casing and the formation. The procedure consisted of three steps: (1) electrodes assembly; (2) installing the electrodes along the tubing; and (3) fiber optic cable set-up along the piezometer casing (Figure 3). The assembly of the

electrodes aimed at hindering corrosion, since this is one of the main difficulty with semi-permanent electrodes in a saltwater environment. The electrodes, made of stainless steel meshes, were tested in the laboratory by submerging them (and the cables) in a salty solution (55 mS/cm). Then, the electrodes were connected to an electrical cable through which an electrical current was imposed to observe the corrosion. The most sensitive part of the system was the connection between the mesh and the cable. After several tests, we determined that the best strategy to delay corrosion was to fully cover the connection with silicone to minimize the contact with saltwater. The final prototype showed corrosion signs in the laboratory after 20 days of continuous current of 1 A at 3 Hz frequency. The current injected during field experiment is much smaller than 1A and time of injection is only a few mS. This, together with the reducing conditions fonded at the deepest part of the site (Martínez-Pérez et al. 2018, Internal communication), should ensure reliable operation for the foreseeable duration of the project. More details in the CHERT configuration can be found in Palacios et al. 2020.

The installation stage consisted of fixing electrodes and fiber optic lines to the casing by means of nylon flanges, which effectively acted as centralizers to protect the two lines (Figure 2.3). Had the wells been deeper, more sturdy protection and centering system would have been needed. The first casing sections were instrumented outside the well and placed vertically inside the auxiliary drilling tubing with the help of the rig crane. The rest of the casing sections were instrumented just after they had been screwed to the casing string already in place. The casing, thus instrumented, was lowered smoothly into the auxiliary tubing for all piezometers. Special attention was paid to prevent dragging casing and instrumentation lines during the extraction of the auxiliary tubing. To this end, we tried to minimize the length over which filter sand in the screened interval, or clay pellets elsewhere, overlapped with auxiliary tubing (Figure 3). The whole operation requires the pro-active collaboration of drillers, who were carefully trained on what we were trying to do.

The deepest piezometers of each nest, and the stand-alone piezometers (PP15 and PP20) were equipped with 36 electrodes (Figure 2.2) to perform both vertical and cross-hole electrical resistivity tomography (CHERT). Distances between electrodes were 40 cm, 50 cm and 68 cm for piezometers with depths of 15 m, 20 m and 25 m, respectively. In the Argentona site, the distance between nests and pumping wells varies from around 10 m to 26 m while the distance between PP20 and P15, the shallowest piezometers equipped with CHERT, is of 12.7 m. In the line perpendicular to the coastline, the CHERT has an aspect ratio (horizontal distance between boreholes divided by depth of boreholes) between 0.6 and 0.8.

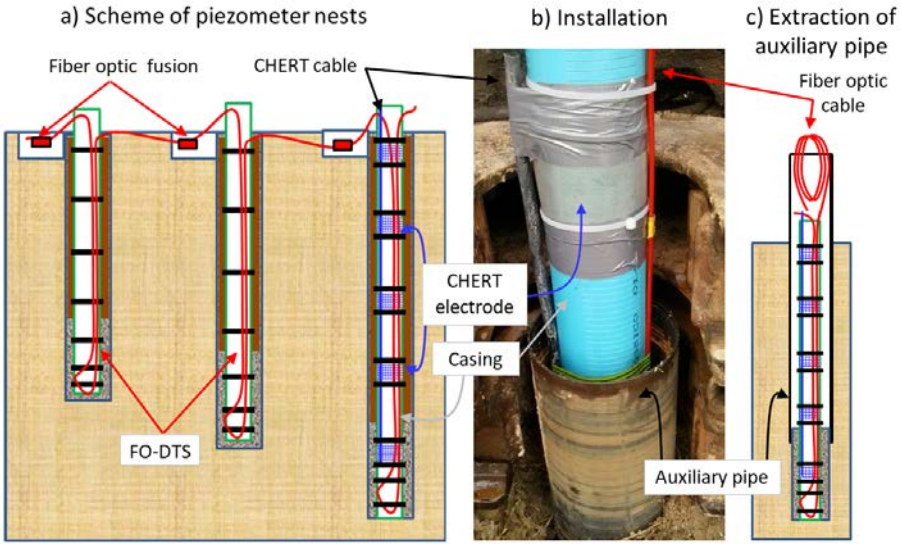

Figure 2.3: a) Schematic description of piezometer nest monitoring system, including CHERT electrodes (actually, 32 electrodes were installed in each piezometer) and fiber optic cable for DTS. (b) photo of the electrodes and cable installation in the piezometric tube. During extraction of the drilling auxiliary pipe (c), the fiber cable has to be cut, requiring fusion points. The black bar represents the nylon flanges to fix the electrodes and the fiber optic cable on the piezometer.

In order to perform FO-DTS, fiber optic cables must be installed in all the piezometers of the site. This made it difficult because the cable needed to be cut to extract the auxiliary tubing (Figure 3). The end of the cable was passed through the tubing to minimize the number of cable segments (or fusions) connections, which cause a loss in signal. In hindsight, this has proven a severe hindrance.

The connections between fusions were done with a Prolite-40 Fusion Splicer (PROMAX, Spain) and an EFC-22 fiber optic cutter (Ericson, Sweden). Two continuous lines of fiber optic cable were set up along the site period. Line 1 included wells from nest N1 and N3, and stand-alone wells PP15 and PP20 period. Line 2 included wells PS25, N220, N215, N225. The total length of fiber optic cable installed was of 1,900 m approximately, with 17 connections.

2.3.2 Data aquisition

All surveys were performed in 2015. CHERT data were acquired on July 3^{rd} and September 8^{th} in boreholes N125, N225, N325, PP20 and PP15. Temperature with FO-DTS was measured on June 25^{th} – 26^{th} and September 10^{th}, in all piezometers, for durations spanning between one and four hours. Time-lapse induction logging (TLIL) were recorded only in borehole N3-20 on May 11^{th} and 12^{th}. During all field surveys, head levels, groundwater temperature and electrical conductivity were measured in all piezometers including water EC vertical profiles in PP20 using a CTD-Diver Schlumberger.

Cross hole electrical resistivity (CHERT)

CHERT was done in four pairs of piezometers to obtain a cross-section perpendicular to the coastline, from PP20 to N225. The acquisitions were made using 72 electrodes in total. To maximize resolution, the cross-hole configurations used were dipole-dipole, pole-tripole, and Wenner, following Bellmunt et al. (2016) (Figure 2.4). We used a ten-channel *Syscal Pro* resistivity meter and an optimized survey design which allowed to record normal and reciprocal measurements: a total of 5842 data points per cross-hole panel in 30 minutes. The recording of a complete CHERT took 2 hours.

CHERT apparent resistivities from July and September 2015 were inverted using the acquisition performed in July as a baseline for the time-lapse inversion. Both datasets were scanned to remove data points with large errors (differences of more than 10% between normal and reciprocal measurements), and compared to keep exactly the same electrode configuration in both acquisitions. For time-lapse inversion, the same set-up was preserved to ensure that the changes observed in time are only related to changes in the aquifer system and not to experimental artefacts. The inversion was made with BERT (Günther, Rücker, and Spitzer, 2006), which builds on PyGIMLi (Generalized Inversion and Modeling Library) (Rücker, Günther, and Wagner, 2017), a finite-element code that incorporates inversion with an iteratively regularized Gauss-Newton method coupled with local optimization of the objective function using the conjugate gradients method. The regularization includes a geostatistical operator that helped removing borehole footprints from the images, caused by the high sensitivity of the method around the electrodes. More detail on the inversion is described by (Palacios et al., 2020).

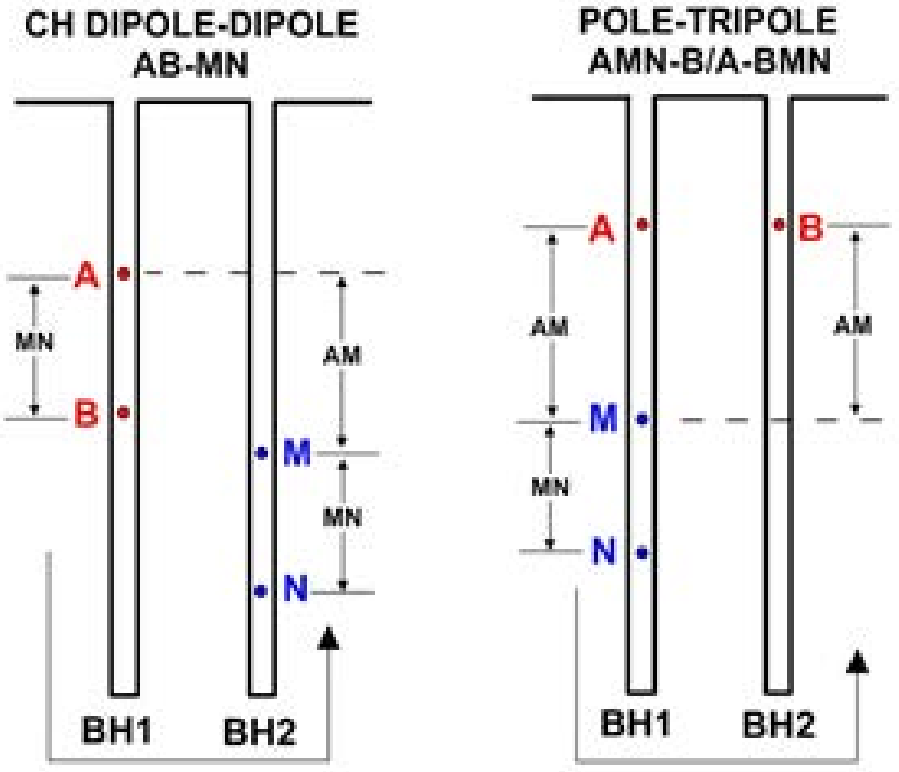

Figure 2.4: Electrode configurations for the acquisition of CHERT. A and B designate the current electrodes, and M and N the potential electrodes. In the cross-hole dipole-dipole array (CH AB-MN), the current electrodes are in the first borehole while potential electrodes are in the second borehole. In the cross-hole pole-tripole array (CH AMN-B/A-BMN), a current is imposed in the two boreholes while potential electrodes are in the same borehole.

Time-lapse induction logging (TLIL)

The EM51 downhole induction probe from Geovista® has the capacity to perform all measurements through PVC tubing in those cases where downhole measurements are complicated by the unconsolidated nature of the sediment. The sonde was deployed the 11^{th} and 12^{th} of May 2015 to measure formation electrical conductivity at meter-scale around piezometer N320. We choose this piezometer instead of N325 because of electrode interference with induction

measurements. Logging was performed in a repeated or so-called "time-lapse" manner over short amounts of time, with a period of 10 minutes between profiles. Compared with the aforementioned techniques, induction logging has shorter acquisition times, allowing to characterize variations in groundwater temperature and/or salinity at short time-scales. Only upward profiles were used in this study despite downward profiles were also recorded.

When comparing field surveys from July and September, the contribution of the conductivity of the grains was suppressed by using the following expression by H. Waxman and Smits (1968), in which the total formation conductivity is given by the sum of the conductivity of the pore volume and the pore surface:

$$C_o = \frac{C_w}{F} + C_s \tag{2.1}$$

where C_0 is the formation electrical conductivity (mS/m), C_W is the groundwater conductivity, F is the dimensionless formation factor and C_S is the surface conductivity of the pore space at the interface with mineral grains, typically associated to the presence of clay. The electrical formation factor F is a petrophysical parameter that depends on matrix porosity and pore connectivity and describes the efficiency of the fluid-filled pore-space to conduct current. As the Argentona site is close to the sea, groundwater conductivity is expected to be high due to salinity, and the term C_S can be considered negligible. Even if it was not the case, by computing the difference in conductivities between two surveys, and assuming that C_S is constant because the sediment remains undaunted, the conductivity changes observed in the time-lapse are only related to changes in pore fluid conductivity (C_W).

Fiber Optic Distributed Temperature Sensing (FO-DTS)

Temperatures were obtained from both fiber optic lines with an Ultima XT Distributed Temperature Sensor (*Silixa, UK*). Spatial sampling is set up at 25 cm, with a spatial integration length of 0.5 meter. The sampling period was set to approximately 1 minute, with an integration time of 10 to 30 seconds. Data sets collected in June 2015 had an integration time of 10 seconds. In order to keep consistency between June and September data, the June data were summed up every 30 seconds. The signal was calibrated using two reference baths of 57 L of water placed in a portable cooler *Ice Cube, Igloo, USA*). Temperature was homogenised with aquarium bubblers, and monitored with RBRsolo-T temperature loggers with and accuracy of 0.02 C *RBR, Canada*).

One of the baths, common to both lines, was kept at 0 C thanks to a well-mixed ice and water mixture, whereas a separate bath at ambient temperature was installed in each line.

Four different datasets were calibrated, one for each FO line (line 1 and line 2) and one for each field survey (June and September). The calibration approach was adapted to the peculiarities of each dataset: (1) The two datasets bellowing to Line 1 (June and September) were calibrated with the single ended calibration Hausner et al. (2016) as no anomalies were found in the fiber connections or calibration baths. (2) For Line 2 datasets, both June and September acquisitions presented different types of anomalies, forcing to perform the temperature inversion with different methodologies for each of them. In the case of the data gathered during June 2015 for line 2, no data from the thermometer monitoring the ambient temperature was available to perform the calibration. Moreover, the differential attenuation between segments of the fiber optic cable connected to form the complete line was different. These two issues prevented the use of a single-ended calibration as in the case of line 1 datasets. To solve this, we first had to correct the differential attenuation using another calibration point along the fiber optic line. We choose the screened interval of the 25 m depth piezometer N425. At this depth, the temperature remains constant for the monitoring period (hours), and we could use the temperature data recorded by the pressure-temperature sensor permanently installed at that depth. Secondly, we calculated the inversion parameters using the ice-bath and the new calibration point.

In the case of the data collected during the field campaign in September 2015 for line 2, the same problem related to the different differential attenuations between glass segments was solved. Moreover, only part of the reference thermometer data could be used. Thus, the temperature data was extrapolated to those acquisitions times where no temperature from the thermometer was available. This could be done since the monitoring period was small, thus changes in the bath temperature in time were negligible. So ,for this dataset double-ended calibration (Giesen et al., 2012) could be applied to account for the change in the differential attenuation.

2.4 Results

2.4.1 Cross hole electrical resistivity (CHERT)

The bulk conductivity (C0) cross-section perpendicular to the coast obtained by CHERT (Figure 2.5) shows a very flat SWI wedge located 2 m below a continuous layer of silt identified at 12 m depth. However, the higher spatial

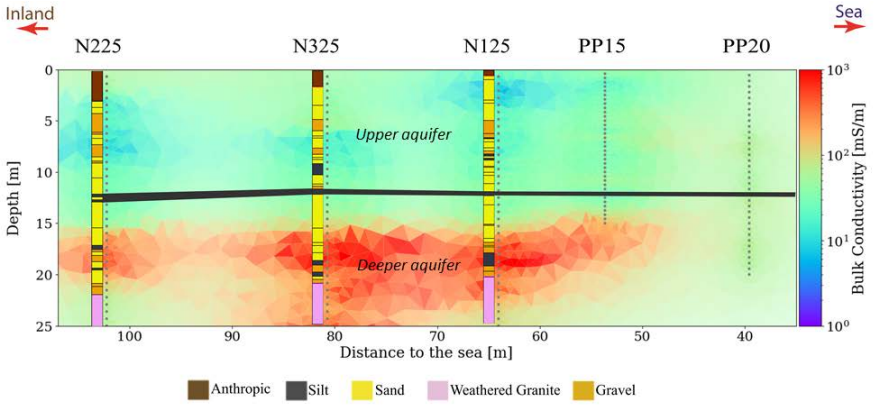

Figure 2.5: Bulk electrical conductivity model obtained from CHERT data. The anomaly in red, extending throughout the cross-section, 2 m below the continuous layer of silt placed at 12 m depth (in grey), indicates the presence of seawater in the aquifer. The stratigraphic columns of the Argentona site are displayed as a reference for interpretation.

resolution obtained with CHERT between wells PP15 and PP20 appear to indicate two different SWI areas, one in the upper part of the aquifer, close to PP20 and another one in the deeper part of the aquifer. These data do not correlate with the EC measured in the piezometers. Indeed, the EC measurements from fully screened piezometers (PP15 and PP20) show relatively constant values of EC between 4 and 12 m depth (Figure 2.6). Below this depth, there is a general continuous increase in EC towards seawater conductivities that does not correlate with CHERT data. Whereas EC patterns observed in PP15 and PP20 are likely to be artificially affected by the use of fully screened piezometers, further research is required to appropriately understand the difference on conductivity patterns derived from EC measurements in the piezometers and CHERT.

The higher spatial resolution obtained with CHERT allows differentiating two different mixing zones that could be indicative of two different discharging areas: a shallow one with a recirculation cell perhaps influenced by seawater infiltration from waves/storms, and a deeper one discharging away offshore. However, more data is required to verify these hypotheses, as the conductivity measured in the piezometers (Appendix A, Table A.1), shows higher values (i.e. lower resistivity) in the deepest part of the aquifer.

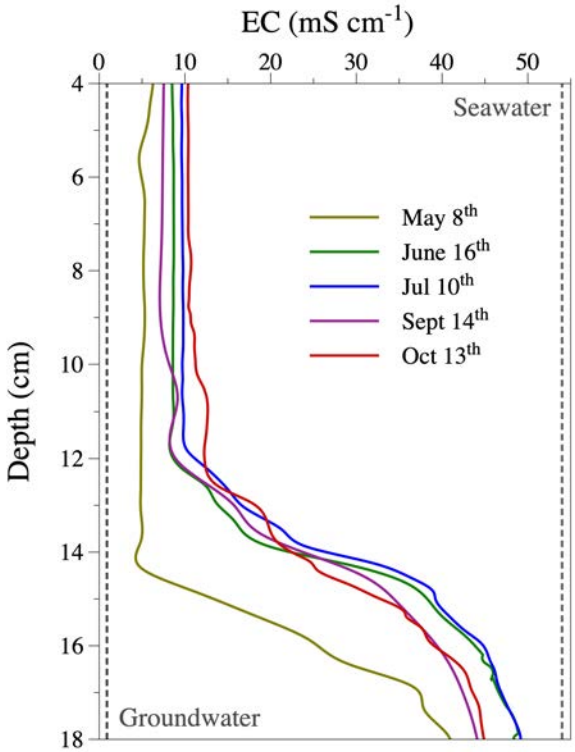

Figure 2.6: EC profiles recorded at the fully screened piezometer PP20 (Figure 2) in 2015. Fresh and sea water values are marked with a dashed line in the figure for comparison.

The ratio between the bulk electrical conductivity from June and September is a good tool to evaluate the seasonal variation in salinity (Figure 2.7). Whilst, ratios below 1 (color blue) indicate a decrease of conductivity, ratios above 1 (color red) indicate an increase. The maximum changes occur between 15 and 20 m depth, with a general increase in conductivity mainly in the coarser materials between the piezometers N3 to PP20. This trend is consistent with groundwater level evolution (data not shown) that tend to decrease between 2 and 4 cm between June and September. However, this evolution is not clear in the water electrical conductivity changes measured in the piezometers (Appendix A, Table A.1). There are changes along the vertical electrical conductivity profiles measured with the EC probe, most significant in June, due to the presence of sediments with different grain size that cause different flow

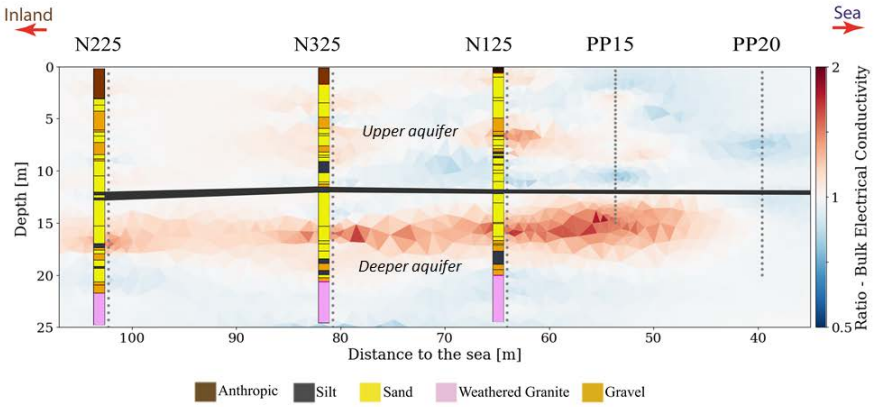

Figure 2.7: Cross-section of the bulk electrical conductivity (C_0) ratio between June and September 2015 CHERT surveys. The colour scale varies from a decrease to half of the value of C_0 compared to June 2015 (blue), to an increase by two in the value of C_0 compared to June 2015 (red). The main change during summer is a twofold increase in bulk EC observed 2 m below the silt layer at -12 m depth represented in grey. The stratigraphic columns of the Argentona site are displayed as a reference for interpretation

distributions along the 2 m screened intervals of most piezometers. Furthermore, compared with piezometers data, CHERT models shows the extension of the area affected by this increase of conductivity in the sands as well as in the weathered granite.

In the upper part of the aquifer there are no significant variations of conductivity as indicated by data obtained in the piezometers PP15 and PP20 (Appendix A, Table A.1), pointing out that a relatively stable SWI between June and September at shallow depths.

2.4.2 Time-lapse induction logging (TLIL)

Time-lapse downhole measurements were carried out in piezometer N320 only and at the onset of the dry season (May 2015). Downhole measurements are repeated every 15 minutes in the same hole, in a time-lapse mode, and surface conductivity (Cs) and formation factor (F) were considered constant (Equation 2.1). Consequently, changes in bulk electrical conductivity are attributed to changes in groundwater conductivity due to changes in pore fluid temperature and/or salinity with time.

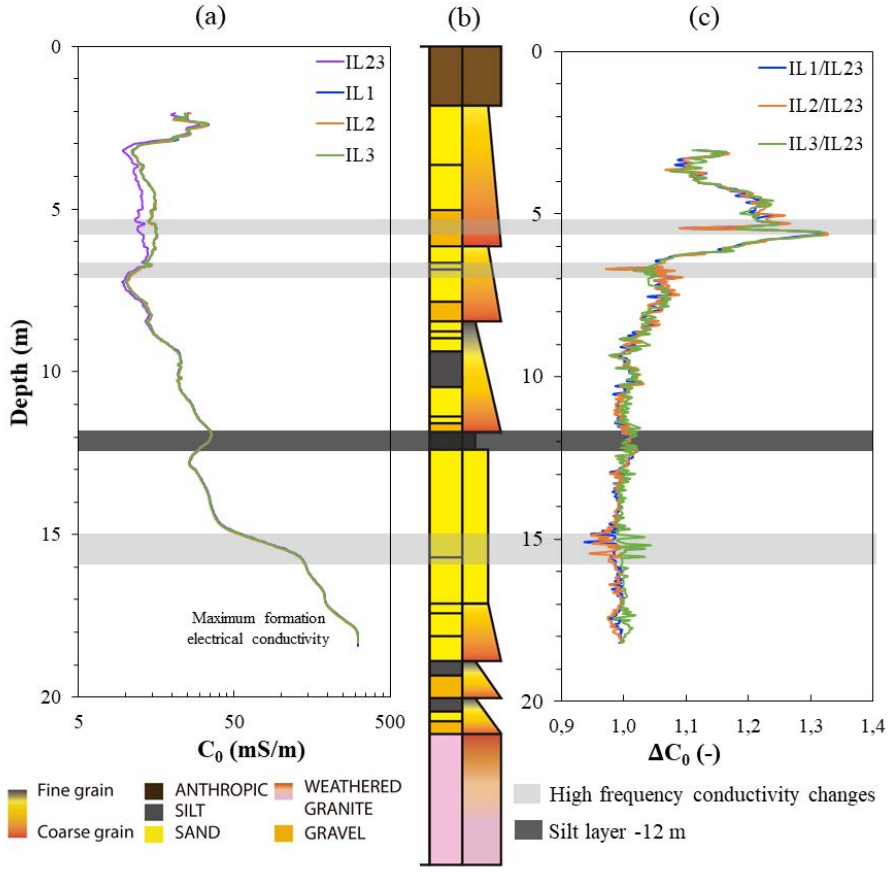

Figure 2.8: a) Downhole Induction logging (IL) profiles of formation electrical conductivity (C0) measured in borehole N320 (Figure 2.1) on May 11^{th}, 2015 (profiles IL1, IL2 and IL3) between 3:00 and 3:45 PM, and on May 12^{th}, 2015 at 11:30 AM (profile IL23). (b) Stratigraphic column of N325 (Figure 2.2) located 1.5 m away from N320 (c) Pore fluid conductivity ratios (ΔC_0), taking the May 12^{th}, 2015 profile IL23 as reference. Grey shadings across the entire figure point at levels where high frequency conductivity changes between profiles recorded on May 11^{th}, 2015 were detected

We considered that changes in formation conductivity (C_0) were directly proportional to changes in water EC, and therefore C_0 measured in May (Figure 2.8) correlate with groundwater EC measured a month later in the same piezometer (Appendix A, Table A.1). The maximum C_0 values were obtained

below 14 m depth, in agreement with piezometers data and the June 2015 CHERT acquisition/cross-section. In this way, groundwater at the top of the screened interval for N320 showed values in agreement with the conductivity of 13.3 mS/cm measured in this piezometer in June.

When considering C0 changes over short periods of time (10's of minutes), some depth intervals present significant changes between May 11^{th} and 12^{th}, 2015 (Figure 2.8a). Changes can be revealed by calculating pore fluid conductivity ratios (ΔC_0)) of each profile taking the May 12^{th}, 2015 profile (IL23) as reference. Close to the surface (from 3 to 9 m depth), were we can find fresher groundwater, all ratios exhibit a decrease in conductivities overnight, with changes up to 30% (Figure 2.8c, Pore fluid conductivity ratios (ΔC_0)). This decrease can be due to a decrease in groundwater temperature or salinity overnight, or both in the same time period. In the same depth interval, smaller changes of 5 to 10% are noticed between IL3 and IL4 (Figure 2.8c, orange and green profiles) that is in less than 15 minutes. These smaller changes appear in decimeter-thick intervals (near 5.5 and 6.5 m depth) and point at small changes in groundwater temperature or salinity in a very short time. These high frequency conductivity changes (grey sections in Figure 2.8) are attributed to the presence of preferential flow pathways with relatively high fluid flow at these depths. It can be noticed that the TLIL method identified small zones of preferential flow that cannot be identified with CHERT.

In the brackish to sea-water saturated region below 9 m depth, very little conductivity changes were registered, in occasions less than 0.5%. These horizons correspond to finer grained materials where fluid flow is troublesome. Between 14.5 and 15.5 m depth, noticeable changes up to 5% are measured over a meter-thick interval. These tiny changes underline the precision of TLIL measurements. Below 16 m depth (Figure 2.8c), no significant changes in C_0 are observed with TLIL.

2.4.3 Fiber Optic Distributed Temperature Sensing (FO-DTS)

Rather than presenting the results as temperature depth profiles, we choose to interpolate the data with a simple linear interpolation perpendicular to the sea to highlight the spatial patterns (Figure 2.9). Unlike the geophysical techniques, which provide a wider distribution of measures in the subsurface, FO-DTS data concentrates on several vertical lines. Therefore, the uncertainty of the interpolation is larger, and any future qualitative analysis would be better based on the un-processed temperature data (i.e. the vertical temperature depth profiles). However, interpolated plots allow a good qualitative analysed and comparison between the different techniques performed in this study.

The general distribution of temperature follows the same trend as piezometer measurements (Appendix A, Table A.1), with higher temperatures inland and lower closer to the sea (Figure 2.9). However, all temperatures measured in the piezometers are higher than those measured with FO-DTS. While the maximum temperature in groundwater according to the FO-DTS is below 19.40 C, several temperature measurements in piezometers are above this value. This pattern is observed in the wells with a 2 m screened interval as well as those completely screened (PP15 and PP20), where the complete cross-section tends to show higher temperature. The higher values measured in the piezometers compared with the distribution observed with the FO-DTS indicates that temperature in piezometers is significantly altered by atmospheric temperature. In contrast, the fiber installed in the annular space of the piezometers, measured temperatures much closer to the expected subsurface temperatures.

The highest influence of the atmospheric temperature is above the first 3 m depth, corresponding to the non-saturated zone. In this regard, the annual thermal oscillation extinction point was estimated to be less than 15 m depth applying the solution proposed by Stauffer et al. (2014) with the local atmospheric temperature in the period May-September 2015 (data not shown). Between June and September, this influence can be reduced to 12 m depth. Considering that neither the vertical nor the horizontal distribution of temperature underground is homogenous, different effects can condition groundwater temperature distribution. However, the small influence of atmospheric temperature on groundwater temperature at shallow depths indicate that groundwater flow in this area is relatively important, which is in accordance with the coarser grain of the materials found in the upper part of the aquifer.

In June (Figure 2.9a), the temperatures are generally lower than in September, showing more spatial changes in the upper part of the aquifer than at the bottom. It is clear that there are two sources of temperature anomalies relating to the coldest and hottest temperatures of the cross-section. The coldest anomaly located between N325 and N125 is attributed to the local effect of surface recharge from a discontinuous sewerage discharge channel close to the site, as also observed in temperature data from the N4 nest (data not shown) which is located close to this discharge area. The warmest temperature of the cross-section is observed in the inland part of the experimental site (between N225 and N325) highlighting the thermal effect of groundwater flow recharged inland. The coldest temperatures of the cross-section are measured at the deepest part of the aquifer at the bottom of a thick pack of sands below 18 m and close to the weathered granite. Since this is the most affected area by SWI, the coldest temperatures derived from FO-DTS data are related to the intrusion of colder seawater, in contrast with the warmer temperatures

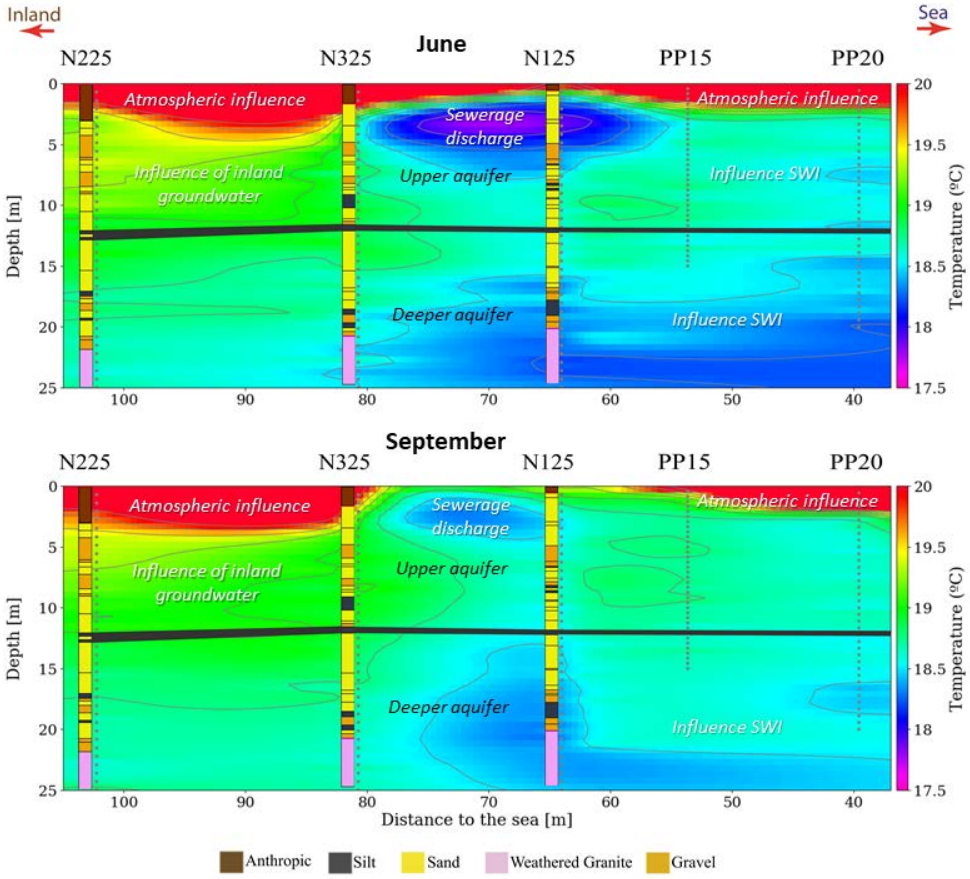

Figure 2.9: Thermal profiles of the June and September field surveys resulting from linear interpolation of data in each borehole. Temperatures above 20 C are all drawn with the same color. The stratigraphic columns of the Argentona site are displayed as a reference for interpretation. Grey layer indicates a continuous layer of silt that crosses all piezometers

observed inland. In this regard, the small areas with the coolest temperatures around at depth of 11 m, close to N125 and PP15, could also be indicating the presence of a shallower saltwater wedge.

In September (Figure 2.9b), temperature distribution is similar to June, but with slightly higher values. The non-saturated zone, as well as the deepest part of the cross-section, shows higher temperatures. As in June, the warmest temperatures are located at the innermost and shallow part of the aquifer and

the coldest temperatures at the deepest part of the aquifer, closer to the sea. However, there is a slight increase of the coldest temperatures in the deeper part of the aquifer, which could be related to the higher temperatures along the profile due to the dry season, an increase of sea water temperature, or both. In the same way, when considering only the shallow part of the aquifer, the coldest temperature corresponds to the part of the profile closest to the sea. However, during summer there is an increase in sea water temperature in the shallow depths that does not seem to affect the temperature distribution in the upper part of the aquifer in the closer zone to the sea.

2.5 Discussion and integration of techniques

The combination of techniques applied in the Argentona site allows describing the behaviour of the system at the beginning and at the end of the dry season. The shallowest part of the aquifer does not show important salinity changes during the studied period. On the other hand, the deepest part of the aquifer shows an increase in salinity over the season, mainly observed in the bottom part of the sedimentary formation. Despite the basement showing a high electrical conductivity, the values measured remain constant during the studied period (i.e. low flow). This lack of dynamism is in agreement with the low transmissivity obtained through short pumping tests (Martínez-Pérez et al. 2018, Internal communication). At borehole scale, induction logging revealed the presence of preferential flow paths at different depths.

Whereas each applied technique provides partial information of the coastal aquifer, the combination of techniques allows obtaining a comprehensive understanding of the characteristics and hydrodynamics of this complex system. CHERT and FO-DTS provide important information at the site scale, whereas TLIL characterizes the system at the meter-scale. With CHERT and FO-DTS data we can differentiate two behaviours in the aquifer. While CHERT identified the main active area of SWI intrusion occurring in the deepest part, FO-DTS does not show important changes between both surveys. However, FO-DTS and TLIL highlighted that the shallowest part of the aquifer is an active system with fresh groundwater flow occurring; a statement that cannot be made by looking only at CHERT.

The active area identified with TLIL in the deepest part of the aquifer at 15 m depth (Figure 2.8), corresponds to the upper part of the active area identified with CHERT (Figure 2.7). On the contrary, no significant changes are observed with TLIL below 16 m unlike what was found by CHERT. These differences between both methods could be related to the fact that both are deployed at different spatial and temporal scales. In this way, CHERT could point more to

seasonal changes, while TLIL may be related to more instantaneous changes. Whilst we cannot evaluate the capacity of CHERT to identify hourly or daily changes with the data collected, we infer that it would be possible to capture such changes with a proper experimental design that allows to acquire data with a high temporal frequency. More research is needed to understand this issue, increasing the number of points were Co is measured and/or by increasing the temporal frequency of CHERT profiles.

Despite the high density of piezometers in the field site, and the screening of the piezometer on only 2 m, these techniques provide higher spatial resolution than direct measurements. Furthermore, they can give more representative information of the SWI extent, especially CHERT. In this regard, CHERT data correlates relatively well with water electrical conductivity of most piezometers in the different locations and depths along the study site. However, CHERT provides a 2D representation of the shape and extent of the seawater intrusion and its seasonal variations. This information would be impossible to obtain using only point measurements from piezometers. This is particularly relevant in fully screened piezometers. Temperature measured with FO-DTS in the annular space of the boreholes (i.e., closer to the aquifer matrix) is lower than temperature measured in the piezometers, pointing out the influence of atmospheric/soil conditions on groundwater measurements from piezometers.

The changes in formation electrical conductivity measured with TLIL may indicate preferential flows at a smaller scale than the other techniques, giving information that cannot be obtained and/or approximated with traditional monitoring methods. Only tracer tests in the screened intervals could generate similar data but with lower spatial and temporal resolution, and at higher costs.

The study site is located in the Mediterranean basin and therefore subjected to a microtidal regime. In other oceanic coastal areas, the effect of tides is more significant and can influence the dynamics of the system. It is expected that in open sea areas the applied methods could improve the characterization of the system. That is particularly relevant for the FO-DTS, as higher tides increase the dynamism of the SWI, increasing the thermal influence of the sea boundary condition on the aquifer. This assumption could explain why the influence of the sea has been found to be minor in this study, despite various studies indicate that temperature can be used as a useful SWI tracer. In the same way, the application of this technique in those areas with important thermal contrast between sea and groundwater temperature could give better results. Finally, the connection to the sea and the thermal properties of the geological materials could limit the application of this technique.

2.6 Conclusions and future challenges

Different approaches and techniques (direct groundwater measurements from piezometers, CHERT, FO-DTS and TLIL) have been combined for the first time to study a 25-m thick microtidal coastal aquifer during the dry season (before and after summer 2015). CHERT profiles allow a better definition of the shape and distribution of the seawater intrusion, as well as its seasonal changes, than data obtained from point groundwater measurements from piezometers. In this case study, the combination of the different techniques has allowed improving the understanding of the hydrogeological system by: 1) A proper characterization of the extend and shape of the SWI, 2) differentiating two different zones with different dynamics in the deep and upper part of the aquifer and 3) identifying preferential flow paths over different time and spatial intervals. The distribution of the SWI does not follow the typical shape, with main changes between 15 and 18 m depth. Despite minor changes in salinity measured in the shallower part of the aquifer, data provided by TLIL and FO-DTS indicate that it is an active system.

Although precise characterization of the aquifer was achieved by combining different geophysical techniques, the groundwater discharge process to the coastal sea (i.e. SGD) is still a challenge. Considering the information obtained from the techniques applied, there are two different mixing zones that could be related to two different discharge areas: a shallow recirculation cell closer to the sea, mainly influenced by wave setup and storm effects (in addition to the terrestrial hydraulic gradient), and a deep discharge area, acting at a more seasonal scale, and likely discharging offshore. However, the extension of the discharge of the deep aquifer into the sea is not fully clear. More data are required to fill the blank between the site and the sea, but also inland, to improve the understanding of the system. Yet, a higher temporal and spatial resolution of the already applied techniques will also improve the understanding of the system considering the following:

- Higher temporal resolution of CHERT would allow understanding how mixing is occurring and the origin of salinity in the shallow part of the aquifer (convective zones, wave effect, etc.). At the same time, higher temporal resolution would allow understanding why at the end of the dry season there is a decrease of salinity simultaneously with an increase of salinity in the deeper part of the aquifer.

- TLIL could be applied in more piezometers at the same time to study the changes in conductivity and check whether these changes correspond

to preferential flows at decimeter scale. In the same way, using this technique with higher frequency could allow understanding if these potential preferential flow paths respond to to the heterogeneity of the system and/or the recharges/discharges processes occurring at different temporal scales (storms events versus seasonal dynamics).

- FO-DTS has allowed obtaining more information in areas with no TLIL data and/or where the conductivity changes are not significant to obtain representative data with CHERT. Nevertheless, only minor differences between both surveys are measured. Therefore, the potential use of temperature as a tracer using FO-DTS needs to be evaluated for a longer period of time as its distribution is significantly affected by the thermal characteristics of the boundary conditions (atmosphere, recharge inland, sea, etc.) and therefore changing along seasons. In this way, it is important to consider that the boundary conditions tend to change in a similar way along seasons but with some lag and different extreme values.

Although more research is needed, the application of the presented techniques in a well-characterized study area such as the Argentona site has allowed describing the effectiveness of FO-DTS, CHERT and TLIL to characterize coastal areas dynamics. This information has pointed out the potential of these techniques to be applied in other areas. In this way, the best technique to use when characterizing coastal aquifers dynamics will depend on the temporal and spatial resolution required. The importance of fresh water flow in the system can also indicate which methods should be combined and the amount of data that is required. The structure of the aquifer (unconfined/confined vs multilayered aquifer), and the boundary conditions (recharge patterns, thermal contrast between boundaries, etc.) can also condition the combination of techniques to be used. Lastly, studying zones in small basins as the Mediterranean or on the contrary in open ocean conditions, will also influence the approach to apply due to the different dynamics of coastal aquifer in both areas. In all cases, the electrical conductivity and temperature data obtained with the CHERT, FO-DTS and TLIL is expected to be more representative than the same data obtained in the piezometers.

Chapter 3

Interpretation of a coastal aquifer pumping test: removing noise and natural head fluctuations

In this chapter we propose a methodology to filter out natural head fluctuations and noise from a coastal aquifer pumping test data. The work is motivated by the need to interpret a pumping test at the Argentona experimental site (NW Barcelona), where small drawdowns were superimposed to tidal and other head fluctuations that obscured the actual response to pumping. The approach for the interpretation of the pumping test consist on six steps: (1) select environmental components of the natural water-level; (2) calculate the drawdown by reconstructing the natural heads during the pumping test using a linear multiple correlation approach; (3) define drawdown curves from pumping and recovery phases to compare and validate the method; (4) prepare diagnostic plots and remove noise using the smooth log-derivative method; (5) use these plots and geological understanding to define the conceptual model; and (6) estimate hydraulic parameters. This approach allowed us to derive drawdowns free of natural trends and noise, while validating the results from the filtering process. The interpretation provides remarkably consistent results.

3.1 Introduction

This work is motivated by the need to characterize the Argentona research site located NW Spain (Folch et al., 2020; Martínez-Pérez et al., 2020). As part of the characterization, we carried out a two days long pumping test. However, its interpretation was hampered by the small drawdowns and the interference of environmental head fluctuations, such as sea tides, which obscured the actual response to pumping. In consequence, we needed an approach to deal with these complex data.

The problem is not exclusive of our site. Large hydraulic conductivities causing small drawdonws are frequent in unconsolidated aquifers.Tidal and wind-driven sea level fluctuations, as well as punctual storm surges, strongly affect groundwater heads close to the coast. In some cases, environmental fluctuations larger than drawdowns occurs, complicating their interpretation. This problems should be frequent in coastal aquifers. And, yet, pumping test analysis is one of the most important methodologies for the assessment of the hydraulic properties of the aquifers (Almeida and J. J. L. Mendonça, 2017).

Pumping test data can be interpreted in different ways. The most straight approach in a complex situation might be to build a numerical model that integrates all the complexity (Calvache et al., 2015; Zhou, Qiao, and Li, 2017; Alcolea et al., 2007). However, the construction of a comprehensive numerical model is demanding and requires information about the hydraulics of the system. In fact, beyond yielding the value of hydraulic parameters, pumping tests are useful to complement geological understanding to define the conceptual model or, at least, to identify the processes that affect the hydraulic response to pumping. This is why pumping test interpretation usually concentrates on analysing drawdowns caused by pumping using analytical solutions rather than numerical models. In this context, diagnostic plots (plots of drawdowns and their derivative with respect to log-t) are extremely useful to identify the conceptual model (Bourdet et al., 1983; Renard, Glenz, and Mejias, 2009).

Diagnostic plots and many other analytical methods require working with drawdowns (i.e., changes in head caused by pumping). The actual measurements are affected by environmental head variations. Thus, environmental variations have to be subtracted from measured heads to obtain drawdowns. To formalize the concept, we distinguish between measured heads (heads that have been measured at piezometers) and "natural heads" (heads that would have occurred if the pumping tests had not been performed). Drawdown can then be defined as the difference between natural and measured heads during pumping. Since natural heads cannot be observed, they have to be reconstructed, which is a common step in pumping test interpretation (Kruseman,

Ridder, and Verweij, 1994).

Reconstructing natural heads is a frequent task and numerous methods are available to do it. Natural head reconstruction could be process-based (e.g., using a numerical model). But most methods are based on data-driven models, possibly bearing a conceptual model in mind (e.g., if one assumes head fluctuations to be caused by tides, one would expect natural head fluctuations to be a dampened and delayed version of the tide signal).

Within the data-driven models we can find methods that reproduce periodic trends, here called spectral analysis methods (Sánchez-Úbeda et al., 2016). Others, like the classical regression models (Halford, 2006; Kruseman, Ridder, and Verweij, 1994) or the new generation of machine learning and artificial neural networks methods (Coppola et al., 2005; Amaranto et al., 2019) are able to handle all types of trends. Regression models are probably the most intuitive to use for their simplicity. In this line, Kruseman, Ridder, and Verweij (1994) suggests to reproduce unique fluctuation (i.e. recharge) by reconstructing the natural head, by correlating the unperturbed groundwater levels with a distant well. Halford (2006) and Halford et al. (2012) offers a much more comprehensive approach. He designed a simple spread sheet to estimate water-levels unaffected by pumping during aquifer tests, so that they can be substrated from the measured heads. To do so, he first generated synthetic times series for each component of the water-level. Then he adjusted the amplitude and phase of each time series until the synthetic natural heads match the measured ones during periods unaffected by the pumping test(Halford, 2006). This is done by minimizing the differences between the synthetic and measured water-levels time series.

To our knowledge, most of the publications addressing the interpretation of pumping test performed in coastal aquifers, focus on dealing with the effect of the rhythmic fluctuation of tides by integrating it in their analysis rather than removing it from the measured heads. Therefore, they are considering tides the only, or at least most important, environmental process affecting measured groundwater heads. Some of these approaches propose analytical solutions integrating the effect of tides, thus analyzing the measured head instead of the drawdown (Almeida and J. J. L. Mendonça, 2017; Chapuis, Bélanger, and Chenaf, 2006). Others, propose the use of numerical models to do the same (Alcolea et al., 2007; Zhou, Qiao, and Li, 2017; Calvache et al., 2015).

Groundwater heads complexity increases with the combination of multiple type of environmental fluctuations, like sudden recharge events or storm surges. Therefore, additional approaches are needed to interpret coastal aquifer pumping tests which are affected by more environmental fluctuations than just sea tides. From the reviewed literature, Halford et al. (2012) provide the most

simple and comprehensive approach to reconstruct complex natural groundwater heads, so that drawdowns can be calculated. We will draw from Halford et al. (2012) approach, and expand it with additional steps to account for the noise removal and the possibility to validate the resulting drawdonws with the recovery data. The proposed approach will be tested to interpret the pumping test carried out in Argentona research site.

3.2 Methods

This section describes all steps we did in order to obtain the hydraulic characterization of the Argentona site based on a pumping test. First, the research site will be briefly introduced, including the background monitoring strategy and the pumping test procedure. Second, the proposed procedure for the estimation of the drawdown will be described: (1) filtering environmental water-level oscillations; (2) defining drawdown curve from pumping and recovery data; and (3) generate diagnostic plots using smooth log derivative to remove high frequency noise. Thirdly, the approach to define a conceptual model will be introduced. And finally, the method chosen for the estimation of the hydraulic parameters will be explained.

3.2.1 Hydraulic test

The Argentona field site is located North of Barcelona (Catalonia, Spain) (Figure 3.1a), at the river mouth of an ephemeral stream, which remains dry most of the year. River discharge only occurs as fast floods during extreme rainfall events. The site is situated on top of an unconsolidated aquifer, formed by alternating layers of sand/gravel and clay/silty sediments, with impermeable granite at the bedrock (Figure 3.1c). The alternation of permeable and impermeable material is believed to cause several semi-confined levels. The continuity of the clay/silty layers is not known.

The site was equipped with sixteen piezometers (Figure 3.1b), with a 2 meters screened interval ranging between 10 and 20 meters below surface (Figure 3.1c). All piezometers were equipped with pressure sensors that collected data continuously every 15 min as part of the background monitoring of the site. Background heads were also monitored in a borehole located some 300 m upstream of the site (Figure 3.1a). This borehole will serve as reference for the natural regional head fluctuations. The background monitoring data was used during reconstruction of the natural heads.

The pumping test was designed based on the analytical interpretation of previous shorter (4h) pumping tests and the interpretation of the lithological

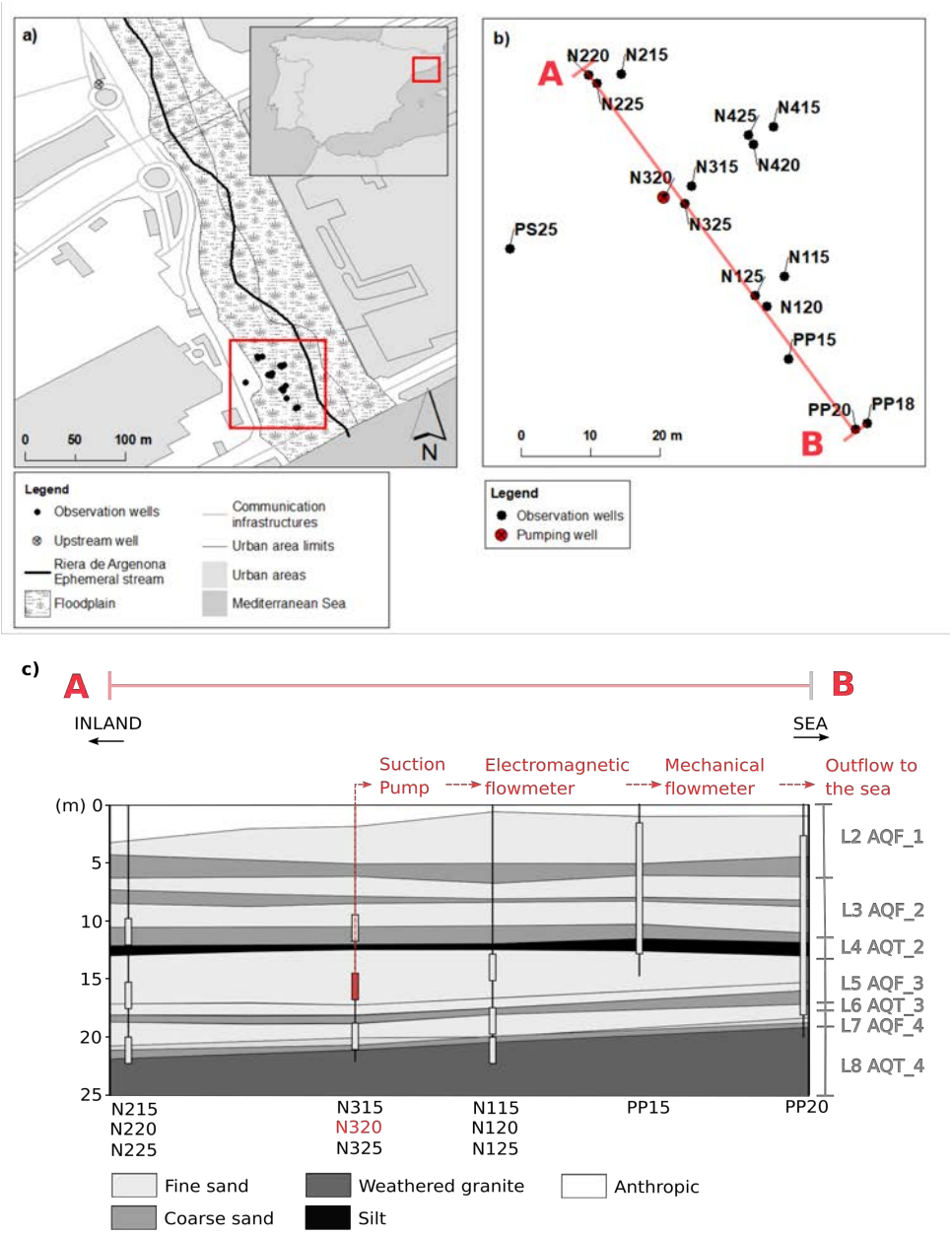

Figure 3.1: Field site location and borehole distribution. a) Map of the location of the field site including upflow monitoring well. b) Distribution of monitoring wells along the experimental site, highlighting the borehole used for pumping. c) Simplified vertical cross-section perpendicular to the sea indicating mayor lithologies and screened intervals (Modified from (Martínez-Pérez et al., 2020).

borehole descriptions (Martínez-Pérez et al., 2020). The pumping test was designed to last for two days aiming to reach the steady state. The diameter of the piezometers (3") did not allow to install a submersible pump with sufficient flow rate. Therefore, a suction pump (*SD150/2, Foras Water Pumps, Italy*)was installed. This pump yielded a flow rate of 4 l/s (the maximum suction elevation was some 7 m). Pump outflow was measured in three ways: (1) with an electromagnetic flow meter (*MS2500, ISOIL, Italy*); (2) with a mechanical flow meter; and (3) manually with a bucket. Despite the lost of pressure during the first minutes of pumping, outflow was kept relatively constant ranging between 4 to 3.9 l/s. During the pumping and recovery, sampling frequency of the pressure sensors was increases up to 2 min.

3.2.2 Filtering environmental head fluctuations

We reconstructed the natural heads using a multiple linear regression during the period before and long after pumping. In essence, we try to reproduce the observed heads as a linear combination of time series that represent the various contributions to head fluctuations:

$$h^*(t) = \sum a_i f_i(t) \tag{3.1}$$

Where a_i is the i-th regression coefficient, associated to time series $f_i(t)$ (regional groundwater levels, direct recharge through the top and the sea level). This approach is similar to the one recommended by Halford et al. (2012). However, rather than using synthetic approximations of each environmental head fluctuation component, we used measured time series. The regression was done using four weeks of data unaffected by pumping (two weeks before the start of pumping, and two weeks after the stop, starting after three times the duration of pumping). Details on the regression procedure and the collection and processing of the time series for each component are explained below.

Environmental water-level fluctuations

- *Mean sea level*

  Mean sea level time series from the tide gauge of the Barcelona port, were provided by the Spanish national port authority (Puertos del Estado) (red line in Figure 3.2b). This is the closest tide gauge to the research site. Data is provided with a frequency of 5 min, which was averaged to 15 min to match the sampling frequency of the background groundwater monitoring. We not only consider periodic fluctuations of the mean sea

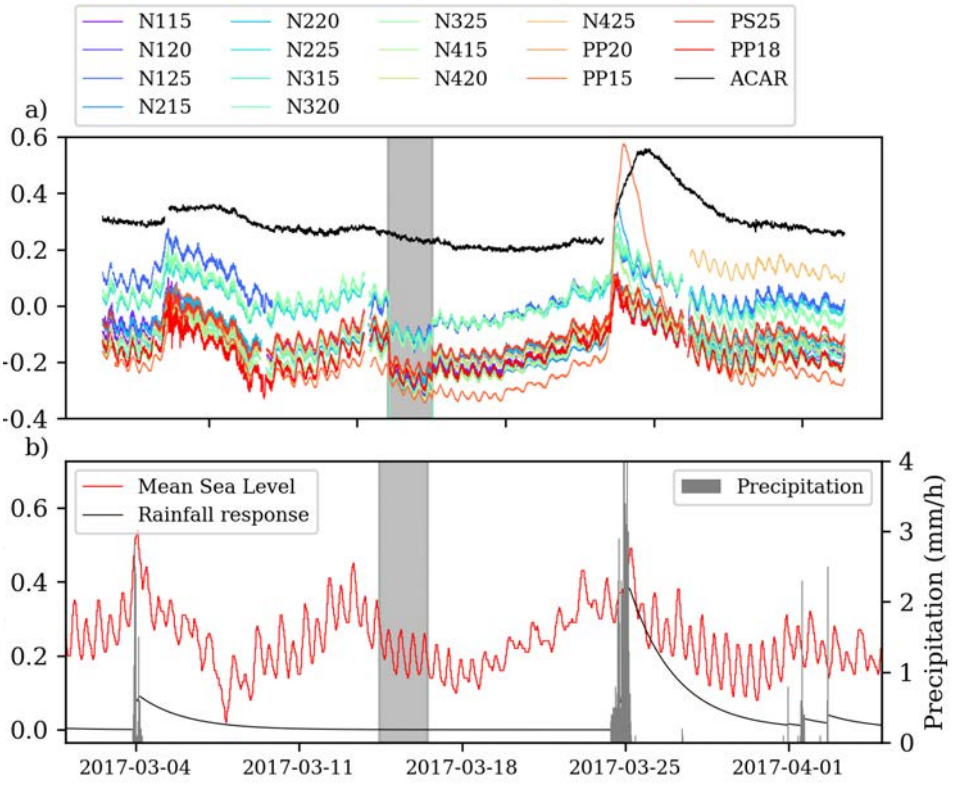

Figure 3.2: Time series measured heads and environmental processes affecting water-levels. a) Groundwater heads expressed as meters below surface of all monitoring wells. b) Mean sea level at the Barcelona Port tide gauge (in red) (Puertos del Estado, precipitation (grey) (MeteoCat) and rainfall response as estimated with Equation 3.2 (black).

level, like astronomic tides, but also wind driven sea level fluctuations and singular oscillations, like storm surges.

- *Rainfall response*

  Meteorological data is available at the near-by meteorological station of Cabrils, a small town located 7 km from the research site (grey line in Figure 3.2b). Precipitation data from this station was used to estimate the attenuated response of the groundwater levels to the precipitation

falling on top of the site (black line in Figure 3.2b), which are then used as another environmental component in the regression.

$$h_{P(t_i)} = \frac{P_e - P_0}{t_r} e^{-(\frac{t_i - t_e}{t_r})} \tag{3.2}$$

where P_e is the precipitation during each rainfall event, P_0 is a rainfall threshold for recharge, t_r is the response time, t_i is the time and t_e is the time each rainfall event starts. This equation is equivalent to that used by Halford et al. (2012) as the "Gamma Transform", if n is considered 1.

- *Regional oscillations*

  We use the term regional oscillations to describe head fluctuations attributed to other unaccounted effects (long term recharge fluctuations, pumping in distant wells, etc.). Regional oscillations were included in the multiple regression as the time series of heads recorded in a distant well (black line in Figure 3.2a). The resulting time series do not show influence of high frequency sea tides, or the pumping test. They do reflect changes in recharge patterns, and the influence of low frequency (long period) sea level oscillations.

Water-level model

- *Time lag optimization*

  Prior to the regression analysis, the time lag between the identified environmental water-level components and each piezometer heads was optimized. To do so, we first separated the daily and semi-diurnal astronomical tides component from the tide gauge and piezometers groundwater heads time series. We did this applying a low-pass filter of 12 and 24 hours. Then we optimized the lag between the diurnal and semi-diurnal components of the sea and each borehole separately. We did the same for the rest of frequencies, thus for those larger than 1 day. We repeated this process separately for each borehole with the rainfall response, regional levels and remaining components of the sea tide respectively. The resulting optimized values were used to correct the lags with respect to each borehole of the environmental water-level components time series introduced in the multiple linear regression. To increase the degree of freedom in the regression a window of 5 hours was applied to the optimized time lags. In this way, for example, several time series for the

mean sea level with different lags around the optimized one were included in the regression, so that:

$$f_{sea,i}(t) = f_{sea}(t - \delta_i) \tag{3.3}$$

$$\delta_i = \delta_0 + \Delta\delta_i \tag{3.4}$$

where $f_{sea,i}(t)$ is each function representing, in this case, the sea level component introduced in the regression, f_{sea} is the time series of original data, in this case, the means sea level obtained from the tide gauge, δ_0 is the optimized time lag, $\Delta\delta_i$ is the time window used to add more time lags around the optimized one, and δ_i represents each of the lags applied to the time series original data in order to obtain a set of time series representing, in this case, the contribution of the sea to the natural head oscillation.

- *Multiple linear regression*

  A multiple linear regression was performed for the unaffected groundwater heads of each borehole, with the previously mentioned environmental components of the water-level. To do so, we used the *LinearRegression* function from *sklearn* package of *Python*. Correlation factor between reconstructed natural groundwater heads and the measured groundwater heads during the unaffected period give an indication of the accuracy of the drawdown estimation.

- *Estimation drawdown*

  The resulting regression parameters are used to reconstruct the natural heads during pumping and recovery at each observation well using equation 3.1. The regression parameters are applied to the environmental water-level components during pumping and recovery. These natural heads are subtracted from the measured heads to calculate drawdowns.

3.2.3 Defining drawdown curves

The method described above is somewhat cumbersome and the choice of fluctuation components $f_i(t)$ in 3.1 is conceptually subjective. Errors can occur in the computations and/or the choice of time series. It is convenient to be able to validate the computed drawdowns. To this end, we take advantage of the fact that drawdown curves can be computed from residual drawdown data during recovery (Agarwal, 2004; Trabucchi, Carrera, and Fernàndez-Garcia, 2018). We can then compare the drawdown curve of the pumping period with

the equivalent curve computed from residual drawdowns using Trabucchi, Carrera, and Fernàndez-Garcia (2018) methods.

3.2.4 Filtering noise with smooth log derivative method

Besides the effect of environmental water-level fluctuations, large noise is also an obstacle to the interpretation of pumping tests. In coastal unconsolidated aquifers, where large permeabilities are usually present, it is difficult to generate large draw-downs that overcome the effect of the instrumental error. As a consequence, subtle changes in the drawdown due to changes in the flow regime, may be hidden behind the noise produced by resolution of the pressure sensors. These changes are important for the identification of the conceptual model using diagnostic plots.

We use the method of Ramos et al. (2017) to calculate smooth log-derivatives (derivative of drawdown with respect to log-t). The drawdowns computed from this log-derivative are effectively noise-free. This approach is specially suitable for pumping test de-noising.

3.2.5 Defining a conceptual model

Diagnostic plots are constructed by plotting together drawdowns and their log-derivatives versus time, both in semi-log and log-log scales (Renard, Glenz, and Mejias, 2009; Ferroud, Rafini, and Chesnaux, 2019; Bourdet et al., 1983). These plots are a well-stablished tool in the petroleum and hydrogeology fields for pumping test interpretation.

Log-derivatives are the slope of the drawdown in a semi-log plot. They are useful to identify subtle trends in the drawdown data. These are indicative of the aquifer geometry and the evolution of the flow regime towards the pumping well. Renard, Glenz, and Mejias (2009) provides a set of the most typical diagnostic plots based on the these derivatives.

Log-log plots of the drawdown derivatives provide further sensitivity to the subtle fluctuations of the drawdown. Ferroud, Rafini, and Chesnaux (2019), in a similar fashion as Renard, Glenz, and Mejias (2009), provides a series of synthetic cases that can serve as example for the interpretation of these plots. In their approach, they emphasized in the sequential interpretation of these plots, where several flow regimens may be concatenated. The resulting conceptual model should provide a consistent explanation for the sequence of flow regimes, which they define as the specific forms of transient response of the aquifer to pumping.

We use both semi-log and log-log plots to deduce the underlying conceptual model driving the aquifer response to the pumping test. Once this is done,

the selection of the the most suitable method to quantitatively interpret the drawdown data becomes easier and more accurate.

3.2.6 Estimating hydraulic parameters

Due to the vertical complexity of the aquifer anticipated from the lithological borehole descriptions and the diagnostic plots (presented in the results section), we decided to use a simple numerical model to estimate the hydraulic parameters. We implemented the model in TRANSIN (Medina and Carrera, 1996), a 3D finite elements code for groundwater flow modelling.

TRANSIN also solves the inverse problem (Medina and Carrera, 2003). We used it to estimate hydraulic conductivity values for each layer in the model. The inverse problem minimises an objective function, which considers the error between the observed and modeled drawdowns.

The model geometry is a simplification of the reality. We assumed that horizontal layers are continuous and parallel in all directions. We assumed that there are no barrier (positive or negative) that could influence drawdowns (this assumption is supported by the diagnostic plots discussed in the next section). These assumptions allow us to model the domain as 3D with radial symmetry around the pumping interval. Thus, the model domain is 23 m high (the depth to the impermeable granite bedrock) by 1000 m long (enough distance to avoid interference of the boundary conditions). The horizontal axis represents the radial coordinate. The layer distribution is a result of the joint interpretation of the lithological borehole description and diagnostic plots (Figure 3.3). Pumping flux was distributed along the 2 meters of pumping well screen to the left site of the model. Top, bottom and right sides of the model are considered no flow.

Observation points were treated as a point located within the 2 meters of screen interval. The vertical coordinate of the point was selected to ensure that it belonged to the adequate layer, so as to correct possible offsets resulting from the vertical simplification of the model layers with respect to the reality.

3.3 Results

3.3.1 Drawdowns calculation

As mentioned in the introduction, head response to pumping was obscured by the influence of external environmental processes affecting measured heads. Figure 3.2 shows the recorded time-series of heads, mean sea level and precipitation before, during and after the pumping test. It can be observed that head

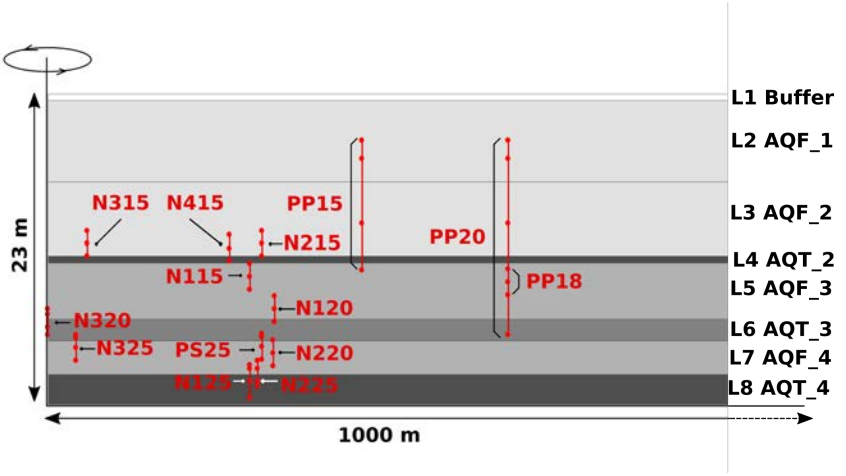

Figure 3.3: Model set-up including simplification of horizontal layers and location of observation points for each observation well in the installation. The red lines indicate the length and position of the screened intervals for each borehole. The red dots indicate the observation points in the model.

drops at observation wells range between 5 and 10 cm, except the pumping well (N320). These drops are of the order of magnitude of the amplitude of tides (10 cm), and much smaller than the amplitude of response to rainfall (5 to 50 cm) or storm surges events (10 to 30 cm). Therefore, rather than periodic, some of the most interfering components of the water-level are singular fluctuations.

Table shows the correlation factors obtained during the multiple linear correlation. Most of them are larger than 0.98, which is a good fitting. We ignored all those boreholes which correlation factors where lower than 0.98.

The resulting regression was used to reconstruct the natural heads during pumping and recovery (Figure 3.4). It can be observed that some of the boreholes presenting lower correlation coefficients (N120, N220 and N325) show a small off-set between the measured and natural groundwater heads. This prevents the drawdown from being centered in zero. This effect may be caused by step trends in the groundwater heads time series used during correlation. Moreover, larger errors are concentrated around the the response to rainfall events. Luckily, large part of the recovery occurs before the rainfall event on March, 25th.

The drawdowns resulting after removing the environmental trends from the measured heads are still too noisy and difficult to interpret. To remove this

Table 3.1: Correlation coefficients and Root Mean Square Error (RMSE) for reconstructed natural groundwater heads before and after the pumping test.

Well	Correlation	RMSE (m)
N115	0.98	0.00014
N120	0.97	0.00022
N125	0.98	0.00015
N215	0.99	0.00017
N220	0.96	0.00028
N225	0.98	0.00010
N315	0.98	0.00023
N320	0.96	0.00018
N325	0.96	
N415	0.99	0.00015
PP15	0.98	0.00046
PP18	0.98	0.00015
PS25	0.98	0.00010

noise we use the smooth log-derivative on the curves obtained during pumping and recovery. Both drawdown curves match quite well (Figure 3.5). This indicates that the filtering procedure was consistent. The comparison between the two log-derivative curves is especially enlightening. Log-derivatives highlight changes in the slope of the drawdown curve, thus informing about possible changes in the flow regime. But they are not sensitive to systematic errors and off-sets. The excellent match between derivatives indicates that despite occasional off-sets, both pumping and recovery display the same behaviour. This means that the off-set is probably an artefact of the initial time considered when correcting the recovery phase, or by a step trend in the input time series to the correlation. In any case, comparison between drawdowns calculated with the pumping and recovery phases are useful tools to check the validity of the filtering procedure.

In summary, we find that the multiple regression was a correct decomposition procedure. This can be surmised from the low RMSE and high correlation coefficients. However, the comparison of pumping and recovery drawdowns represents a much more informative validation, as it allows us to discern if the error may affect the validity of the conceptual model derived from the data. This confirms the additional utility of the smooth log derivative to denoise pumping test data. The good fitting between the two drawdown curves for most of the observation wells, indicates that the proposed methodology is

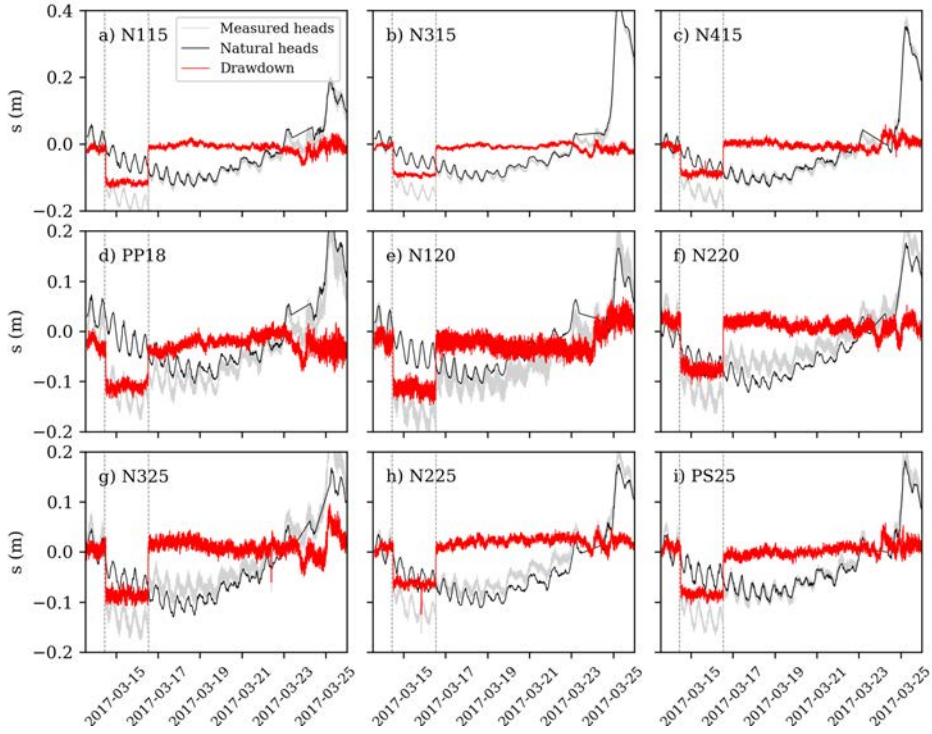

Figure 3.4: Drawdown resulting from subtracting the reconstructed natural groundwater heads from the measured groundwater heads for each borehole: measured heads (grey), reconstructed natural heads (black) and the filtered drawdowns (red)

robust.

3.3.2 Conceptual model

One of the objectives to carry out a pumping test is to gain information about the conceptual model of the aquifer. Bearing in mind this objective, we built diagnostic plots with the average between the drawdowns calculated with the pumping and recovery phases (Figure 3.6). The interpretation of the resulting semi-log and log-log drawdown and log-derivative plots is largely based in Renard, Glenz, and Mejias (2009) and Ferroud, Rafini, and Chesnaux (2019) methodologies respectively.

Log-derivatives plotted en semi-log scale are shown in the left column

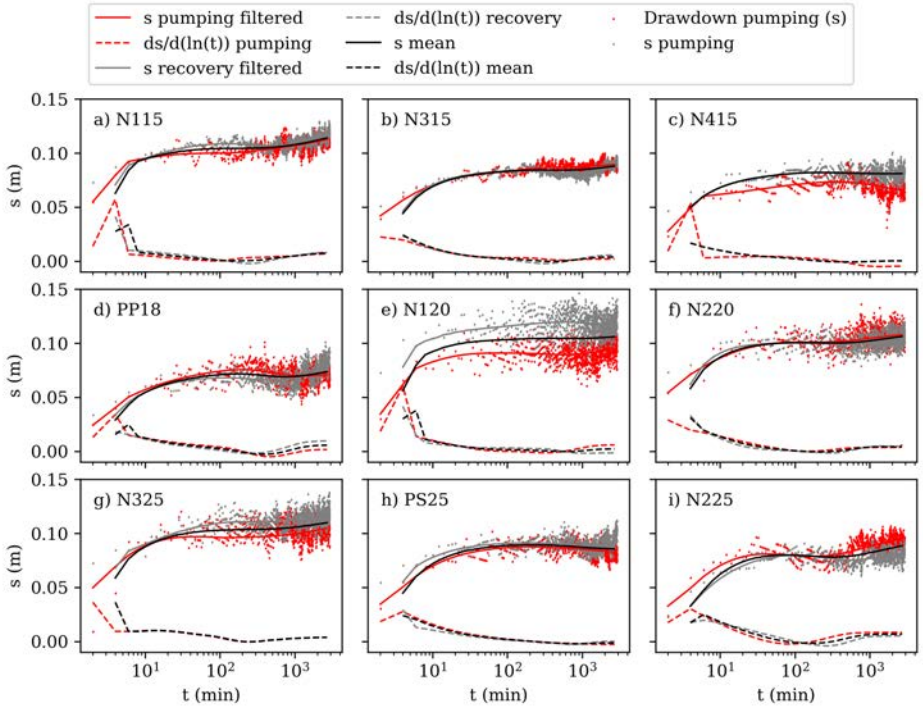

Figure 3.5: Drawdown (full line) and log-derivative (dashed line) curves obtained after noise removal with smooth log derivative method for the pumping period (red), derived from the recovery period (grey) and average between both (black) Dots indicate the original drawdown data.

of Figure 3.6. All boreholes display a similar behaviour. Early time log-derivatives are large and they decrease to values close to zero around 0.1 days. Then, they start to increase again and tend to stabilize after one day of pumping. The zero drop in derivative at intermediate times can be attributed to delayed yield (Boulton, 1954; Neuman, 1972) or to leakage across an aquitard (Hantush, 1956; Neuman and Witherspoon, 1972). The pumping interval is located between two silt layers. Therefore, we conclude that leakage through these semi-confining layers is the most likely explanation, as vertical connectivity tends to dominate pumping test responses.

The log-log plots may be more helpful to visualize flow regimes. Three flow regimes can be distinguished in most of the boreholes. First, the -1/2 slope of the log-derivative in log-log scale indicates spherical flow towards the pumping interval (Renard, Glenz, and Mejias, 2009; Barker, 1988). An initial

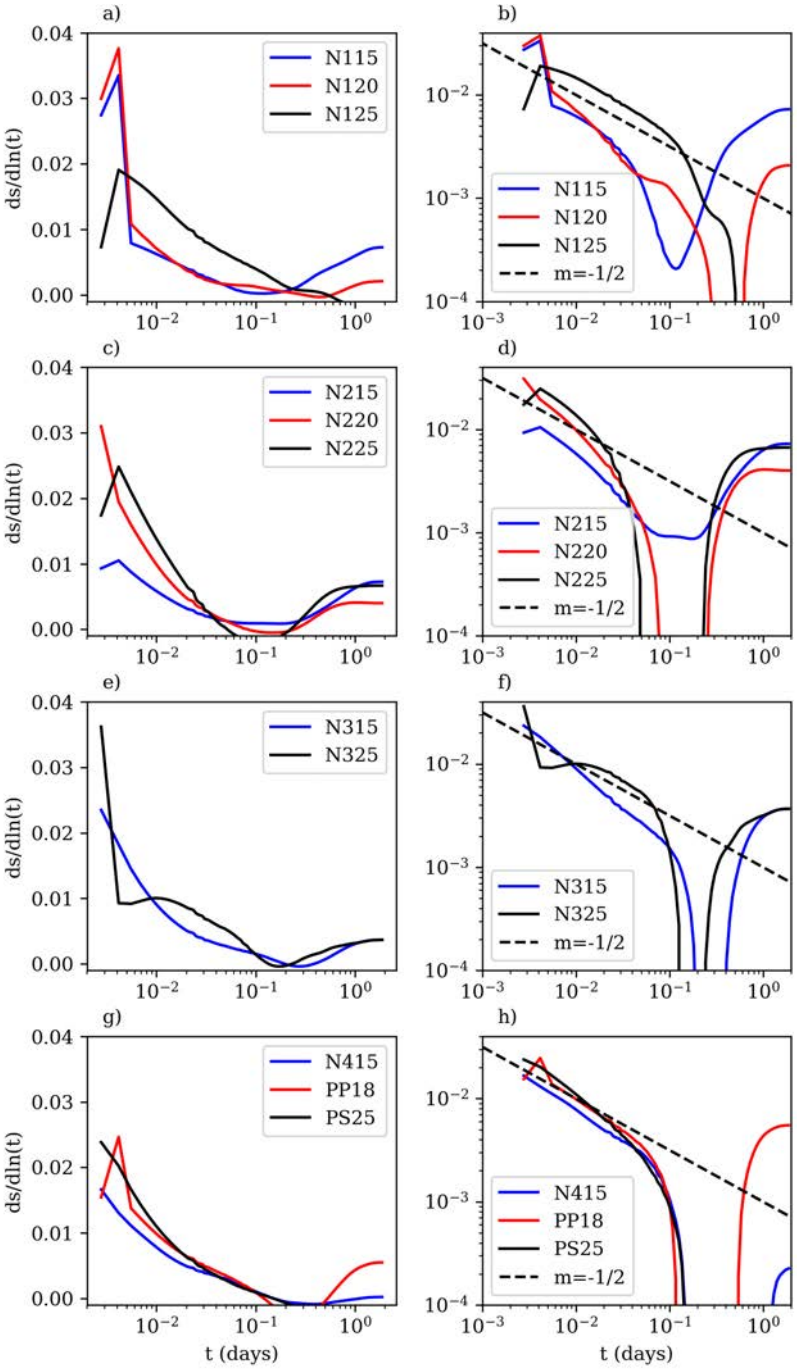

Figure 3.6: Diagnostic plots showing semi-log scale plots on the left and log-log plots on the right.

spherical flow period is consistent with the short screen interval of the pumping well, although the fact that it lasts 0.1 days suggests that leakage may have already started. The second flow period is characterized by the sharp drop in log-derivative, which we attribute to leakage through the silty layers from the top and bottom conductive layers. Finally, the log-derivative tends to stabilize in the third period, which indicates radial flow. That is, the pressure front is reaching the the full depth of the aquifer and all layers contribute flow to the pumping interval. Radial flow implies that the area where head is dropping grows with R^2, where R is the radius of influence, which grows with $\sqrt{t}$. The cone of depression does not need to be circular. It may be irregular, growing further along zones of high permeability (i.e., flow may not be radially symmetric).

We denote full radial conditions to the situations where all observation points drop at the same rate, meaning that they belong to the region where the cone of depression drops without changing its shape. If full radial conditions had been achieved, the final slope should have been the same for all points (Meier, Carrera, and Sánchez-Vila, 1998), which is not the case. The final slope of piezometers N115, N215, N225, N315, N325, and PP18 lies around 0.007 m, which implies a transmissivity ($T = Q/4\pi m$, with Q pumping flow rate and m log-derivative) of some $4000m^2/d$. N220 is close but not quite there, while the final log-derivative of N120, N125, N415 and PS25 is definitely smaller. Except for N220, all piezometers reaching the 0.007 log-derivative are either close to the pumping interval or belong to the same layer. This supports further our earlier conjecture that the silt layers act as aquitards that delay the response to pumping. This conceptual model is consistent with the information about the vertical heterogeneity shown in the gelogical records.

3.3.3 Estimation of hydraulic parameters

We interpret the drawdown curves using a simple numerical model so as to interpret all observation wells at once. The model facilitates the explicit representation of the vertical heterogeneity, screen intervals and well-bore effects.

A 2D radial vertical cross-sectional model was built with TRANSIN. The layers are a simplification of the lithological distribution (Figure 3.2). Layer 1 represents a buffer layer with a large storativity value designed to reproduce the yield from the phreatic surface and, possibly, delayed yield if the permeability of the layer is small (Carrera and Neuman, 1986). The well bore is a linear element of large permeability representing the borehole. The large permeability ensures that heads are the same for all borehole nodes. Flow from

Table 3.2: Hydraulic parameters resulting from manual calibration of the pumping test.

	K [m/d]	Ss [m-1]
L1	30	0.1
L2	0.1	0.00002
L3	29	0.00002
L4	0.28	0.00002
L5	127	0.00002
L6	2.7	0.00002
L7	441	0.00002
L8	0.016	0.00002
Wellbore	10000	0.5
Skin L5	231	0.00002
Skin L6	42	0.00002

the formation into the borehole is computed by the simulation code. Skin elements are located around the borehole and allow representing resistance to flow trough the borehole screened section, as well as construction effects.

The inverse problem was ran for all layers. The resulting hydraulic conductivities are shown in Table . The model could only be calibrated if layers L2, L4 and L6 display a moderately low hydraulic conductivity, thus acting as semi-confining layers. Notice that the L2 layer was not initially meant to represent an aquitard, but the top conductive layer. We conclude that the calibration reduces permeability of Layer 2 to represent the semi-confining effect of silty layers present at around -6 and -8 meters depth, and to delay the mobilization of storage from the water table (specific yield).

The high permeability layer (L7) appears on top of the low permeability weathered granites (L8). This high permeability was necessary to fit the drawdowns from deep boreholes. This high permeability probably reflects the coarse sand or even gravel deposit found at this depth (Martínez-Pérez et al., 2020).L3 and L5 represent sandy deposits located between semiconfined silty layers.

In summary, computed permeabilities are consistent with the geological information. In our view, this result demonstrates that much information is contained in the drawdown data, despite the noisy nature of the original measurements.

The numerical model reproduce measured drawdowns with surprising accuracy (Figure 3.7).The fact that this good fit is obtained with realistic hydraulic

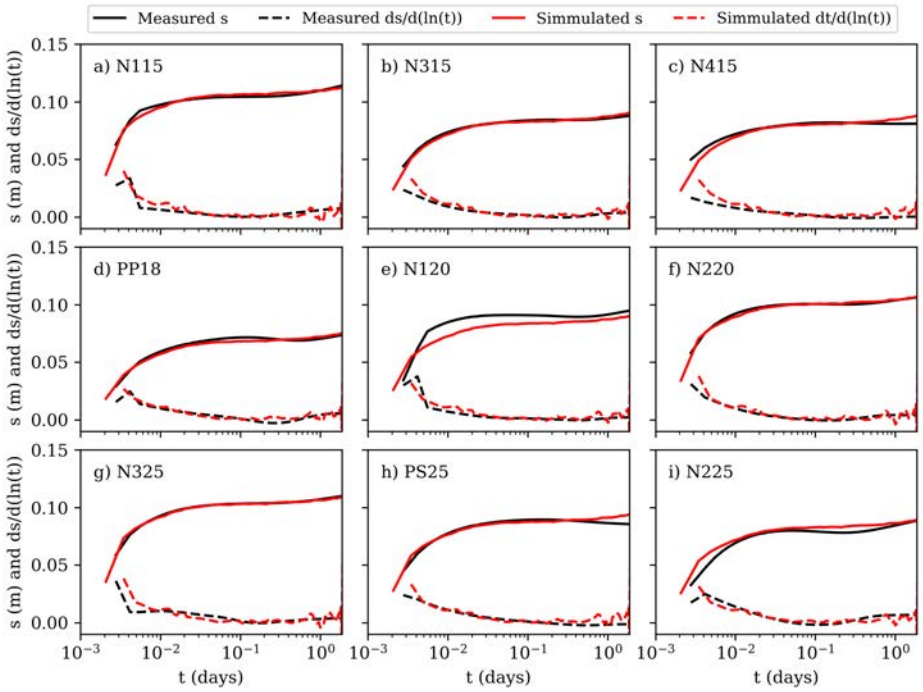

Figure 3.7: Comparison of model calculation (red) to filtered data (black) in terms of both drawdowns (full lines) and indicate drawdowns and log-derivatives (dashed lines).

parameters confirms that the conceptual model drawn from the diagnostic plots is a valid hypothesis. Moreover, it proves that the changes in slope of the drawdowns are not an artifact of the filtering process, but an effect of the aquifer geometry on the aquifer response to the pumping test.

3.4 Conclusions

Drawdowns resulting from the pumping test carried out in Argentona were obscured by environmental water-level fluctuations and signal noise. Initially, this situation prevented the interpretation of the experimental data. To overcome this impediment, we propose a step-wise approach for the processing and interpretation of complex drawdown results from pumping tests, which is especially recommended for coastal aquifers were multiple environmental influences

on water heads converge.

The proposed approach consist on six steps:(1)Identification of contributing components to natural head fluctuations, such as tides, recharge or storm surges. (2) Application of a multiple linear regression with optimized time lags for each observation well during the period unaffected by pumping (this requires a long observation period both before and after the pumping test). The resulting regression is used for reconstructing natural heads during the pumping and recovery period. (3) Defining two drawdown curves for each piezometer (one with directly measured drawdowns during pumping, and another one with drawdowns derived from measurements during recovery). (4) De-noising with the smooth log derivative method. (5) Qualitative interpretation of diagnostic plots. (6) Quantitative interpretation of drawdowns.

This approach has allowed us to derive trend-free and noise-free drawdowns. We test their validity by comparing the drawdown curve during pumping to that derived from recovery, for each piezometer.

An important addition of this approach is the validation of the drawdown during pumping test with recovery period data. This approach allowed us to validate the trend filtering process with independent data, adding more reliability to the results.

The possibility to analyse the drawdown separately from the rest of water-level components enable the construction of the diagnostic plots. These plots are useful to define the aquifer conceptual model. Based on the diagnostic plots we could distinguish three flow regimes: (1) spherical flow during the initial period, which reflects that pumping was done from a short screen piezometer; followed by (2) a leakage period, which reflects flow across the silt layers bounding the pumped layer; and (3) a late time 2D radial flow regime, which reflects the lateral growth of the cone of depression. We had not anticipated these results, but they are consistent with the geology of the aquifer.

Additionally, the quantitative interpretation of the drawdonws allows for much more simple numerical models, or even the application of analytical solutions. In any case, the removal of processes in the data facilitates the generation of more robust interpretations.

Despite the interesting results achieve during this work, precautions may be taken when using this methodology. The method is highly sensitive to the selection of environmental water-level components. Probably, and initial trial-and-error analysis must be done in order to find the contributing components to the water level. Moreover, independent data on the environmental water-level fluctuations may not be available. In those cases, Halford et al. (2012) provides alternatives by generating synthetic time series of each environmental force acting on the groundwater level.

We believe this methodology, and its testing in a such a complex situation, could be of help and inspiration to all practitioners confronting a similar task. The results prove that the method works, providing useful and robust results. Further research could be concentrated in the application of more advanced statistical methods, like artificial neural networks, to improve the water-level model.

Chapter 4

Heat Dissipation Test with Fiber-Optic Distributed Temperature Sensing to estimate Groundwater flux [1]

In this chapter we propose a method to measure groundwater flux and thermal parameters around a borehole from the interpretation of heat dissipation tests performed by heating the armour of an Optical Fibre cable installed outside the well casing. We show that the resulting temperature build-up goes through four periods easy to identify using the log derivative of temperature (dT/dlnt): initial response, skin (cable insulation), conduction dominated and advection dominated. The method is similar to thermal resistance tests, but benefitting from the high spatial and temporal resolution of Distributed Temperature Sensing (DTS) and lasting longer, so as to measure advective dissipation. Field installation relies on an innovative way to install the FO cable in the annular space of the well, close to the aquifer matrix. We test the proposed method in an unconsolidated shallow aquifer with controlled pumping. Results are in agreement with independent estimates of groundwater velocity.

[1] This chapter is an edited version of: Laura del Val, Jesús Carrera, María Pool, Lurdes Martínez, Carlos Casanovas, Olivier Bour, Albert Folch. Heat Dissipation Test with Fiber-Optic Distributed Temperature Sensing to estimate Groundwater flux. Water Resources Research. (2020). (under review)

4.1 Introduction

Quantification of groundwater velocity would be desirable for numerous hydrogeological problems, ranging from contaminant migration to submarine groundwater discharge quantification, and from geothermal systems optimization to leakage identification. Unfortunately, no practical method is available for direct measurement of natural groundwater velocity in aquifers. The most reliable estimates of natural flux can be obtained through solute and/or heat tracing (Davis et al., 1985; Anderson, 2005; Reiter, 2001; Taniguchi, 1993; Bakker et al., 2015; Tombe et al., 2019). However, natural flow tracing is expensive (several observation wells are needed and the test may last long), risky (the observation network may fail to get the plume), often hard to interpret and, as a result, rarely repeated over time for characterizing time variability. What would be desirable is a single well method to measure natural groundwater flux in the way one measures transmissivity or head.

These conditions are apparently met by heat and solute dilution methods, which relate the flow rate to the observed variations of a known initial tracer concentration or heat pulse placed within the well. These tests have been widely used, and therefore validated (Drost et al. (1968), Jamin et al. (2015), and Pitrak, Mares, and Kobr (2007) among others). Arguably, the most sophisticated of these are fluid logging methods (Tsang, Hufschmied, and Hale, 1990), which consist of replacing the borehole fluid and measuring how some fluid property (e.g., electrical conductivity) evolves over time along the borehole. Variations of the method can be used to measure and quantify zones of increased groundwater inflow hydraulic fracture interconnectivity and to identify velocity within the borehole. These measurements are useful and can be used to derive aquifer properties, but they yield flow rates within the borehole, not the groundwater flux in the aquifer.

The high spatial and temporal resolutions of Fiber Optic Distributed Temperature Sensing (FO-DTS) techniques have opened the way for improved thermal tracing. This is especially true for active FO-DTS, which consists of heating the FO cable or the media around the monitoring cable, and monitoring the ensuing temperature increase (Freifeld et al., 2008). Active FO-DTS have been employed as a thermal resistance test (Freifeld et al., 2008), as a fluid logging technique (Banks, Shanafield, and Cook, 2014) and for heat tracing (Bakker et al., 2015; Hausner et al., 2016). However, the best way to employ this technology is still under discussion due to the different issues raised during: (i) interpretation of results, (ii) correction of FO cable thermal effects and (iii) installation of the cable.

The installation of FO in the borehole remains an open question. Several

configurations have been proposed. For active FO-DTS, some authors installed separate heating and monitoring lines (Bakker et al., 2015; Banks, Shanafield, and Cook, 2014; Hausner et al., 2016; Liu, Knobbe, and Butler, 2013; Selker and Selker, 2018; Tombe et al., 2019). A few authors simplified the installation by using the same cable for heating and monitoring (Coleman et al., 2015; Perzlmaier et al., 2004; Read et al., 2014; Su et al., 2016). In parallel, the same studies proposed different approaches for the installation of the cable in the ground. Initial studies deployed the cable within the well (Coleman et al., 2015; Hausner et al., 2016; Klepikova et al., 2011; Liu, Knobbe, and Butler, 2013), which is the most simple and non-permanent field strategy. However, velocity within the well might be affected by natural convection. Coleman et al. (2015) used a lining filled with water to hinder convection. Likewise, Selker and Selker (2018) permanently filled the borehole in order to prevent any effect of free water movement. A different approach is proposed by Banks, Shanafield, and Cook (2014) and Tombe et al. (2019) by installing the cables with direct push equipment leaving the aquifer materials to collapse around the cable. Heating curves produced by this method are the most representative from aquifer conditions. However, this installation has two main limitations: a depth limit of around 60 meters and impossibility for installation in certain geologies like gravels. Therefore, proper installation of FO remains an open question.

Beyond this discussion, the question of how to measure natural aquifer flux remains unanswered. Perzlmaier et al. (2006) and Perzlmaier et al. (2004) proposed a semi-empirical solution to estimate dam leakage by combining the steady state solution of a cylindrical heat exchanger, with the estimation of empirical factors. Su et al. (2016) used a numerical approach to investigate the relationship between effective thermal conductivity and seepage velocity through an experimental sand tank. Selker and Selker (2018) proposed heating at spaced intervals to measure both radial heat dissipation and vertical fluxes. However, by setting the cable in the middle of the well, they could hardly observe advection. In summary, formal analytical methods for estimating absolute groundwater fluxes using a single heating and monitoring cable have not been established yet.

In order to overcome the above-mentioned limitations we propose a new approach for the quantification of groundwater velocity and the thermal properties of the aquifer. Alternatively, to other methodologies, we propose to install the FO cable in the annular space between the well and the aquifer. The installation of the cable outside the well casing aims to: 1) benefit from the borehole installation process, 2) keeping the cable as closer as possible to the aquifer materials and 3) maintaining the borehole available for the installation

of additional monitoring devises. In addition, we use an analytical solution to interpret the heating curves resulting from the active FO-DTS. The interpretation methodology pays special emphasis to the estimation of the cable thermal effects in the heating curves. This methodology allows the interpretation of the heating curves generated at a single heating and monitoring cable, which simplifies field installation in many circumstances apart from those tested in this case. The presented method has been tested under controlled velocity conditions in a real sandy aquifer.

4.2 Problem statement and solution

We discuss the conceptualization and solution of the problem. We start with a simplified ideal set-up: a line heat source in a homogeneous medium with horizontal flux (Figure 4.1a). Second, we discuss and consider in the analytical solution the effect of the cable materials (Figure 4.1b) to account for storage and skin effects, much like in well hydraulics. Finally, the proposed set-up involves the installation of the FO cable in the annular space of the piezometer. So, we solve the problem considering the field setup in which we have two parallel cables (Figure 4.1c), the one going down to the piezometer bottom and the same cable coming up to the surface with an unknown orientation with respect to the groundwater flow (Figure 4.1d).

4.2.1 Analytical solution for the ideal case

The problem can be idealized as the temperature rise created by a small diameter heated cable embedded in a porous media where groundwater is flowing, which is governed by:

$$\frac{\partial T}{\partial t} = \nabla((\lambda \mathbf{I} + C_w \mathbf{D_p}) \cdot \nabla T) - C_w \mathbf{q} \cdot \nabla T + P\delta(\mathbf{x}) \tag{4.1}$$

where T $[K]$ is the temperature, Cw $[J/m^3K]$ is the water heat capacity, $\mathbf{D_t}$ $[m^2/T]$ is the thermal dispersion tensor expressed as $\mathbf{D_T} = \lambda \mathbf{I} + C_w \mathbf{D_p}$, where λ $[J/mK]$ is the thermal conductivity, $\mathbf{I}$ is the identity tensor, $\mathbf{q}$ $[m/s]$ is the specific discharge and P$[W/m]$ is the power released per unit length of cable. We take the x-axis along the flux direction perpendicularly to the cable. Therefore, $\mathbf{q} = (q_x, 0)$ and $\mathbf{D_T}$ is a diagonal tensor with principal components $D_{TL} = \lambda + C_w \alpha_{TL} q_x$, $D_{TT} = \lambda + C_w \alpha_{TT} q_x$, where α_{TL} and α_{TT} are, respectively, the longitudinal and transverse thermal dispersivities, much smaller than their solute transport counterparts. The solution to this problem

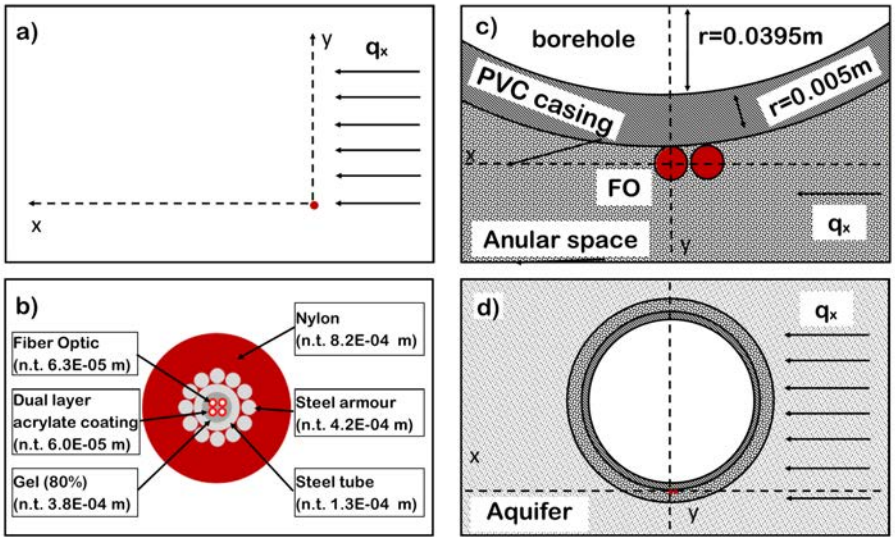

Figure 4.1: Description of the problem: a) Idealized setting (Infinite Moving Line Source), b) detailed cross-section of Optical Fiber cable (n.t. = nominal thickness) (source: personal communication Brugg Kabel AG (Switzerland)). c) schematic cross-section of optical fibre cable installation in the annular space. d) Zoom out schematic horizontal cross-section of the field installation with indication of groundwater flux.

for the purely conductive problem was presented by Carslaw and Jaeger (1959) (Stauffer et al., 2014).

The full solution for the dispersive problem is derived in the AppendixB. Actually, accounting for dispersion is somewhat controversial. Dispersion is often neglected (see discussion by Stauffer et al. (2014). Here, following the findings of Hidalgo, Carrera, and Dentz (2009): we use dispersion only to obtain the spatial distribution of temperature downstream, but neglect it to obtain temperature build-up at the source. That is, near the source, $\mathbf{D_T} = \lambda \mathbf{I}$, which allows simplifying the solution Equation 4.1 to

$$T(x, y, t) = \frac{P}{4\pi\lambda} e^{\frac{q_x C_w x}{2\lambda}} W_H(u, v) \tag{4.2a}$$

$$u = \frac{C_b r^2}{4\lambda t} \tag{4.2b}$$

$$v = \frac{q_x C_w r}{2\lambda} \tag{4.2c}$$

where r is the distance from the heating source, Cb $[J/m^3K]$ is the bulk heat capacity, and W_H is the Hantush Well function (Hantush and Jacob, 1955) (Equation B.6).

We have evaluated using the approximation of Shirahata et al. (2016), who also discuss the asymptotic behavior of for small (i.e., long time, advection dominated heat transport) and (i.e., small or , conduction dominated transport). These two asymptotic behaviors, which can be observed in Figure 4.2a, are of interest. For small times and distances, advection can be neglected, and Equation 4.2 can be approximated as Theis (1935) well function, evaluated at the radius of the heated cable. Note that is the time it takes for heat generated at to reach . In reality, the opposite might be a closer approximations (heat is generated on the armour and the FO sensor is in the center). We will return to this issue in Section 4.3. Theis solution is usually approximated as Cooper and Jacob (1946).

$$T(x, y, t) = \frac{P}{4\pi\lambda} \ln \frac{2.25\lambda t}{C_b r^2} \tag{4.3}$$

Equation 4.3 plots as a straight line versus log-time. The slope of this line (K/log10 cycle) and the intercept with the log-t axis, t_0, can be used to derive λ and C_b as (Cooper and Jacob, 1946)

$$\lambda = \frac{\ln 10 P}{4\pi m} = 0.183 \frac{P}{m} \tag{4.4a}$$

$$C_b = \frac{2.25\lambda t_0}{r^2} \tag{4.4b}$$

The distance affected by the temperature propagation due to conduction (R_{inf}) is:

$$R_{inf} = \sqrt{\frac{2.5\lambda t}{C_b}} \tag{4.5}$$

Heat within this radius of influence is dragged by the groundwater flux. In fact, Equation 4.3 can be viewed as an expression of the competition between conduction, which tends to increase temperature and R_{inf}, and advection, which drags heat away. Eventually, advection dominates heat transport (i.e., R_{inf} grows large enough for all the heat at the source to be dragged away),

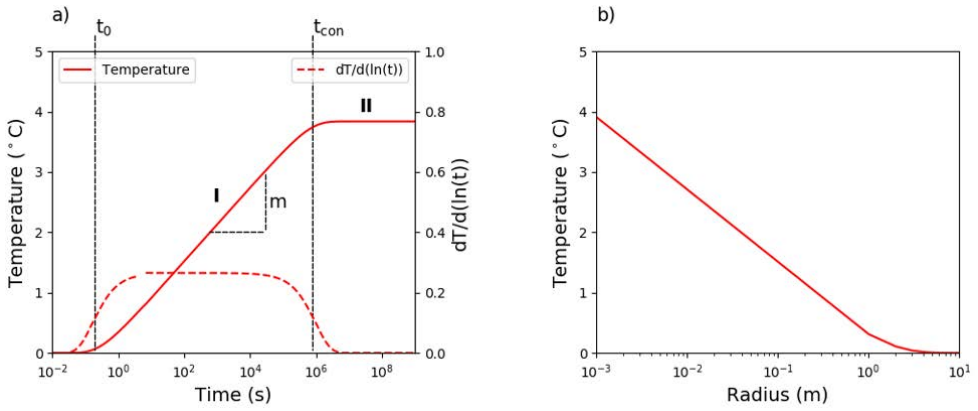

Figure 4.2: Behaviour of analytical solution for an ideal case: a) semi-log plot of temperature increase and its log-derivative (Equation 4.2). I and II indicate the conduction-dominated and advection-dominated phases respectively. b) Spatial distribution of temperature once steady state is reached. (data: λ_b=3 $Wm^{-1}K^{-1}$; C_w=4.2e^6 $Jm^{-3}K^{-1}$; C_b=2.2e^6 $Jm^{-3}K^{-1}$; r=0.001m, P=10 Wm^{-1}; q_x=1.1e^{-6} ms^{-1})

so that R_{inf} does not grow anymore and steady state is reached (i.e, temperature is stabilized). This is represented in Equation 4.2a by the "Advection-dominated" phase, which can be easily identified when the log-derivative tends to cero. Under these circumstances, the well function can be approximated as the Bessel function of second kind and order cero (K_0). Considering x=0, the Equation 4.3 can be approximated as:

$$T(r, t = \text{inf}) = \frac{P}{2\pi\lambda} K_0(\frac{C_w q_x}{2\lambda} r) \tag{4.6}$$

Equation 4.6 represents the maximum temperature reached during heating, which depends on the specific discharge.

In summary, Equation 4.2 evaluated at the radius of the heating cable, behaves as Theis well function at early times, which can be approximated as a straight line after in semi-log plot (Equation 4.3) and tends to stabilize to a constant value, given by Equation 4.6, at late times. This behaviour is illustrated in Figure 4.3 for several values of specific flux and typical values of thermal conductivity and capacity. Figure 4.3a, the larger the groundwater flux the lower maximum temperature reached by the heating curve and the longer the time it takes to reach this value. Figure 4.3b shows the maximum

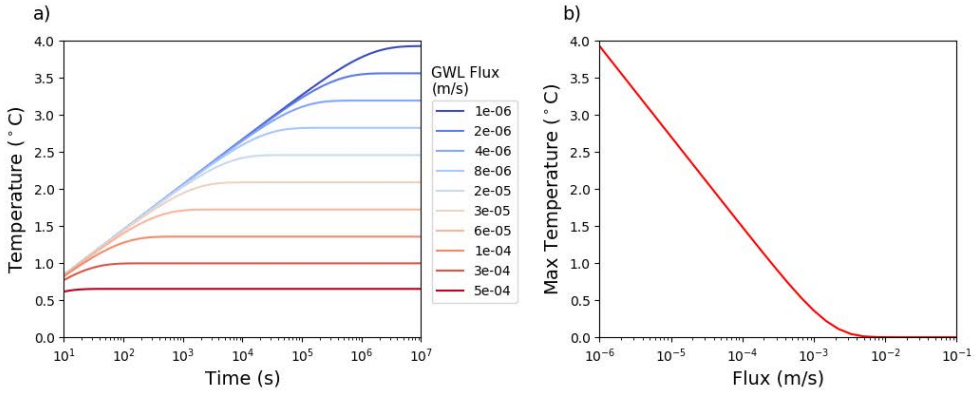

Figure 4.3: Sensitivity of the analytical solution to groundwater velocity: a) Temperature evolution in time under different specific discharge rates. b) Maximum temperature reach for a wide range of fluxes. (data: λ_b=3 $Wm^{-1}K^{-1}$; C_w=4.2e^6 $Jm^{-3}K^{-1}$; C_b=2.2e^6 $Jm^{-3}K^{-1}$; r=0.001m, P=10 Wm^{-1})

temperature as a function groundwater fluxes, giving an indication of the application range of the method for a given set of thermal properties of the media, power injection and cable radius.

We term conduction characteristic time (t_{con}) to the time when the conduction dominated and advection dominated behaviours intersect. It results from combining Equation 4.3, and it is given by:

$$t_{con} = \frac{2.24\lambda C_b}{C_w^2 q_x^2} \tag{4.7}$$

t_{con} can be identified from the heating curve at the point where Equation 4.3 and 4.6, thus conduction-dominated and advection-dominated phases, cross over. Knowing t_{con} and , 4.7 can be used to estimate groundwater velocity (q_x).

4.2.2 Adaptation of analytical approach to a real case: "Skin effect"

The simple conceptual model explained above (Figure 4.4a) do not consider the thermal effects induced by the cable materials through which heat has to travel before reaching the aquifer (Figure 4.4b). In reality, the obtained experimental heating curve is the combination of conduction heating transport within the cable, and an advection-conduction transport in the porous media once the

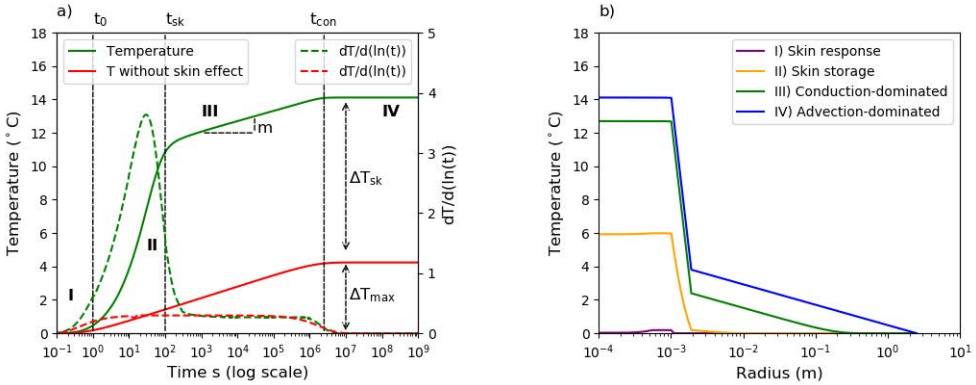

Figure 4.4: Behaviour of temperature increase and its log-derivative when skin effect is present: a) The heating curve with skin effect is compared with that resulting from applying the approximation from Srivastava and Guzman-Guzman (1998) to equation (2). Evolution of temperature with skin effect considering all cable material from a heat transport model (data: λ_w= $5.8e^{-1}$ $Wm^{-1}K^{-1}$,λ_b= 3 $Wm^{-1}K^{-1}$; $\lambda_{poliamida}$= $9e^{-2}$ $Wm^{-1}K^{-1}$; λ_{steel}= 16 $Wm^{-1}K^{-1}$; λ_{gel}= 0.3 $Wm^{-1}K^{-1}$; C_w= $4.2e^6$ $Jm^{-3}K^{-1}$; C_b= $2.2e^6$ $Jm^{-3}K^{-1}$; $C_{poliamida}$= $6.4e^6$ $Jm^{-3}K^{-1}$; C_{steel}= $3.8e^6$ $Jm^{-3}K^{-1}$; C_{gel}= $2e^6$ $Jm^{-3}K^{-1}$; P=$10Wm^{-1}$; $q_x = 1.1e^{-6}ms^{-1}$). The four heat transport regimes are indicated in the figure: I) skin response, II) skin storage, III) conduction dominated and IV) advection dominated. b) Spatial distribution of temperature at representative times for each heat transport regime.

heat reaches the cable walls. This effect is analogue to the "skin effect" in well hydraulics (Feng and Zhan, 2016) or the "borehole thermal resistance" in geothermal thermal response tests (TRT) (Bandos et al., 2011; Raymond et al., 2011; Wagner et al., 2013). In TRTs thermal influence of the well structure is taken into account explicitly as a factor (mKW^{-1}) which corrects for the excess of temperature increase due to the temperature storage in the borehole materials. Likewise, in well hydraulic the skin effect may increase or decrease drawdown at the pumping well because permeability around the well casing may be larger or smaller, respectively, than the formation permeability, which causes uncertainty in the estimation of storativity. Therefore, for interpreting heating curves obtained at the heated cable it is necessary to acknowledge this effect.

In this study, we define the "skin effect" (ΔT_{sk}) as the temperature increase due to low thermal conductivity between the source of energy and the geological media surrounding the cable. This effect includes the low thermal conductivity

of the isolation materials around the heating source. It also comprises any thermal interference of the installation around the cable (i.e. borehole), which could reduce heat dissipation towards the geological media (see Figure 4.1c). The skin effect can be expressed as an excess of temperature:

$$T_m = T(0, r, t) + \Delta T_{sk} \tag{4.8}$$

where T_m is the temperature at the measurement point, edge of the heating system, at a distance r from the centre of the cable, where measures are taken. $T(0, r, t)$ is the temperature calculated with Equation 4.2, thus the temperature without skin effect.

The skin effect due to the cable itself, depends on the thermal properties of the FO cable material. The glass fibres are protected with different layers for specific purposes. For the single steel armoured Multi Mode fibre optic cable (*Brugg Kabel AG, Switzerland*) used in this study, the glass fibres are first covered with a dual layer acrylate coating, then embedded in a steel tube filled with a gel, then a steel armour and finally a nylon coating (Figure 4.1b). Due to its low thermal conductivity, the nylon coating is expected to produce the strongest contribution to the skin effect.

Exact estimation of the cable skin effect is not possible, since thermal properties of the cable materials are not provided by the manufacturer. However, if theoretical values and radius of each cable layer are considered in a heat transport model, the resulting heating curve would present an increase of temperature in the initial times which corresponds with the skin effect. Figure 4.4a shows the difference between the temperature evolution in time with (red line) and without skin effect (green line). As a result, the initial conceptual model expands from two regimes to four regimes: (I) During the first seconds of heating, the gel surrounding the fibre delays in the response to the injected energy. This is the "FO response" regime. (II) The second regime presents a stable heating rate, representing the heat conduction through the cable materials. This phase may be named "skin dominated". (III) In a third stage, the cable is warm enough to transfer heat to the aquifer media. This sustained slope represents the heating rate, or "Conduction-dominated" regime. (IV) Finally, the last stage occurs when temperature diffusion in the media reaches a limit due to advection, thus "advection-dominated" regime.

Ultimately, proper estimation of the groundwater velocity needs to be carried out once the skin effect is subtracted from the data. Skin effect can be roughly estimated graphically, with the difference between the heating curve and the curve without skin effect, thus the approximation for small times (Equation 4.3). Therefore, the analytical approach for the interpretation of

the heating curves described in the previous section must be expanded with an additional step: (1) The slope of the conduction-dominated phase can be obtained graphically from the log derivative ($dT/dlnt$), when this is constant but different from zero. The thermal conductivity of the porous media is then calculated with Equation 4.4a. (2) The skin effect can be subtracted knowing the initial time (t_0 in Figure 4.4a. This effective skin effect, results from the joined effect of the cable materials and any other material around the cable that might store heat. (3) From the initial time and using Equation 4.4b the bulk volumetric heat capacity can be estimated. (4) Finally, The conduction characteristic time (t_{con} in Figure 4.4a) can be graphically estimated from the intersection between the conduction-dominated and advection-dominated phases. Characteristic conduction time and previously estimated thermal conductivity are used to calculate the groundwater velocity from Equation 4.7.

4.2.3 Adaptation of analytical approach to a real case: two parallel heaters

An additional deviation from the ideal case is the contribution of a second heater in parallel to the initial one to the temperature increment. This can be solved by superposition of the temperature increase due to each heating source, where a heater would be located in (x_1, y_1) and a second one in (x_2, y_2).

$$T_{(x,y,t)} = T_{1(x-x_1,y-y_1,t)} + T_{2(x-x_2,y-y_2,t)} \tag{4.9}$$

For the first heating source we consider r_1 equal to the radius of the heater. For the second heater, r_2 is the distance between the observation point (the centre of the first heater) and the centre of the second heater. Both heaters are considered to be located right next to each other (Figure 4.1c).

Figure 4.5 illustrates the difference between the analytical solution for an ideal case with one single heating source (Figure 4.5c), with the case of two parallel heating sources located at x_2 equal to zero (Figure 4.5d) and larger or smaller than zero (Figure 4.5e). In Figure 4.5a, it can be observed how temperature increment is doubled when a second heater is added close to the initial one. The effect of the position in x of the second heater is illustrated in Figure 4.5b by calculating the temperature for x_2 ranging between ± 100 times r_2. In reality, this effect can be neglected if both cables are assumed to be right next to each other, thus x_2 ranging between ± 2 times r_2.

Based on the mentioned conceptual model there are two parameters in our methodology that should be adapted to account for the contribution of a second heating cable, the input power and the distance between cables. As both

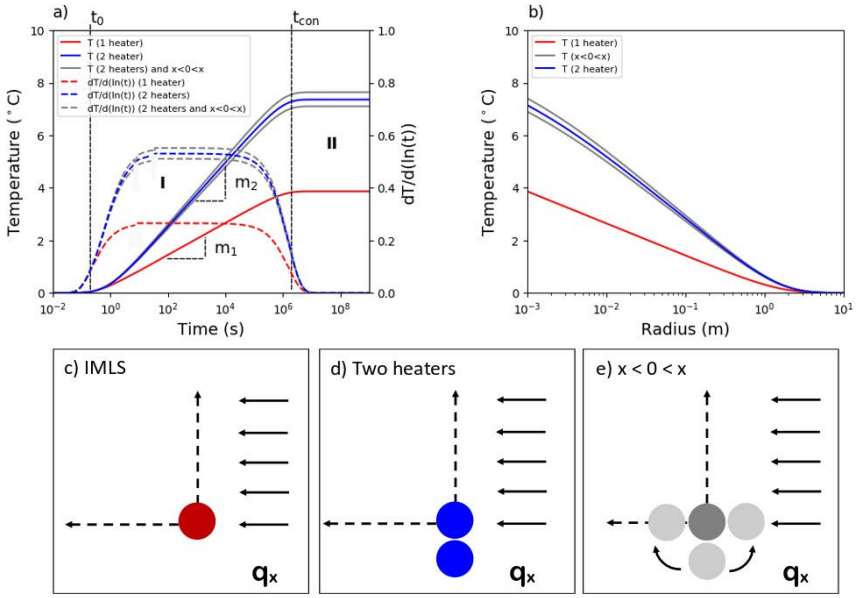

Figure 4.5: Conceptual model ranging from the ideal case to more complex scenarios where two cables are heated in parallel. a) Comparison of the transient solution for the ideal case, thus with only one heater (red), for two heaters (blue) , and for two heaters where the second could be in different position with respect to the direction of q_x and the observation point, thus x is different from zero (grey). "m1" represents the slope of the ideal case, while "m2" represents the slope of the case with two parallel heaters. b) Stationary spatial distribution of temperature from the heater towards the aquifer matrix. c) Graphical representation of the conceptual model for an Infinitesimal Moving Line Source (IMLS). d) Graphical representation of the conceptual model for two parallel heat line sources. e) Graphical representation of the conceptual model for two parallel heat line sources, where the position in x of the second heater is different from zero. (data: λ_b=3 $Wm^{-1}K^{-1}$; C_w=4.2e^6 $Jm^{-3}K^{-1}$; C_b=2.2e^6 $Jm^{-3}K^{-1}$; r=0.001m, P=10 Wm^{-1}, $q_x = 1.1e^{-6}$ ms^-1)

cables are considered to be next to each other, the input power is considered to be doubled when estimating from Equation 4.4a. For the estimation of q_x, Equation 4.6 and Equation 4.9 are combined to account for the temperature increase due to the second heater. In this case, r_1 and r_2 are the distances of each heater to the observation point (located in the centre of the fibre optic

cable) respectively. Additionally, the effect of the second heater position (x_2) can be taken into consideration by not neglecting the exponential term in Equation 4.2 when approximating Equation 4.6. In this case, Equation 4.6 is resolved for $x_1 = 0$ and x_2 between 0 and r_2, where r_2 can be optimized within this range.

4.3 Application to a real case: field set-up

The proposed approach for heat dissipation tests with FO-DTS at field scale was tested at the experimental site of MEDISTRAES, described in detail by Folch et al. (2020) (in press) and Martínez-Pérez et al. (2020) (submitted). The experimental site is located in the alluvial aquifer of the Riera Argentona 40 Km North from the city of Barcelona (Spain), between Catalan Littoral Mountain Range and Mediterranean Sea. Surface runoff only occurs during extreme rainfall events, therefore the "riera" or ephemeral stream runs dry most of the time. The catchment is dominated by granites and Paleozoic materials covered by Quaternary alluvial sediments. The field site is therefore situated in the Quaternary deposits formed by a sequence of alternating horizontal layers of coarse (gravels and sands) to fine (silt and clay) deposits. The result is a strong vertical heterogeneity, which generates multiple aquifer levels separated by a few decimetre thick silt layers, whose confining effect is still under discussion. The bottom depth of these Quaternary units is controlled by Paleozoic basement, having an average thickness close to the coast of 25 to 30 m (Agencia Catalana de L'Aigua, 2009).

The site comprises sixteen shallow piezometers installed between 30 and 100 m from the seashore, with depths ranging between 15 and 25 meters (Figure 4.6). Most PVC piezometers are screened only two meters. Single steel armoured Multi Mode fibre optic cable (*Brugg Kabel AG, Switzerland*) was installed along the annular space of the piezometers (Folch et al., 2020) (in press). The cable was installed in a "U" shape, so that both cable extremes came out of the well (Figure 4.7). The cables were then connected in series in order to form two single fibre optic lines that can be deployed individually. The connections were done with a *Prolite-40 Fusion Splicer* (*PROMAX, Spain*) and an *EFC-22* fibre optic cutter (*Ericson, Sweden*). Each cable line has a length around 950 m with eight connections in each. The cable was deployed with an Oryx + (*Sensornet, UK*) Distributed Temperature Sensor (DTS). The sensor has a minimum spatial sampling distance of 0.5 m and a minimum acquisition time of 10 seconds. For the purpose of this experiment, we chose a 10 seconds integration time, with a sampling frequency of 20 s, which then was increased to 30 s integration time and 2 min acquisition time after 4 hours. FO lines were

connected in a duplexed configuration (Hausner et al., 2011), and deployed in both directions , forward and reversed. Two calibration baths with different temperatures were installed at the beginning of the cable in order to inverse the DTS raw signal into temperatures (Figure 4.7). Both baths are homogenised with small pumps (*EHEIM Compact 300, EHEIM, Germany*), and monitored with *RBRsolo-T* high resolution temperature loggers (*RBR, Canada*). The warm bath was constructed by submerging at least 10 meters of cable in a 57 l portable coolers (*Igloo, USA*) filled of water kept with a 150W heater (*Sera, Germany*) at an average temperature of 38 °C. The cold bath was constructed with additional 10 m of cable submerged in a 40 l thermoelectric portable cooler (*MOBICOOL International Ltd, Hong Kong*) filled with water kept at an average temperature of 10 °C. DTS raw data are calibrated with the Single Ended Method (Hausner et al., 2011).

DTS raw data are transformed into temperature values using the Single Ended Calibration method. As proposed by Hausner et al. (2011), the quality of the calibration is reported through the Root Mean Square Error (RMSE) and Duplexing Error (Edup). The first is calculated using the difference between calibrated and known temperatures at the calibration baths, representing the accuracy of the calibration. The second is calculated as the average of the difference between the duplexed calibrated temperatures, bringing information about the calibration consistency along the cable. During the first 4 hours of the heat dissipation test, time integration period was set to 10 s. During this first period, the RMSE is 0.28 °C and the Edup is 0.08 °C. After 4 hours since heating started, the time integration period was set to 30s, bringing the RMSE and the Edup to 0.12 °C and 0.09 °C, respectively. For medium size cable lengths like this one, the selected time integration is the main limiting factor to temperature resolution. The initial seconds of the heat dissipation are crucial for the quantification of the skin effect. Therefore, the shortest integration period was chosen for the initial part of the heating dissipation test despite worsening of the temperature resolution.

4.4 Heat Dissipation Test

The Heat Dissipation Test implies heating a conducting element within the saturated soil until its temperature increase reaches steady state, while monitoring the temperature development of the heating element during heating and cooling phases. The FO cable used in this installation has a steel armour to provide strength. This armour can be used to heat the cable due to the resistance to electric conduction that the metallic armour provides. A variable transformer (*Carroll & Meynell, UK*) was used to provide constant electric

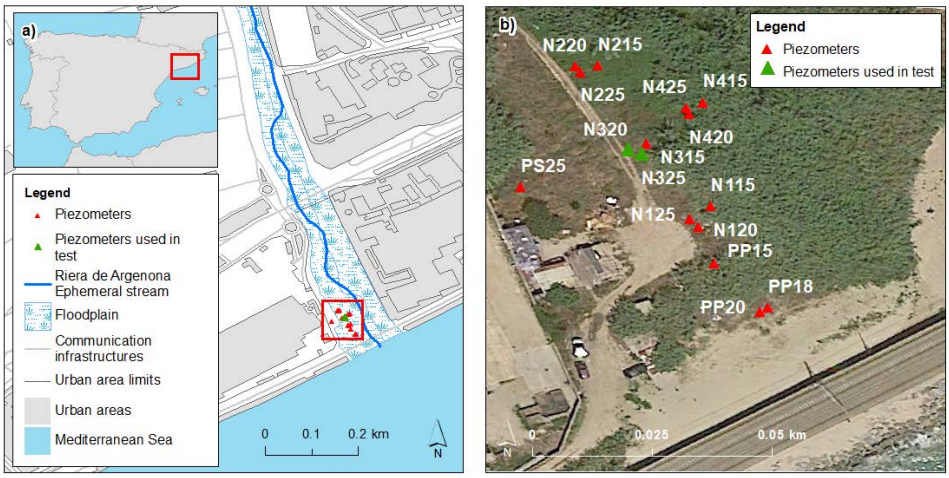

Figure 4.6: Location map: a) Location experimental site; c) distribution of piezometers in the field (sources: Institut Cartogràfic i Geològic de Catalunya (ICGC) and Agencia Catalana del Agua (ACA))

power of 1 W/m to the cable. The variable transformer was connected to the two either sides from the FO cable sticking out of the well installation. Electricity injection was monitored with a multi-meter.

In order to test the method, the heat dissipation test was performed under known radial velocity conditions. Thus, while a constant-rate pumping test was being carried out in the installation, a suction pump was installed in piezometer N320 (Figure 4.6), pumping at a constant flow rate of 4 l/s during two days. Pumping rates were monitored with an electromagnetic velocity meter and kept constant during the test. During pumping and recovery, water levels were monitored in all piezometers using pressure sensors (*LevelSCOUT 10m, Seametrics, USA*) programmed at a frequency of 2 min. The groundwater flux during steady state was estimated to be 5e-5 m/s, by assuming uniform radial flux across a cylinder with height equal to the thickness of the unit between the two closest sit layers, and assuming they are fully confining (5 m) and radius equal the distance between the pumping well and the observation well (N225), which is 2.5 m (Figure 4.7).

Once the drawdown reached steady state, we started to heat the FO cable of the N225 piezometer. Heating at the N325 lasted for 1.5 days, enough to reach the steady-state of the heating curve at the depth confronting the screened section of the pumping well (N320).

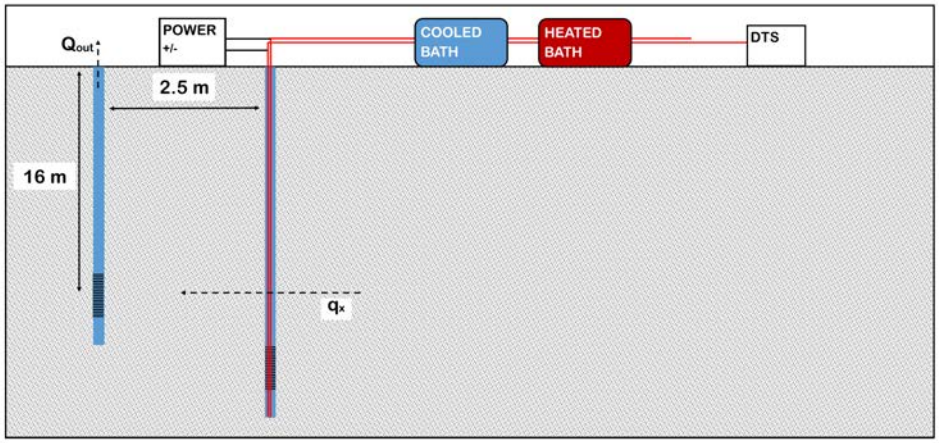

Figure 4.7: Schematic vertical cross-section of heat dissipation test field set-up.

4.5 Results

The test resulted in a set of heating curves vertically distributed along the observation well. Since the cable was installed in a "U" shape and the acquisition configuration ("duplexed") allowed for forwards and reversed data, four heating curves are available per monitoring location. The average maximum temperature increase reached at each depth is plotted in Figure 4.8a. Lowest temperatures indicate the areas with the higher groundwater fluxes. In fact, the lowest maximum temperatures occur at the depth confronting the screened interval of the pumping well (15 – 17 m). These are the only ones reaching steady state (Figure 4.8b), and thus, the only heating curves that can be interpreted with the proposed method.

Prior to any interpretation, the external trends and noise, distorting the signal, need to be removed. The first process is called de-trending and it was not necessary in this case because the daily temperature fluctuations do not penetrate deep enough to reach the selected depths. The second post-processing task aims to remove the noise coming from the Distributed Temperature Sensor. In this case, a two-fold objective will be addressed with the application of the Stable Computation of Log-derivatives from Ramos et al. (2017) to remove noise from temperature signal and compute the log-derivative.

The log-derivatives in combination with drawdown data are used for the identification of hydrogeological conceptual models responsible for the levels

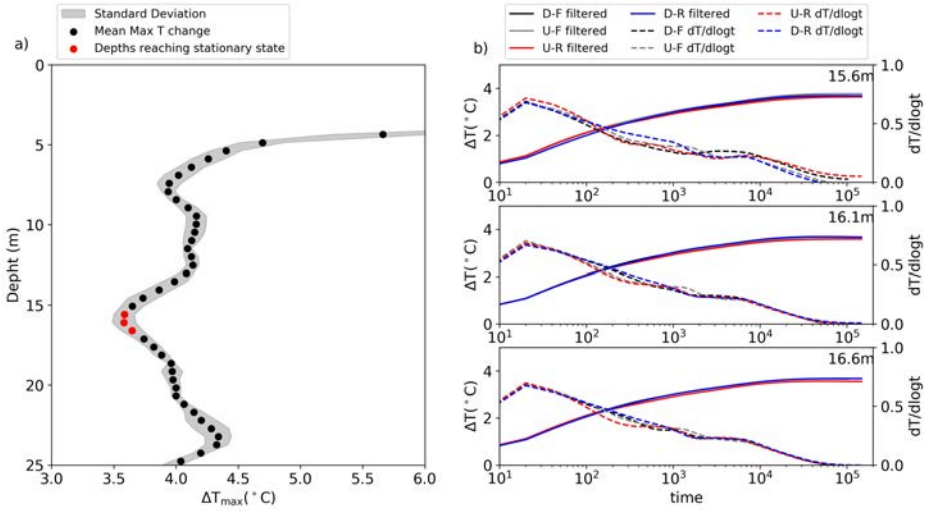

Figure 4.8: Results from the heat dissipation test: a) Vertical distribution of average maximum temperatures reach during the Heat Dissipation Test. Mean values are calculated with the four available heating curves at the same depth (cable going up and down and the forward and reversed signals for each). Curves at specific depths that reached steady state during the test are highlighted in red. b) Evolution of temperature change and corresponding log derivative for each of the three depths reaching steady state. These smooth curves are the result of applying the filtering method of the Stable Computation of Log-derivatives to the original data. The nomenclature used in the legend represents the downwards (D) and upwards (U) sections of the cable, and the forward (F) and reversed (R) back-scattered signals

response to the hydraulic test (Renard, Glenz, and Mejias, 2009) which are an analogy of the heat dissipation test for heat transport. The resulting log-derivative and smoothed data represented in Figure 4.9 for one of the selected depth, reveals the four phases of heating conceptual model described in previous sections, including the skin effect. The method is based on the analysis of the two last heating phases associated to the aquifer thermal properties and advection.

Firstly, the thermal conductivity is estimated. The log-derivative highlights two conduction phases with constant temperature increase attributed to the conduction within the cable materials ("Skin effect") and to the "conduction-dominated" phase in the aquifer matrix. The last is used to estimate the thermal conductivity of the media, which is 0.75 ±0.04 W/m °C (Equation 4.4a)

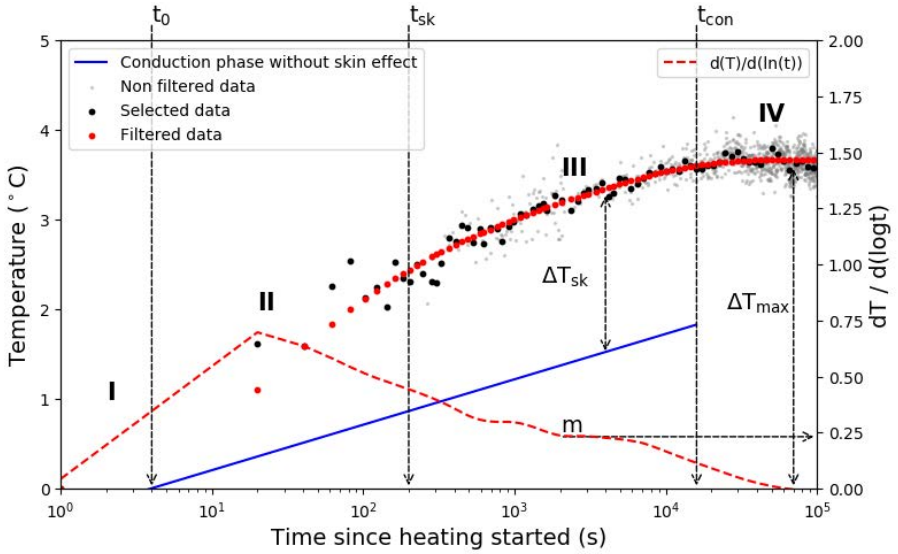

Figure 4.9: Heat dissipation curve at 16.1 m depth (black like in Figure 4.8a) in the observation well 2.5m away from pumping well. Grey dots represent the raw temperature data after calibration of DTS signal. Black dots are the logarithmic selection of 100 points necessary to apply the filter. Red dots represent the signal after application of Stable Computation of Log-derivative filter. Red dashed line represent the computed Log-derivative. Blue line represents the aquifer conduction phase without skin effect used to approximate graphically the skin effect. Number represent the heat transport regimens: I) skin response, II) skin storage, III) conduction dominated and IV) advection dominated. These regimes are delimited by the characteristic times: (t_0) initial time, (t_sk) skin time and (t_con) conduction characteristic time. Estimation of the thermal conductivity is based on the conduction-dominated phase slope (m).

(Figure 4.9).

The existence of a conduction phase associated to the heat storage in the cable materials, adds an additional temperature increase to the final temperature, the skin effect. The skin effect correction depends on the slope of the conduction-dominated phase and the initial time. However, as (Equation 4.4) is not known, it has to be adjusted. In fact, actual starting time is also uncertain (it has to be defined with seconds of accuracy). Given the delayed response of the cable to the heating and the limitation to 10 s of the DTS sampling frequency, it is difficult to measure directly. Because of this, we

adjusted the actual starting time by trial and error during the log-derivative smoothing phase. Still, the thermal capacity is sensitive to t_{con} (recall Equation 4.4b). Given its uncertainty we decided to use a theoretical heat capacity of $2.71e^6 J/m^3K$ in the calculation of the groundwater velocity. The resulting skin effect is estimated to be 1.95 °C, thus a 55% (Equation 4.8) of the temperature increase is due to the cable materials.

Finally, groundwater velocity can be estimated by applying the analytical method in three different ways. The first approach uses the conduction characteristic time (t_{con}). This method does not require the skin effect correction, as it does not use the maximum temperature. Graphically, the (t_{con}) can be identified from the intersection between the aquifer conduction-dominated phase and the advection-dominated phase. The groundwater velocity was then estimated to be $3.7e^{-6} \pm 4e^{-7} m/s$ (Equation 4.7). In the second approach, we consider the effect of two parallel heaters through Equation 4.6. As there is no analytical solution to calculate q_x from this equation, q_x is obtained by interpolating the curve of versus q_x (see Figure 4.3b). The estimated groundwater velocity was $7.4e^{-6} \pm 2e^{-6} m/s$. The third approach considers both parallel heaters and their orientation with respect to the observation point and groundwater flow direction. A sensitivity analysis of Equation 4.9 to x was performed (data not shown), which resulted in the selection of an x value equal to the cable diameter. The estimated groundwater velocity was $8.4e^{-6} \pm 2e^{-6} m/s$.

Figure 4.10 presents the vertical distribution and dispersion of the maximum temperatures (corrected for the skin effect), estimated thermal conductivities and groundwater fluxes for each depth that reaches steady-state. Groundwater flux estimates show larger variability when two heating lines are considered in the interpretation. Nevertheless, the analytical approaches considering two parallel heaters provide closer estimates of the groundwater flux to those obtained from pumping rates, than the estimates obtained by the method considering a single heating line.

4.6 Discussion

Measured heat dissipation curves (Figure 4.8 and 4.9) are surprisingly similar to theoretical predictions (Figure 4.4). However, the actual estimated parameters are somewhat different from expected values. The estimated thermal conductivity ($0.7 - 0.8 W/m^oC$, see Figure 4.10) is lower than expected ($1.8 \tilde{} 2.2 W/m^oC$) for a saturated sandy soil with a porosity of 0.35 (Stauffer et al., 2014). However, lithology indicates the presence of silty/clay layers and organic matter, with a much lower thermal conductivity. Additionally, it is

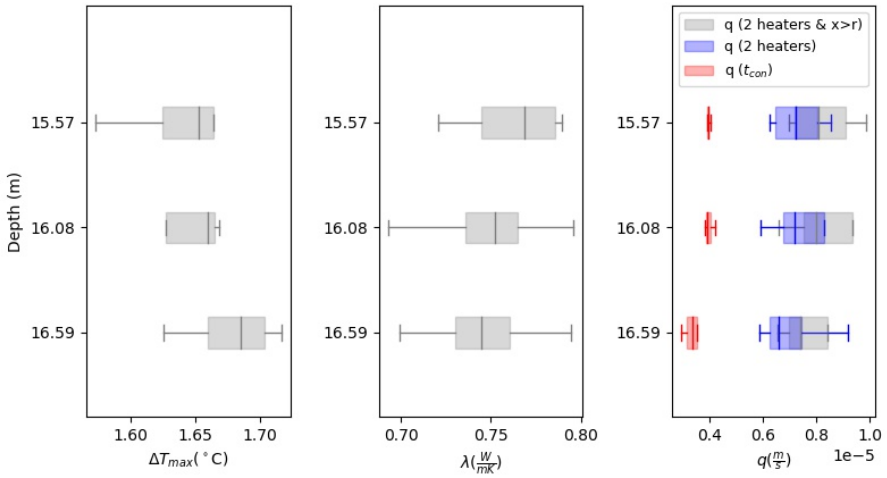

Figure 4.10: Boxplots illustrating the vertical distribution of maximum temperatures without skin effect, thermal conductivity and groundwater velocity. Box plots distribution is calculated for each depth where temperature reaches steady-state,with the four available heating curves (Figure 4.8b). The colours of the boxplots illustrate the variability of the three different analytical approaches to estimate q_x.

feasible to expect larger values of porosity in such an unconsolidated formation $(0.4 - 0.5)$. In such case, thermal conductivity values range between 0.7 and 1 W/m^oC, a range that is consistent our estimates (Figure 4.10).

Estimated groundwater velocity is smaller in comparison with the value obtained with the pumping rate ($5e^{-5}$ m/s). This discrepancy could be due to different reasons belonging to three main groups: 1) water flow assumptions and 2) analytical approach and post-processing of the FO-DTS data, and 3) the field set-up and Heat Dissipation Test implementation.

Regarding the first, groundwater flux was estimated under the assumption of homogeneous horizontal radial flow. This assumption sounds realistic because the aquifer presents strong vertical heterogeneity, which might concentrate velocity through localized layers. Moreover, piezometers are partially penetrating (only 2 m open interval) which leads to vertical fluxes towards the screened section. In fact, all piezometers responded to pumping (data not shown), which suggests that flow might be spherical around the screened interval. Worse, the most conductive layer does not appear to be the one we tested, but the one below. In this case, one should expect a significant vertical flow

near the well and a reduction of the radial component. In short, flux direction and magnitude can be modified in the vicinity of the observation piezometer, which might lead to an over or underestimation of the flux, with respect to assumed ideal radial flow. Therefore, the identified discrepancy between the groundwater velocity derived from the heating curves and thus derived from the pumping test, might come from the interpretation of the latter.

Discrepancies may also be caused by difficulties with the test itself. These difficulties may be of two kinds: (1) the analytical approach and post-processing of the FO-DTS data, and (2) the field set-up and Heat Dissipation Test implementation. While the conceptual model accounts for cable and borehole thermal effects ("skin effect"), further research needs to be done to characterize the cable materials and properly quantify the skin effect. Additionally, the application of the analytical approach requires graphical identification of the conduction-dominated phase slope (m), initial time (t_0), and conduction characteristic time (t_con) which has associated some deviation. For example, for the estimation of the thermal conductivity, the lack of a constant plateau in the temperature log-derivative from which to infer the slope of the conduction-dominated phase adds uncertainty to the method. This uncertainty coupled to the low early time sampling frequency provided by the DTS, may cause errors in the estimation of thermal conductivity and water flux. Finally, noise removal algorithms and graphical interpretation are a source of uncertainty, as they depend on the user knowledge about the conceptual model underlying the data.

Referring to the field application of the method, some sources of uncertainty can arise from the installation of the cable and performance of the heat dissipation test. The main difficulty of the cable installation was to reduce the amount of connections along the cable. Additionally, the method proved highly sensitive to a possible separation between both cables and the relative orientation of them with respect to the flux. Given the complexity of the installation, it is easy to imagine both cables might be separated several centimetres at certain points, resulting in a considerable error when solving Equation 4.9. When performing the heat dissipation test, ensuring cable constant heating requires periodic monitoring of intensity and voltage evolution in order to validate constant power injection. Additionally selection of power to be injected depends on the electric installation and the cable length to be heated. The longer the cable the higher power the system will require in order to reach the same power per unit length of cable. Fortunately, in this case, power injection should be minimized to avoid convective fluxes, yet another limitation of the method. One of the major sources of uncertainty in the interpretation of the data is the maximum acquisition frequency of DTS, in this case 10s. Exact

monitoring of the heating initial time is essential for proper characterization of the heating curve, as the method is very sensitive to the initial time and skin effect values that depend on the initial moments of the heating curve.

4.7 Conclusions

We presented a methodological approach to perform heat dissipation tests with a single FO cable in order to quantify groundwater fluxes and thermal properties. The method is based on the interpretation of the heat dissipation curves generated by a single heating and monitoring FO cable, situated between the piezometer and the aquifer matrix outside the well casing. Complementarily, a new approach to approximate the existing MILS analytical solution was presented for the interpretation of the heat dissipation curves. A correction for the skin effect generated by the low thermal conductivity of the cable and borehole materials is included in the interpretation. The proposed methodology to interpret the heating curves comprises five steps; (1) temperature calibration, (2) noise removal, computation of temperature log-derivative and conceptual model identification, (3) skin effect correction, (4) estimation of thermal properties from conduction-dominated phase slope and initial time, and (5) estimation of groundwater velocity with conduction characteristic time or corrected maximum temperature.

There are three main contributions of this study: 1) the field set-up to carry out heat dissipation tests, 2) the approach to approximate and adapt the existing analytical solution to the interpretation of the resulting heating curves and 3) the testing of both at the field scale. Furthermore, the proposed method has several advantages: i) FO-DTS is installed as an additional downhole technology, which can be deployed in parallel to other borehole devises, ii) the single heating-monitoring cable approach reduces costs and simplifies its installation, and iii) the analytical approach provides a simple way to interpret heating curves, likewise well hydraulic analytical solutions.

The method presented is a step towards generalised use of heat dissipation tests with FO-DTS not only for aquifer hydraulic characterization but also for the hydrology field. Obtained results are consistent with the expected variability of groundwater flux, although with some discrepancies in the actual values. We attribute these discrepancies to the effect different uncertainties (soil heterogeneity, vertical fluxes or thermal properties of cable and borehole materials). Therefore, further research is needed to overcome these uncertainties both at the field and during interpretation of the data. Improving quantification of the "skin" and aquifer heterogeneity effects are identified as priority topics for future research.

Chapter 5

Is temperature a valid proxy to study seawater intrusion dynamics?

In this chapter we propose the use of temperature as a natural tracer for the characterization of the seawater intrusion (SWI) dynamics in coastal aquifers. This proposal lies on our interest in using fiber optic in-situ measurement techniques, such as Fiber Optic Distribute Temperature sensing, which could provide larger amounts of data than traditional techniques based on tracing solutes. In order to understand how solutes and temperature dynamics behave at the SWI, we build two numerical models. Based on the interpretation of the model results we conclude that temperature on its own provides information about the position of the fresh-saltwater interface, and about the flow direction and rates in multilayered aquifers. However, temperature and solutes distribution comparison is neither exact nor straight forward.

5.1 Introduction

The seawater intrusion (SWI) is subjected to the influence of processes at a wide range of temporal and spatial scales. The complexity and interaction of these processes represents an obstacle for its detailed characterization and monitoring. One of the monitoring techniques that can offer large amounts of in-situ data, is the Fiber Optic Distributed Temperature Sensing (FO-DTS). This technique provides temperature data with a high spatial and temporal resolution. We tested this technology in the field in two occasions (June and September 2015), to detect the temperature spatial distribution at the SWI (Chapter 2). The results show a spatial correlation between the temperature recorded by the FO-DTS, with the resistivity data obtained by the CHERT (Cross-Hole Electric Resistivity Tomography). This indicates that FO-DTS may be useful as well for continuously monitoring the SWI. However, in order to propose this technology as a possible alternative for coastal groundwater monitoring, we need to answer a more fundamental question: Can temperature be used to monitor the seawater intrusion dynamics? This chapter aims to answer this question.

Temperature has been used as natural tracer in multiple fields involving transport in saturated porous media. For example, in civil engineering to trace leakage through embankments (Perzlmaier et al., 2006), in geothermal energy to detect heat fluxes (Ziagos and Blackwell, 1986), or in the management of artificial recharge to estimate recharge rates Becker, Bauer, and Hutchinson (2013). In the field of applied hydrogeology, the use of temperature to trace groundwater processes has increased in the last two decades (Anderson, 2005; Rau et al., 2014; Saar, 2011). A reason may be precisely, the improvement in the resolution and accuracy of temperature sensors, as well as the development of new ones, such as methods employing fiber optics (Shanafield et al., 2018).

Two approaches can be found in the literature on the use of temperature as a natural tracer for groundwater processes. (1) Applications focused on the shallow subsurface. This corresponds to the first 10 to 15 m depth approximately, where the dominant process is the influence of the atmospheric or surface water temperature. These types of applications usually benefit from the contrast between the highly variable temperature signal of the shallow groundwater and the more stable geothermal gradient of the seeping groundwater. (2) Applications focused on the deep subsurface, at which the influence of the surface temperature is negligible. At these depths, deviations from the geothermal gradient can only be attributed to groundwater flux patterns, distribution of thermal properties or the influence of heat sources (Domenico and Palciauskas, 1973).

Applications in inland aquifers (outside the influence of the sea) of the use of temperature as natural tracer are abundant. At the shallow subsurface, temperature has been mainly used to study groundwater-surface water interactions (Vogt et al., 2010; Duque et al., 2016; Mamer and Lowry, 2013; Sebok et al., 2013; Hare et al., 2015). On the other hand, at depths where influence of atmospheric thermal conduction vanishes, applications focus on surface-groundwater interactions, such as the identification of regional scale recharge-discharge pathways (Saar, 2011; Forster and Smith, 1989) or the quantification of vertical groundwater fluxes (Bredehoeft and Papaopulos, 1965; Stallman, 1965; Li et al., 2019; Bense et al., 2017; Irvine et al., 2017).

In coastal aquifers, many of the applications found in the literature concentrate on the first meters of the subsurface beneath the beach and the near-shore sea-bottom. In this approaches temperature has been mainly used to identify discharge areas (Henderson et al., 2008; Vandenbohede, Louw, and Doornenbal, 2014; Debnath et al., 2015; Dale and Miller, 2007), to quantify vertical fluxes of discharging groundwater (Land and Paull, 2001; Keery et al., 2007; Tirado-Conde et al., 2019), to study the temperature dynamics at beach scale (Pollock and Hummon, 1971; Wilson, 1983; Befus et al., 2013) or to detect the effects of sea flooding (Vandenbohede and Lebbe, 2011).

In contrast, few applications are found in the literature at deeper levels of the subsurface. Taniguchi (2000) manages to delineate the fresh salt water interface by measuring the modification of the temperature with respect to the expected geothermal gradient. Fidelibus and Pulido-Bosch (2019) were able to relate the position of the fresh salt water interface with the thermal field at regional scale for a karstic aquifer in the South of Italy. Kue-Young et al. (2008) found that temperature and solutes present different amplitudes in response to the sea-tides, depending on the part of the interface they were observing and on the permeability of the layer they were confronting. Taniguchi, Turner, and Smith (2003) quantified vertical seepage fluxes by adapting the classical Bredehoeft and Papaopulos (1965) and Stallman (1965) solution. Niroshana Gunawardhana and Kazama (2009) developed a series of type curves to estimate temperature distribution from the seashore considering advective effects of tides. Most of these applications concentrate on the quantification of vertical fluxes, which may be misleading when dealing with highly stratified aquifers, where horizontal fluxes are expected to dominate. Additionally, few studies are done on the behaviour of heat and solutes under transient conditions. Still, all of them are good examples of how heat can be used to identify, delineate or quantify different aspects of the SWI.

Aside field applications, numerical models on their own are a good tool to

study the coupled effect of solutes and heat transport in coastal areas. However, few models could be found in the literature. The benchmark of Langevin, Dausman, and Sukop (2010) is one of the publications that simulated the classic laboratory experiment by Henry and Hilleke (1972). However, they concentrate exclusively on the validation of their code at the lab scale. At field scale, Vandenbohede and Lebbe (2011) simulated the temperature distribution in a relatively homogeneous coastal sandy aquifer in Belgium. To our knowledge, this is the most relevant study at field scale using a numerical model to study the coupled effect of temperature and solutes at the interface between fresh and salt groundwater near the coast. Still, they mainly focused on the effects of marine flooding, although they modelled the vertical temperature profile. They concluded that the dominant heat transport mechanisms was conduction, as most processes affecting temperature distribution were connected to the vertical influence of the atmospheric temperature or the sea. Moreover, no concrete recommendation was provided about how temperature can be used in monitoring the SWI. Despite the lack of publications, numerical models seem to be the most suitable tool to start analysing heat and solutes transport behaviour at the SWI from a theoretical point of view.

Based on the reviewed literature and the preliminary results described in Chapter 2, we hypothesized that the thermal signature of fresh and salt groundwater can be used as a proxy for the solutes distribution at the SWI. Based on this hypotheses, temperature distribution should be related to the solute distribution, and therefore to the groundwater flow.

To confirm this hypothesis, we will study how solutes and temperature transport compare at the SWI in a coastal aquifer by means of numerical modelling. First, we use an idealized case, in which the effects of steady horizontal flux on the thermal vertical profile is analysed. Second, we use a coupled heat and solute transport model at field-scale, with which we will characterise the solutes and temperature dynamics under different external stimulus and timescales. Both models, with different levels of simplification, are based on the Argentona coastal research site, from which flow, solute and bulk resistivity data characterizing SWI is available over a period of two years. The site, serves as an example of the processes that can drive the SWI in a heterogeneous unconsolidated aquifer. Finally, we propose a conceptual model of the thermal behaviour of the SWI, which can be used to relate temperature to solute dynamics for monitoring purposes.

5.2 Governing equations and numerical methods

The partial differential equation for mass conservation of the aqueous or fluid phase in porous media can be written as:

$$\frac{\partial}{\partial t}(\rho\phi) + \nabla \cdot (\rho \mathbf{q}) = 0 \tag{5.1}$$

where ρ is the fluid density Kg/m^3, ϕ is the porosity, $\mathbf{q}$ is the flux of water m/s. The last is described by Darcy equation, in this case, in its generalized form in order to account for variable density:

$$\mathbf{q} = \frac{\mathbf{k}}{\mu}(\nabla P + \rho g \nabla z) \tag{5.2}$$

where $\mathbf{k}$ is the intrinsic permeability, μ is the viscosity, g is the gravity acceleration and z is the elevation.

Both temperature and solutes effects the density, which is considered through the density function:

$$\rho = \rho_{l0}(1 + \beta(P_l - P_{l0}) + \gamma w + \alpha T) \tag{5.3}$$

where ρ_{l0} is the reference density of the liquid phase in Kg/m^3, β is the water compressibility in MPa^{-1}, P_{l0} is the reference pressure in MPa usually considered as the atmospheric pressure ($0.1MPa$), γ is the solutes expansion coefficient and α is the volumetric thermal expansion coefficient in $^oC^{-1}$. Therefore, the density variation due to temperature, pressure or solutes variations is coupled to the Darcy flux through this function.

The mass conservation of solute can be expressed as:

$$\frac{\partial(\rho\phi w)}{\partial t} = \nabla \cdot (\phi\rho(\mathbf{D}_{dif} + \mathbf{D}_{dis})\nabla w) - \nabla \cdot (w\rho\mathbf{q}) \tag{5.4}$$

where w is the mass fraction of the solute in liquid phase in Kg/Kg and D_{dif} and D_{dis} are tensors for diffusion and dispersion m^2/s.

The energy balance can be expressed as:

$$C_b \frac{\partial T}{\partial t} = \nabla \cdot ((\lambda_b + \phi_w \mathbf{D}_{dis})\nabla T) - \nabla \cdot (C_w T \mathbf{q}) \tag{5.5}$$

where λ_b is the bulk thermal conductivity in $J/^oC/m/s$ and C_b is the bulk thermal capacity. The last can be calculated as $C_b = \phi C_w + (1 - \phi)C_s$, where C_w and C_s are the water and soil thermal capacities respectively $J/^oC/m^3$.

Both heat and solute transport equations are analogous. This becomes more patent if equation 5.4 is divided by the C_w:

$$\phi R \frac{\partial T}{\partial t} = \nabla \cdot ((D_t + \phi_w \mathbf{D}_{dis}) \nabla T) - \nabla \cdot (T\mathbf{q}) \tag{5.6}$$

Then $\frac{\lambda_b}{\phi C_w}$ becomes the thermal diffusion D_t coefficient ($m^2 s^{-1}$), and $\frac{C_b}{C_w \phi}$ becomes the retardation factor R. This form of the heat balance equation is more illustrative to discuss the difference and similarities between heat and solute transport.

Although, both solutes and heat transport equations present advective and diffusive terms, the contribution of each mechanism to both transports is very different. Heat transport is usually dominated by conduction (comparable to diffusion), whereas solutes transport is dominated by advection. This is partly explained by the larger values of thermal diffusion ($10^{-1} - 10^{-3} cm^2/s$), as heat has the capacity to be transferred through solid and fluid phases, in comparison to molecular diffusion ($10^{-6} cm^2/s$), which only transfer through water (Anderson, 2005). With respect to the role of the thermal dispersivity, there is an open debate in relation to its magnitude, where some authors consider it negligible and others with the same magnitude as dispersivity for solutes (Vandenbohede, Louwyck, and Lebbe, 2009). Equations 5.6 and 5.7 assumes the latter.

The mentioned difference can vary depending on the importance of advection with respect to diffusion/dispersion. Advection depends on the flux rate, and therefore, for large flow rates advective heat transport can dominate over conductive transport. In those cases, the difference between the solutes and heat front velocity is determined by the retardation factor (Russo and Taddia, 2010) as: $v_T R = q/\phi$.

Therefore, an interesting aspect to assess systematically would be the relative importance of diffusion versus advection. This is traditionally done with the thermal Peclet number:

$$Pe = \frac{L \phi \rho_w c_w v}{\lambda_b} \tag{5.7}$$

The Pe results from dividing the advective and conductive terms. Therefore, if this value is larger than 1, advection should dominate. However, the Pe is scale dependent, and therefore misleading. At larger scales (L) and times (t), advection always dominates. This is specially important if temperature gradients are small, as is the case at large depths where temperature does not oscillate.

We will use CODEBRIGHT to solve the described mass and energy balance equations. CODEBRIGHT is a 3D finite-elements multi-phase flow and heat transport code able to solve coupled thermo-hydro-mechanical (THM)

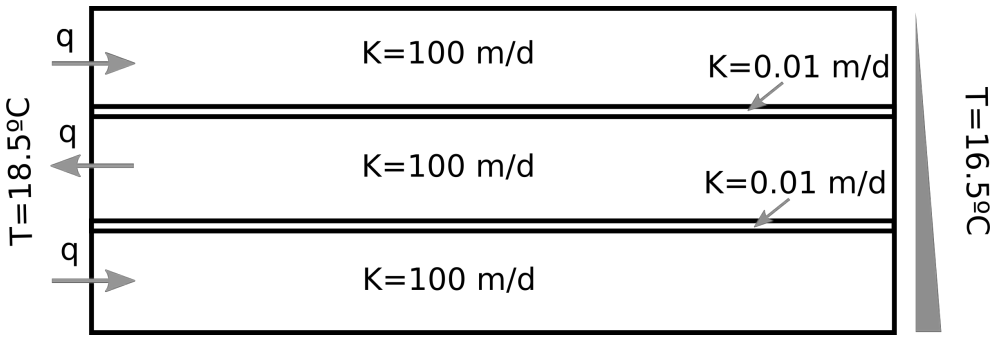

Figure 5.1: Schematic cross-section depicting the simplified model geometry.

problems in porous media (Olivella et al., 1996). In this case, we neglected the mechanical component of the problem, and focus on the coupling between heat and solutes (TH). CODEBRIGHT uses the compositional approach to establish the mass balance equations (Olivella et al., 1996). The code considers the three phases as solid (s), liquid (l) and gas (g) phases, and the species as salt (h), water (w) and air (a). In this case, we consider fully saturated media, therefore air and gas phase drop from the balance equations. The state variables are pressure (P), temperature (T) and mass fraction (w), expressed in MPa, $^{\circ}C$ and Kg/Kg respectively.

5.3 Model of simplified case

A simplified case was designed in order to understand the processes driving heat transport at the SWI. We will model the influence of the horizontal advection and conduction between two groundwater bodies at different constant temperatures. We will focus on studying how the interaction between both processes will affect the vertical distribution of temperatures.

We modelled a 2D vertical cross-section of 20 by 50 m including three aquifer levels separated by two thin confining layers (Figure 5.1). This geometry was the result of several considerations. First, we consider groundwater flux near to the coast mainly perpendicular to the seashore. And secondly, we focus on the transport in unconsolidated coastal aquifers, which are usually formed by multiple aquifer levels separated by horizontal (semi)impermeable layers.

As the focus is on the analysis of the temperature distribution, we simplify the problem by only considering heat transport and groundwater flow. We

do not consider solute transport, and thus we will assume constant density. To simulate the temperature difference between two independent groundwater bodies, we prescribed two constant temperatures at both left and right sides of the domain, with a 2°C difference between both. As we focus on the temperature distribution below the atmospheric temperature influence depth, we do not need to set any temperature boundary condition at the top. Moreover, we also neglect the effect of the geothermal gradient as it will not provide any added value to the analysis.

With this very simple model, we will test the effect of confronting groundwater fluxes with different rates. In layered coastal aquifers, the seawater intrusion front travels at different rates in each layer depending on the connectivity to the sea and the permeability of the geologic materials. It is often seen that seawater intrusion travels inwards through one layer, while in the over- or underlying layers, fresh water travels seawards. To test this scenario, we set a fixed hydrostatic pressure boundary condition on the right side, and a fixed flux boundary on the left. On the left side flux rates on the top and bottom layer were positive (inflow), while negative on the middle layer (outflow). This scheme aims to mimic the process on horizontal seawater intrusion through a permeable layer, without considering solute transport. We assumed steady state for both groundwater flow and heat transport. Three different flow rates ($1e^{-2}$, $1e^{-3}$ and $1e^{-4}$ kg/s) were applied.

5.4 Field-scale model

A field-scale numerical model including coupled heat and solute transport is built to analyse more complex and realistic dynamics. The model is inspired by the research site of Argentona (Figure 2.1). This site is a good example of unconsolidated coastal multilayered aquifers.

5.4.1 Field site

The Argentona research site has been intensively characterised (Chapter 2 and 3) and monitored (Palacios et al., 2020) between 2016 and 2019.

The site is characterized by three aquifer levels separated by semi-impermeable silty-clay layers. This multilayered aquifer is part of a larger formation, composed of interspersed deltaic and marine sediments. At the bottom of the research site weathered granite was found. Granite is believed to underlay the weathered layer acting as the impermeable bedrock. The available lithological descriptions are restricted to those performed in the boreholes of the research

site. Therefore, continuity of the layers to the sides, or the possible presence of paleochannel are not known beyond the studied site.

The available monitoring information includes continuous records of heads, concentrations and temperature at the screen interval of each borehole, periodic cross-hole electrical topographies (Palacios et al., 2020), induction logs, periodic electrical conductivity measurements from sampled groundwater and two punctual FO-DTS temperature measurements. Based on these data, we could characterise the SWI and identified multiple dynamics at different temporal (hours to years) and spatial scales (cm to m).

For the sake of simplification, we focus on reproducing some of the most relevant features of the SWI observed at the lower aquifer located below the -10m semi-confining layer: (1) the oscillation of groundwater heads in most boreholes; (2) the general solute distribution between aquifer layers; and (3) the solutes dynamics in response to long term recharge cycles.

5.4.2 Geometry

The problem is simplified in a 2D vertical cross-section assuming groundwater gradient direction is perpendicular to the seashore (Figure 5.2). The upstream limit coincides with the position of an independent borehole, located at 300 m from the research site, which will serve as the inland boundary condition. The model extends 300 m inland and another 260 meters offshore. The model's onshore elevation does not aim to represent the reality, as the upper model layer has been given a large specific storage in order to act as a phreatic surface. On the other hand, the offshore segment of the top boundary does represent the real bathimetry profile.

As stratification is predominantly horizontal, the model is composed of eight horizontal layers, four permeable and four semi confining. This distribution and number of layers is derived from the combined interpretation of the geophysical data in Martínez-Pérez et al. (2020) and the long pumping test calibration (Chapter 3). Based on this initial geometry we added an additional semi-confining layer at - 5m in order to account for any possible effect of the thin silty layers described at that depth. The total thickness of the model is 22 m, where the impermeable bottom represents the granite.

Because of the predominant horizontal stratification of the aquifer, regular quadratic elements were used to generate the grid. The elements height is 0.5 m and their length ranges between 2 to 0.5 m.

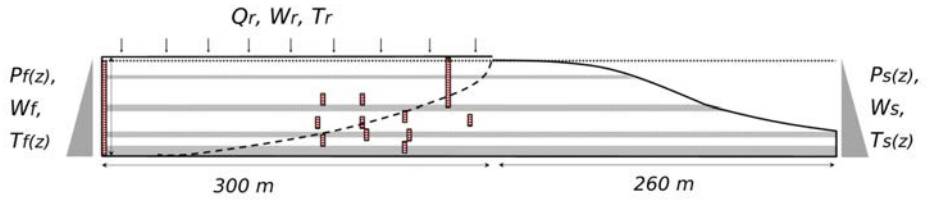

Figure 5.2: Schematic cross-section depicting the model geometry and types of boundary conditions.

5.4.3 Boundary conditions

Inland and off-shore hydraulic boundary conditions are set as prescribed time-variable heads, while the effective recharge is imposed as a flux through the top boundary (Figure 5.3).

Inland prescribed heads are defined using the monitoring data from the borehole (08029-0094), periodically monitored by the Catalan Water Agency since 2009, and intensively monitored by the research team between 2016 and 2018. The specified head boundary condition is not recommended for the inland boundary of sea shore-perpendicular cross-sectional models like ours (Jiao and Post, 2019). Specified head boundary conditions might overestimate the response of the SWI to an increase of the sea level. Despite this well documented warning, we consider the specified head boundary condition the most appropriate for these case because of two reasons. First, we do not have reliable data or a numerical model for the entire catchment to provide for accurate time varying fluxes across the inland boundary. And second, the stratification of the aquifer is an obstacle to calculate fluxes for each layer, which are thought to be different. Because of these reasons we decided to use the head boundary condition inland, making sure the resulting fluxes across the boundary were coherent with independent observed estimations.

The mean sea level in the near-by port of Mataró is periodically simulated by the Spanish Ports Authority (NIVMAR, Puertos del Estado). We use their data to feed our seaside head boundary condition. The effective recharge imposed on the upper boundary, is calculated using a water balance in the soil that takes into account rain and evaporation similar to WatBal (Yates, 1996). The model was applied using meteorological data - precipitation, atmospheric temperature and net solar radiation - from the near-by meteorological station of Cabrils (MeteoCat).

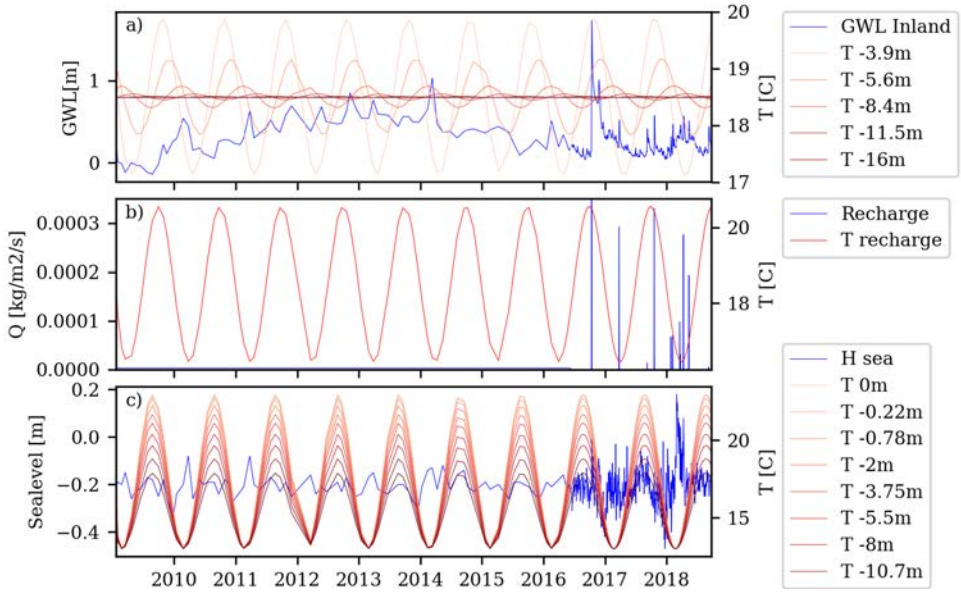

Figure 5.3: Time series of boundary conditions imposed on the numerical model. a) Inland boundary conditions, b) Top boundary condition, and c) Seaside boundary condition. The blue lines represent the hydraulic boundary conditions times series. The red lines represent the temperature data. The light reds represent the shallower temperatures and dark reds represent the deeper temperatures.

The vertical temperature distribution at the inland boundary conditions was calculated using the one-dimensional vertical conductive heat transport analytical solution propose by Gröber, Erk, and Grigull (1955)(Stauffer et al., 2014). The analytical solution was manually adjust to the available DTS vertical profiles at different boreholes. The resulting mean aquifer thermal conductivity and thermal capacity were used to calculate time and depth dependent temperatures at the recharge and inland boundaries. To simulate the temperature at the upper boundary condition - that is, the recharging water - temperature time series at 3 m depth - approximately the groundwater depth - were estimated by means of the analytical solution and the mentioned thermal parameters (red lines in Figure 5.3b). Temperature was calculated at nine different depths (0 to 21.3 m) in order to provide a realistic temperature profile at the inland boundary (red lines in Figure 5.3a).

Time and depth dependent temperature values were prescribed at the sea side boundary condition. We adjust a simplification of the conductive heat transport equation mentioned above, to the sea surface water temperature data from Mataró Port (NIVMAR - Puertos del Estado) and the temperature vertical profiles provided by (Vargas-Yáñez et al., 2017). Temperature of the sea water was estimated at seventeen depths, in order to reflect the temperature vertical distribution beneath the sea. Notice that average temperature of the sea decreases with depth.

The initial conditions were established by running the model until a stationary state considering mean annual values (between 2016 and 2018) of the boundary conditions. A total period of 10 years was simulated, divided in two segments. The initial period, between 2009 and 2016, is designed to reproduce the long term trends of seawater intrusion. This is specially important for arid areas like the Mediterranean coast, where recharge patterns present periods of several years. This can be appreciated in the groundwater levels evolution at the inland boundary piezometer (blue line in Figure 5.3a). The second period from June 2016 to December 2018 represents the period for which we have detailed monitoring data at the research site.

5.4.4 Parameterization

The numerical model was parameterized with the values specified in Table 5.1. We used approximately the thermal conductivity estimated through the Heat Dissipation Test described in Chapter 4. Initial values of hydraulic conductivity were obtained from the interpretation of a pumping test (Chapter 3). Although these initial values of hydraulic conductivity provide a good match of both simulated and observed groundwater heads oscillations, the solute distribution and dynamics did not compare well with the observed data. Therefore, a manual calibration was carried out focusing first on reproducing the groundwater head oscillations, and second, on reproducing key features of the solutes distribution and dynamics. These are: (1) the mean concentrations at each borehole, (2) fast salinization and refreshing dynamics taking plce in the aquifer layer L6, as observed in (Palacios et al., 2020), and (3) increasing concentrations during the monitored period in wells screened at layer L6. The resulting hydraulic conductivity (Table 5.1) reproduces the general dynamics of the SWI.

Table 5.1: Parameters for numerical simulations of the field-scale model.

Parameter	**Units**	**Value**
Gravity	m/s^2	10
Dynamic viscosity	kg/m·s	0.001
Porosity		0.3
Solute diffusivity	m^2/s	1.1e-4
Longitudinal solute dispersivity	m	0.5
Transversal solute dispersivity	m	0.25
Longitudinal thermal dispersivity	m	0.5
Transversal thermal dispersivity	m	0.25
Specific heat of fluid	J/kg/K	4200
Specific heat of solid phase	J/kg/K	1074
Thermal conductivity	W/m/K	1
Density solid phase	kg/m^3	2700
Volumetric thermal exp. coef. α	C^{-1}	1e-10
Solutal expansion coef.	kg/kg	0.79
Water compressibility coef.	MPa^{-1}	4.5e-4
Reference density	kg/m^3	1000
Reference temperature	C	0
Reference pressure	MPa	0.1
Layers	**Hydraulic conductivity m/d**	
L1 Sy	1.5	
L2 AQF1	60	
L3 AQT1	35	
L4 AQF2	35	
L5 AQT2	0.5	
L6 AQF3	400	
L7 AQT3	0.1	
L8 AQF4	1	
L9 AQT4	0.01	

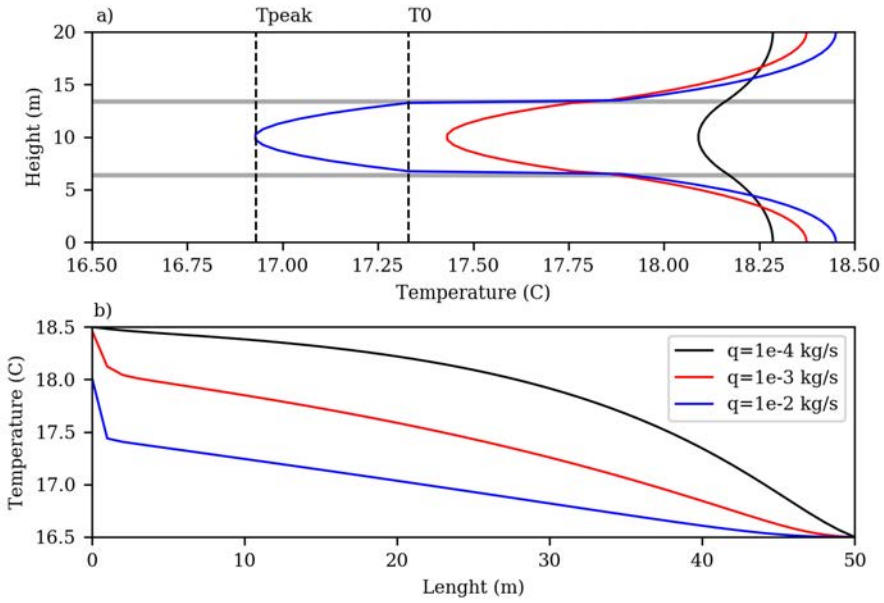

Figure 5.4: Results simplified model. a) Temperature vertical profiles at x=25m. Tpeak and T0 indicate the temperature that define the parabola. b) Horizontal distribution of temperature at y=10m.

5.5 Results

5.5.1 Analysis of simplified case

The effect of horizontal flux over an homogeneous temperature vertical profile for different flow rates can be observed in Figure 5.4a. In general, we observe, as expected, that large flow rates have larger impact on the temperature profile. The thermal front is therefore able to reach further into the aquifer. In the case of the middle layer, we observed how temperature decreases approaching the temperature of the incoming water (16.6 ^{o}C at the right boundary). Three interesting features can be deduced from this figure. (1) A parabolic shape of the vertical temperature distribution is generated at the permeable layers. (2) The shape of this parabola indicates the flow direction. (3) The temperature difference between the peak of the parabola (Tpeak) and the minimum (T0) depends on the flow rate.

Additionally, we depicted the temperature distribution in the x-direction

(Figure 5.4b). In this figure some boundary effects can be observed at the left and right. Since the flow direction is from right to left, the boundary effect is sharper on the left side. In any case, these effects vanish at the middle of the domain. Interestingly, we can observe - ignoring the mentioned boundary effects - how the temperature distribution becomes linear for large flow rates. This temperature distribution indicates that the vertical parabolic shape remains constant in x for large flow rates.

These results suggest that in layered coastal aquifer, where groundwater flow is predominantly horizontal, temperature vertical profiles will be affected by changes in the flow direction and rate. Thus, changes between fresh- discharging groundwater and intruding saline groundwater could be possibly detected by analysing the anomalies in the temperature vertical profiles.

One of the most interesting features of these results is the shape of the temperature parabolic curves. This shape is controlled by three parameters: the maximum temperature difference between T0 and Tpeak, the thickness of the layer and the flow rate (Figure 5.4a). Thereby, this parabolic curve can be expressed as:

$$T(y_D) = \frac{1}{2} y_D^2 \left(\frac{qC_w L_y^2}{L_x \lambda} \frac{\partial T}{\partial x_D} \right) - \frac{1}{2} y_D \left(\frac{qC_w L_y^2}{L_x \lambda} \frac{\partial T}{\partial x_D} \right) + T_0 \qquad (5.8)$$

where, Y_D is the dimensionless y-axis ranging between 0 to 1, L_x is the characteristic length in the horizontal direction, L_y is the characteristic length in the vertical direction, and $\frac{\partial T}{\partial X_D}$) is the horizontal temperature gradient. Further details on the derivation of this equation are included in Annex C.

Based on this equation we can relate the parameters determining the parabolic shape (Tpeak layer thickness and horizontal temperature gradient) to the flux rate. Assuming constant $\frac{\partial T}{\partial X_D}$we estimated the flow rates for each of the three simplified models. The $\frac{\partial T}{\partial X_D}$ is calculated by the ratio between the temperature difference between both boundary conditions and the model length. The resulting flow rates are $-1.1e^{-2}$, $-9.3e^{-3}$ and $-1.8e^{-3}$ $kg/m^2/s$ for each simplified model, where the original flux rates imposed at the boundary condition were $-1e^{-2}$, $-1e^{-3}$ and $-1e^{-4}$ $kg/m^2/s$ respectively. Notice that the negative values indicate flow direction from right to left. As flow rate decreases, the assumption of linear horizontal temperature gradient becomes completely invalid, and thus the estimated flow rate. However, for large flow rates, the temperature gradient in the x direction remains constant and the flow rate estimation is more accurate.

This analytical approach confirms that the shape of the curves generated by horizontal groundwater flux between two groundwater bodies at different

temperatures can provide useful information. We could deduce the direction of groundwater flux and estimate the flux if groundwater flux is large enough to produce linear temperature gradients along the x direction.

5.5.2 Analysis of field-scale model

Groundwater heads, solute concentrations and temperature were modeled at field-scale for two years and a half. The geometry and boundary conditions of the model are inspired by the Argentona research site. A simple manual calibration of the hydraulic parameters was performed attending to the observed data on groundwater heads and concentrations.

Simulated groundwater head oscillations match well with the observed ones, collected between June 2016 and December 2018 (Figure 5.5). The quick reaction of groundwater levels to the changes induced by the boundary conditions fluctuations, could only be reproduced with a low storage coefficient (Ss = 1e-4). This confirms the hypotheses of a semi-confined system with multiple aquifer levels derived from the interpretation of the pumping test (Chapter 3).

As can be observed in Figure 5.5 groundwater heads in all boreholes behave similarly, responding to the regional aquifer oscillations (green line in Figure 5.5a) and to the mean sea level oscillation (blue line in Figure 5.5a). We observed that the groundwater levels were not sensitive to the recharge at the top. The responses of the groundwater heads to the rainfall events are triggered by the fixed head inland boundary condition. PP15 and PP20 are the boreholes with the largest errors. This is specially evident during the response to rainfall events. Both boreholes are screened along their entire length, whereas in the model just a point in the middle of the screen is considered. The observed data at these two boreholes may be affected by the recharge through the part of the screened section open at a most shallow layer. This part is not considered by the model, however it may be the cause for this fast reaction in the measured heads. To a lesser extent, this observation is also valid for the N315 and N215 boreholes, whose response to rainfall events is stiffer for the observed data than for the simulated data. In other cases, the matching between simulated and observed groundwater head oscillation is good.

Concentrations resulting from the model reproduce the overall distribution and main dynamics observed in the field. Figure 5.6 shows the modelled concentrations, expressed as mass fractions (kg/kg) at steady state. The overall solutes distribution match well with the resistivity images obtained with the CHERT (Palacios et al., 2020). As in Palacios et al. (2020), the model shows a slightly sloping interface developing below the -10 m semi-confining layer. These results serve as initial conditions for the transient model.

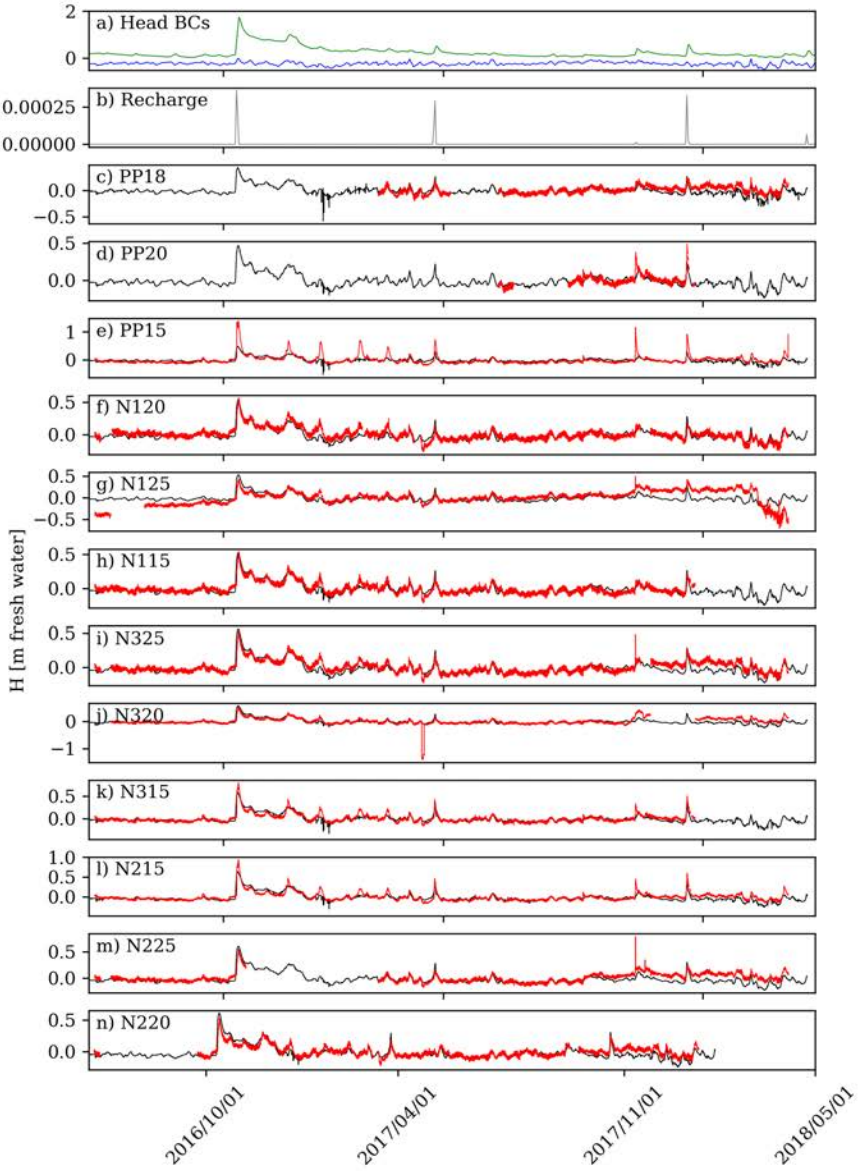

Figure 5.5: Comparison of the simulated with experimental groundwater heads. a) Heads of boundary conditions in meters above mean sea level. The green line indicates the groundwater head at the left boundary (inland) and blue red line indicates the mean sea level. b) The grey line depicts the recharge function in $Kg/m^2/s$ imposed along the top boundary. c) to n), measured (red) and simulated (black) groundwater head in m.

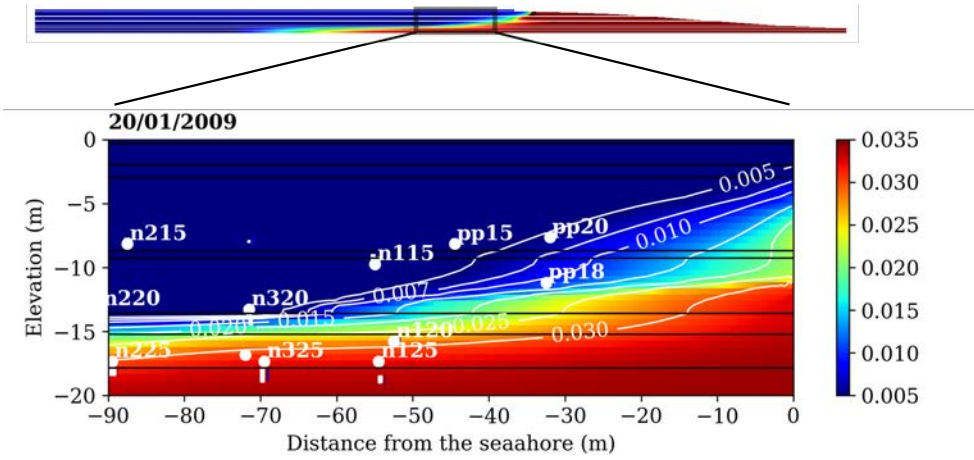

Figure 5.6: Concentration distribution at steady state, expressed as mass fractions (kg/kg). These results are obtained with annual mean values of the boundary conditions

Temporal evolution of modelled concentrations was compared to data obtained at the research site during several sampling campaigns between 2016 and 2018. Although the transient model was ran for a longer period, between 2009 and 2018, no data is available for comparison with the modelled concentration prior to 2016. Still, Figure 5.7 shows the complete transient period to put in context the dynamics observed between 2016 and 2018.

As can be observed in Figure 5.7 the concentrations tend to increase between 2016 and 2018. This is coherent with the periodic CHERT obtained during that period (Palacios et al., 2020). The model captures the overall trend of salinization, although it fails to reproduce smaller oscillations shown by the measurements. From the observation of the complete period, it is clear that the salinization process is an inter-annual process, which obeys the also inter-annual variations of the regional groundwater levels (green line in Figure 5.3a). This general tendency may be interrupted by extreme recharge events, like that occurring in October 2016 (indicated in Figure 5.7a). These types of events are able to interrupt the long-term increasing concentrations tendency, or to refresh it for a while, as can be observed in borehole N320. These patterns have been also observed in the CHERT results of Palacios et al. (2020). The model roughly reacts to this large increase in the regional groundwater heads inland. Still, we can say that the model is able to reproduce the overall dynamics observed in the system, allowing us to understand the time-scale of

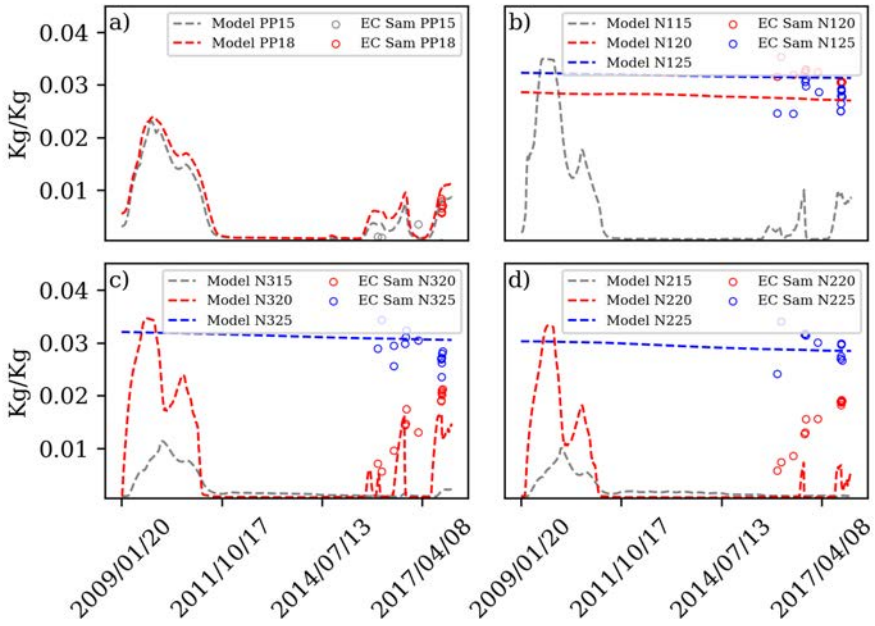

Figure 5.7: Modelled and observed concentrations. Data is grouped by location, from the sea (a) to inland (d).

the processes affecting the SWI.

When observing each layer individually, we perceive different dynamics. The boreholes, of which the screened interval is located in the permeable layer between -10 and -15 m depth (PP18, N115, N320 and N220), are the ones presenting increasing concentration between 2016 and 2018. On the other hand, the rest of the boreholes remain at relatively constant salinity. This dichotomy between the highly dynamic layer below the -10m semi-confining layer, and the less permeable layers below -15m depth is captured by the model. The highly permeable layer is also identified by Palacios et al. (2020) as a preferential path for salinization. Still, simulated solute dynamics at this layer seems to be overestimated, while underestimated in the deeper layers. We need to keep this in mind when analysing the thermal data.

Now that we have been able to show that the model reproduces fairly well the dynamics of a real aquifer system, we will show how these dynamics affect the distribution of temperatures. Therefore, the purpose of these results is to illustrate how temperature behaves given a realistic solute transport pattern.

Figure 5.8 shows the temperature distribution at the model domain for a

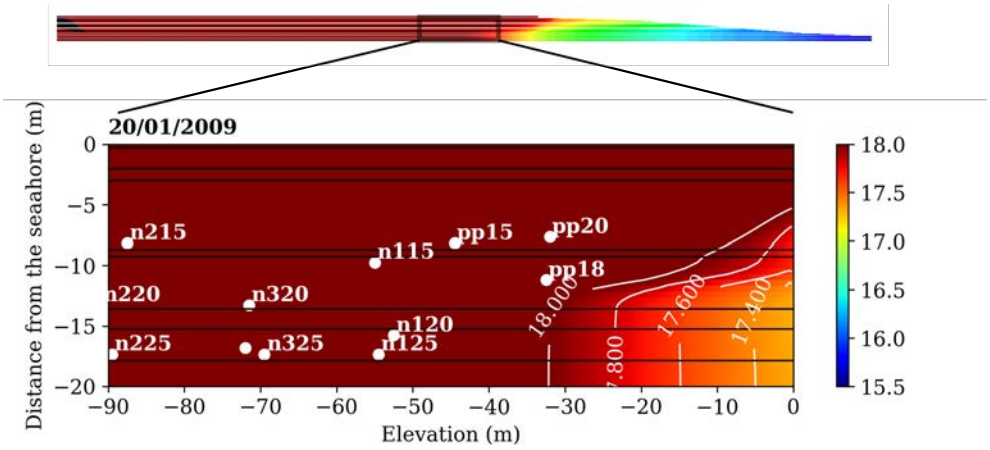

Figure 5.8: Modelled temperatures at steady state.

steady state. The first feature that stands out in this figure is the contrast between the warmer homogeneous inland water, and the progressive drop in temperature of the off-shore section of the aquifer. As explained in the boundary conditions section, temperature oscillations at sea decrease with depth. Also, the annual mean temperature of the seawater decreases with depth, as can be observed in Figure 5.8. This means that, at least at steady state, the part of the aquifer in contact with the sea reflects a decrease of temperature with depth.

At the same time, the shape of the bathymetry near the coast seems to play an important role in the temperature distribution. In this case, the small slope facilitates temperature to reach a uniform distribution in the vertical, rather than horizontal direction.

At the field-site, the lower temperature signature of the saline groundwater hardly reaches the closest borehole to the sea. However, the cold thermal signature of the saline groundwater is coherent with the FO-DTS results analysed in Chapter 2.

If we analyse the temperature behaviour in time (Figure 5.9), we observe similar patterns as those presented by the solute concentrations in Figure 5.7. Figure 5.9 depicts temperature oscillations in depth for the deepest boreholes aligned perpendicular to the sea. The larger temperature oscillations occur at the boreholes closest to the sea due to the saline groundwater influence. Three periods with contrasting behaviour can be differentiated. The first between 2009 and 2012. During this period groundwater temperature decreases and

warms up again due to the advancing and posterior retreat of the saline front. Between 2012 and mid-2015, high regional groundwater heads prevented saline groundwater to penetrate inland. As a consequence, temperatures remain constant and close to that of the warmer fresh groundwater. Finally, between mid-2015 and 2018, regional groundwater heads dropped and saline intrusion at the field-site was activated. As a response temperatures started to decrease due to the influence of the colder saline groundwater. This indicates that the influence of saline groundwater temperature can be observed at large distances from the seaside.

Taking a closer look to Figure 5.9 we observe that temperature oscillations concentrate between -10 and -12.5 m. At this depth a high conductive layer is located (L6 AQF3 in Table 5.1). Below -15m, temperature changes occur but with certain lag and smaller amplitude. This behaviour denotes that temperature at that depth is also influenced by the saline groundwater. However, groundwater flux is very small due to the small permeabilities of layers 7, 8 and 9 (Table 5.1). This is probably the reason why the temperature at the deepest part of the borehole further inland (N225) is always similar to the inland temperature (18.5°C), while being partly salinized. This suggest that a minimum flow rate is needed for the thermal signature to be observed

The most interesting aspect of this analysis is the comparison between solutes and heat transport at the SWI. Figure 5.10 presents the modelled solutes and temperature distribution at the middle depth of four representative layers for different times. The plots on the left show the temperature evolution at four different depths. The atmospheric temperature influence can be perceived in the -2.25m depth plot further inland. However this effects vanished already for the -6.8 m depth plot. It can be observed that the annual thermal oscillation concentrates at the right side of the plot, influenced by the sea. The year oscillation of the temperature of the sea water, as well as its mean, decreases with depth, from 6°C to 1°C and from 18°C to 16°C respectively. This produces a step-like shape between the inland warmer groundwater (annual mean around 18.5°C) and the offshore colder water (annual mean around 16.5°C). The most interesting feature of this step-like feature is that it advances and retreats indicating a displacement of the thermal divide between the two groundwater bodies. The amplitude of this displacement is larger in the layer L6 (around 60 m in the x direction), as we also observed in Figure 5.9.

The plots of the right present the distribution of concentrations in the x-axis for different time steps for the same four layers. The concentrations front L6 show again the largest range of displacement (150m) centered around a 100m from the shoreline. The contrast in the solute behavior between layers is obviously related to the permeability of each layer.

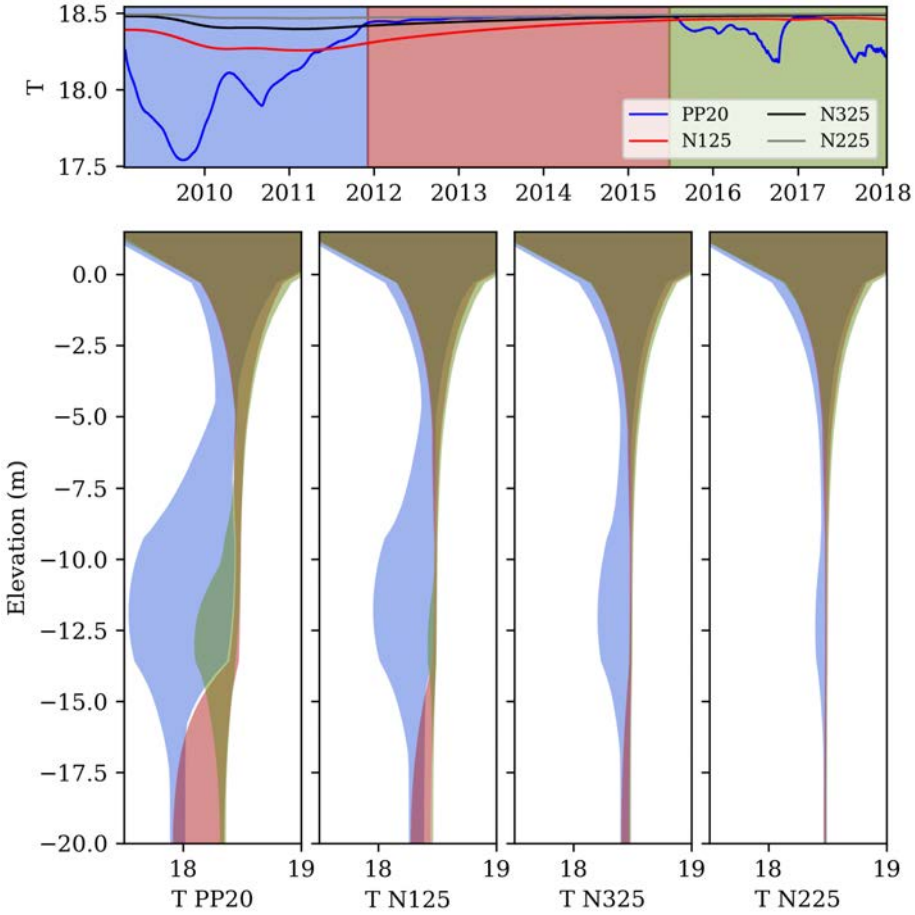

Figure 5.9: Modelled temperature profiles. The top graph depicts the temperature evolution at the screened interval of the deepest boreholes aligned perpendicular to the sea. Colored segments indicate period with contrasting dynamics: In blue a refreshing period, when temperature increases. In red a period when no changes are recorded and temperature remains constantly high. In green a period when temperatures decrease progressively. Maximum and minimum vertical oscillation in temperature for each period are plotted for each borehole. Notice the difference between boreholes in amplitude of the temperature variations between -10 and -12 meters.

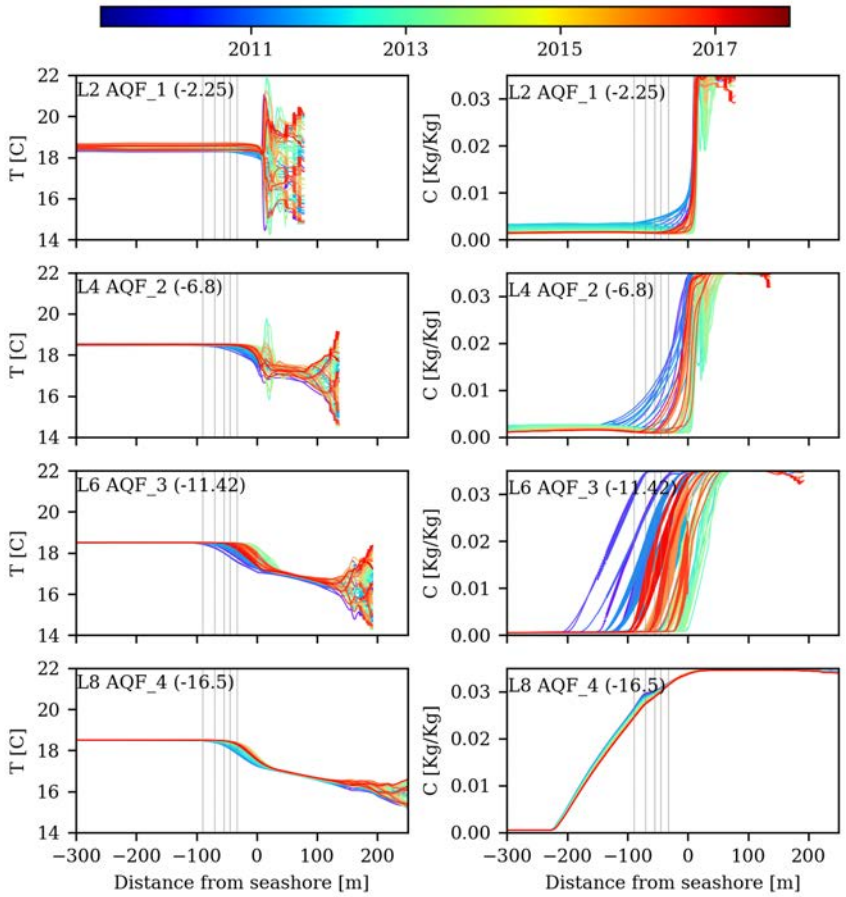

Figure 5.10: Temporal evolution of modelled solute and temperature horizontal distribution at four representative depths. Left plots shows temperature, while right plots shows concentrations, expressed as mass fractions (kg/kg). The color-bar represents the time. The vertical grey lines indicate the location of the deepest boreholes of the research site aligned perpendicular to the seashore.

If we compare both temperature and solute distributions we see several analogies and differences. The amplitude of the distance swept by the step trend of solutes is around 150m, while for the temperature is around 60m. Differences concentrate at time steps corresponding to a strong intrusion event

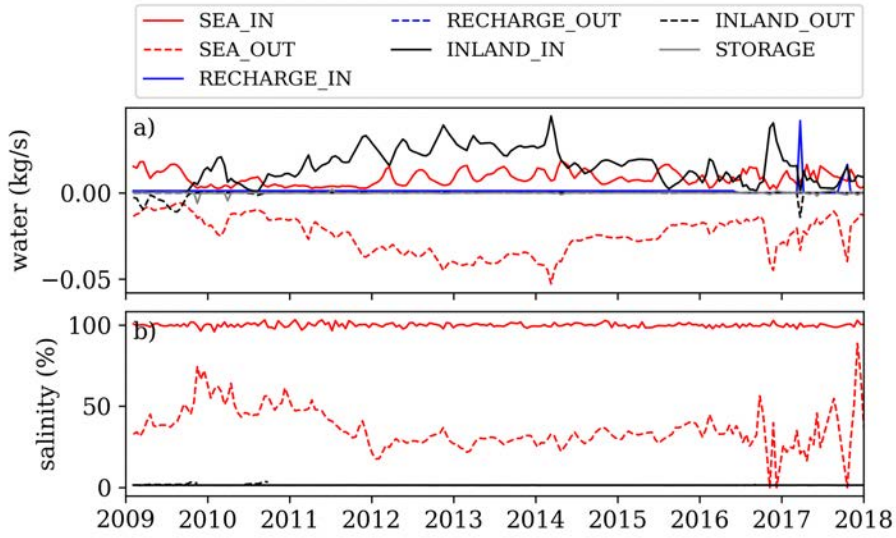

Figure 5.11: Evolution of the water balance (kg/s) and salinity (%) in time through each boundary conditions differentiating between in flowing and out flowing water.

at the beginning of the transient period (From 2009 to 2010). This reaction of the temperature and solutes distribution is not so evident in layer L8. In this layer the thermal front is located in average further seawards (around 30m from the seashore), while the average position of the solutes front surpasses the field installation (150m from the seashore). Both temperature and solutes distribution at the L8 layer do not show much oscillation, indicating stable conditions and probably very low groundwater flux as consequence of the low permeability.

Two conclusions can be derived from this figure. First, that the temperature is an indicator of the solute dynamics. But, secondly, that the behaviour between solutes and temperature is only comparable in a range of circumstances. For fast pulses, like the one occurring at the beginning of the transient period (From 2009 to 2010), temperature acts with a spatial lag. This lag is related to the retardation factor, which prevents the thermal front from being displaced as much as the solute front. At deeper layers (L7 and L8), which are also less permeable, saline groundwater seems to reach the temperatures of the surrounding fresh water, which prevents detection of salinization based on a thermal contrast.

Table 5.2: Balance considering mean values for the transient period (2009 to 2018) per layer and boundary condition. Water balance expressed in $Kg/m^2/s$. % of Salinity is indicated for the outflow through the seawards boundary conditions.

	L1	**L2**	**L3**	**L4**	**L5**	**L6**	**L7**	**L8**	**L9**	**TOTAL**
Mass	$(kg/m^2/s)$									
sea in	0	4.8e-3	3.9e-5	3.0e-4	3.2e-4	3.3e-3	2.1e-6	2.0e-5	5.1e-6	8.7e-3
sea out*	0	-2.4e-2	-3.1e-5	-7.0e-5	-1.8e-4	-1.4e-4	-2.3e-5	-3.8e-6	-6.2e-8	-2.5e-2
*(% Salinity)	(0)	(33)	(88)	(85)	(81)	(80)	(98)	(100)	(100)	(34)
recharge in	1.2e-3	0	0	0	0	0	0	0	0	1.2e-3
recharge out	0	0	0	0	0	0	0	0	0	0
inland in	1.6e-4	1.8e-3	2.0e-4	8.3e-4	2.6e-4	1.2e-2	3.4e-4	1.7e-5	1.0e-6	1.5e-2
inland out	-4.9e-7	-6.9e-5	-1.6e-5	-5.0e-5	-8.9e-6	-3.8e-4	-1.2e-5	-5.5e-7	-4.3e-8	-5.4e-4
total	1.3e-3	-1.7e-2	1.9e-4	1.0e-3	3.8e-4	1.4e-2	3.0e-4	3.2e-5	5.9e-6	

The mass balance provides useful information to quantify water fluxes in the model and relate the SWI dynamics with the submarine groundwater discharge (SGD). Table 5.2 presents the mean values for the complete transient period, thus from 2009 until 2018. The values are estimated per layer and boundary condition. Entering fluxes are positive, while leaving fluxes are negative. Mass fluxes are the sum of water and solutes in liquid phase. The salinity is calculated based on the fluxes of solutes and water in liquid phase.

The mean flux of groundwater discharging to the sea ($0.024 kg/m^2/s$) is coherent with values provided by Cerdà-Domènech et al. (2017) (0.01 - 0.02 $kg/m^2/s$ depending on the method). From this flux only 33% is saltwater. Thus, 33% of SGD is recirculated saline groundwater. Most groundwater discharge to the sea occurs through the top layer. Although large amount of fresh groundwater gets into the system through the layer L6, it does not discharge at that depth. Still, the groundwater discharging through L6 is less saline than through the other layers above and bellow, indicating that part of fresh water is discharging to the sea far away from the seashore.

Temporal patterns of the water fluxes also provide information about the SGD response to different environmental processes (Figure 5.11. During large recharge events, when regional groundwater heads increase, discharge of water can rise up to 0.04 $kg/m^2/s$ (Figure 5.11a). Salinity of the inland and seawards incoming water are constant in time (Figure 5.11b). However, salinity of the discharging groundwater through the seawards boundary show great variations. At the beginning and end of the transient period, when regional groundwater levels are low and incoming freshwater is minimum, discharging groundwater present highers levels of salinity.

5.5.3 Conceptual model of the temperature behaviour at the SWI

Temperature contrast between the fresh and saline groundwater at the SWI can be used to estimate the position of the interface, and also discern the SWI dynamics.

In the tested aquifer, the thermal signature of the fresh water is warmer than that of the saline water. Inland regional circulation (from recharge to discharge zones) is warmer (Figure 5.12A) (Saar, 2011). The first meters of the temperature vertical profile inland reflect the influence of the atmospheric temperature. However, this effect vanished in the around the first 5 to 10 meters depth.

On the other hand, temperature in seawater tends to decrease with depth. This reflects the mean temperature distribution in the sea, which decreases

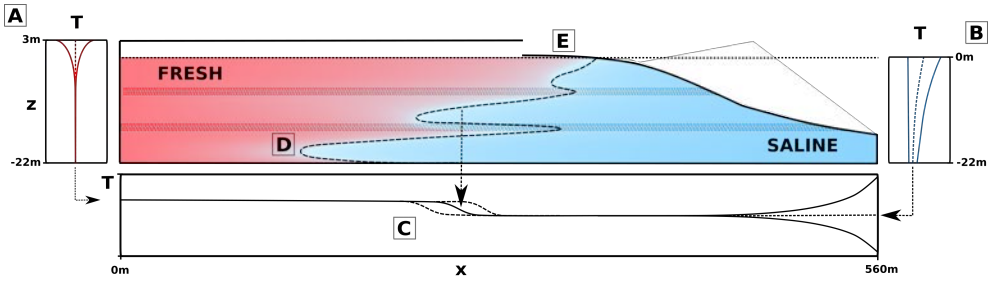

Figure 5.12: Conceptual Model Thermal behaviour of the seawater intrusion. A) Temperature depth profiles inland, showing the annual oscillation in the first meters. B) Temperature depth profile at the sea indicating minimum, maximum and mean annual temperatures. C) Step like temperature distribution in the x axis at the middle of the aquifer where seawater intrusion occurs. D) Contrast between fresh and salt groundwater body can be discerned from the temperature distribution. E) SGD zone.

with depth. During summer temperature of shallow seawater increases, but in winter the whole profiles mixes while getting colder (Guillén et al., 2018) leading on average to a temperature decreasing with depth. Thus, seawater intrusion which is in equilibrium with the annual mean temperature of the sea is colder than fresh inland groundwater. This contrast may vary from latitudes (Figure 5.12B). For example, Vandenbohede, Louw, and Doornenbal (2014) presents the opposite thermal contrast at a shallow sandy aquifer in Belgium. Still, if a thermal contrast is present between the aquifer and the seawater, this should be traceable at the SWI.

Except for the mixing that takes place near the SWI, fresh and saline groundwater remain relatively well unmixed. Recirculating saline groundwater reflects the temperature of the sea, even at large distance from the seashore. This temperature contrast produces a step-like distribution of the temperatures in the x axis (Figure 5.12C). Still, if saline groundwater flux is too small, saline groundwater will tend to have temperatures of the inland fresh groundwater. Thus, the transition between temperatures may occur closer to the sea than the solutes transition.

The thermal signature of the recirculating saline groundwater allows to identify active intrusion through overlapping aquifer levels, in multilayered unconsolidated coastal aquifers (Figure 5.12D). As we shown in the simplified case, and also in the field-scale case, the curved anomalies in the vertical temperature profiles tell us about the direction of groundwater flux and its

rate. In an initial stage we can deduce if there is active intrusion taking place in the aquifer, and at which depth. In a final stage, and for some cases, we may discern the horizontal flow rate. The results from the simplified model and their analytical interpretation indicate that for constant large horizontal groundwater fluxes, groundwater flux can be estimated from the curvature of the temperature vertical profiles. This cannot be done for very small flow rates and pulses of short duration (days).

5.6 Conclusions

The result from the simplified and field-scale models indicate that temperature signature of saline and fresh groundwater bodies can be used to characterize and monitor different features of the SWI. (1) The position of the interface between fresh and saline groundwater can be deduced from the step-like temperature change between both groundwater bodies. (2) In stratified aquifers, with multiple aquifer levels, anomalies in the temperature vertical profiles can be used to discern layers with active intrusion. (3) In some cases, the shape of these anomalies may be used to estimate the horizontal groundwater flux.

The use of temperature as a tracer of the SWI dynamics has certainly several limitations. Solute and temperature fronts do not travel with the same velocities. A retardation factor must be considered, as heat transfer depends not only on the heat capacity of the water but also of the solid matrix. Moreover, heat transport conditions vary greatly when advection or conduction dominates the transport. Therefore, temperature and solutes distribution comparison is neither exact nor straightforward. The flow regime and retardation factor need to be considered to give an estimation of one based on the other.

Despite the mentioned limitations, temperature shows great potential for tracing the SWI dynamics. It may not be able to completely substitute concentrations measurements, but certainly it can bring extremely useful complementary information related to the flow regime. In consequence, new technologies like FO-DTS, able to provide large amounts of data in time and space, represent a great opportunity to study the SWI dynamics.

Future research may concentrate on testing new temperature measurement techniques in order to prove that the thermal patterns simulated by the numerical models actually take place. Moreover, further research is needed in testing the analytical approach to quantify horizontal fluxes in coastal aquifers and clearly define under which assumptions it can be applied. Additionally, a numerical model considering the thermal response to quick processes, such as sea surges or fast recharge events, can be useful. The results from this study

and the number of remained open issues indicates the unexplored potential of the use of temperature as natural tracer to study the SWI.

Chapter 6

Distributed Temperature Sensing for seawater intrusion monitoring

In this chapter we propose to use Fiber Optic Distributed Temperature Sensing (FO-DTS) to monitor the dynamics of the seawater intrusion (SWI). With this technology we hope to bring a new tool that provides the simultaneous high spatial and temporal resolution that traditional field techniques used in coastal hydrogeology lack. To do so, we test the FO-DTS technology at the field scale by monitoring temperature continuously at the SWI during one year and a half. Despite some interruptions in the monitoring due to maintenance problems, the high resolution of the FO-DTS allowed us to identify long and short term dynamics. We first analyse the thermal effects of long term salinization processes. Then we focus on the thermal response of the aquifer to two very different quick meteorological events: a "cold drop" and a storm surge. The results indicate that FO-DTS can be used for monitoring the fresh-salt water interface dynamics, whenever the generated thermal contrast is larger than the temperature resolution of the FO-DTS system. The thermal data produced by the FO-DTS has a great potential for detailed quantitative and qualitative study of coastal aquifers.

6.1 Introduction

Monitoring of coastal aquifers is an outstanding necessity, as large human pressures to coastal fresh groundwater resources and groundwater depend ecosystems increase. Almost half of the worlds population lives within a 100 km from the coast (Martínez et al., 2007; Jiao and Post, 2019), showing a larger growing rate than inland settlements (Neumann et al., 2015; Jiao and Post, 2019). The increasing population implies higher risks of groundwater over-exploitation and pollution derived from the increasing agricultural, touristic and industrial activity. Sea-level rise and the consequent increasing in coastal flooding, is an additional threat to these resources. For this reason, Michael et al. (2017) gave it the very-well-deserved name of "coastal groundwater squeeze". Despite its implications to human wellness, lack of representative data remains one of the main obstacles to improve understanding (Post, 2005; Werner et al., 2013), and therefore management of coastal groundwater resources.

Being able to monitor at great detail the groundwater intrusion wedge is crucial to understand the dynamics of coastal aquifers, which have a great temporal and spatial variability. The dynamics of the seawater interface (SWI) depends on many processes at different temporal (from years to hours) and spatial scales (Land and Paull, 2001; Bravo, Jiang, and Hunt, 2002; Heiss and Michael, 2014). The period of the mean sea oscillations, controls the spatial extent up to which the SWI is displaced (Vallejos, Sola, and Pulido-Bosch, 2014). Furthermore, the position of the SWI depends on the degree of heterogeneity of the aquifer properties (Fahs et al., 2018; Martínez-Pérez et al., 2020). Because coastal aquifers are forced by such a wide variety of phenomenons, we need to generate monitoring methods able to collect large amounts of data. These might help us to capture multi-scale processes.

Additionally, from the perspective of the marine coastal environment, the SWI dynamics control the amount (Taniguchi, Ishitobi, and Shimada, 2006) and quality (Slomp and Van Cappellen, 2004) of the water seeping into the sea. This adds a new dimension to the problem. In fact, much of the recent SWI-related research is done under the scope of the quantification of submarine groundwater discharge (SGD), because of the large implications to coastal ecosystems.

Monitoring of the SWI is usually based on measuring the solutes concentrations. Direct measurements of concentrations can be performed by sampling groundwater from a borehole (Vallejos, Sola, and Pulido-Bosch, 2014; Abarca et al., 2013; Mastrocicco et al., 2012; Petelet-Giraud et al., 2016) or pore-water from sediments (Heiss and Michael, 2014; Taniguchi, Turner, and Smith, 2003). The most commonly used approach is to measure water electrical conductivity

employing electrical conductivity sensors. These sensors are cheap and easy to operate, they offer high temporal resolution, and they can be installed in one or more boreholes. Alternatively, indirect methods, like geophysical methods, are becoming popular in coastal monitoring and characterization, due to their increasing availability and high spatial resolution. Among the most used in coastal areas (Post, 2005), direct current resistivity methods, such as surface Electrical Resistivity Tomography (ERT) (Henderson et al., 2008; Goebel, Pidlisecky, and Knight, 2017; Levi et al., 2008; Franco et al., 2009; Zarroca et al., 2014) or cross-hole ERT (Palacios et al., 2020; Morrow, Ingham, and McConchie, 2010; Nguyen et al., 2009), and electromagnetic methods (EM), such as airborne EM (Delsman et al., 2018). None of these methods provides simultaneously high spatial and temporal resolution. This lack, implies a limitation in the amount and type of process we can observe in coastal aquifers.

Temperature is an alternative to the use of direct or indirect concentration measurements. As discussed in the previous chapter, temperature can be used as a proxy, especially when low frequency oscillations are targeted. However, few field applications employ temperature to trace the intrusion at the field scale. This is surprising, since the potential of temperature as a groundwater tracer has been extensively demonstrated in inland aquifers (Anderson, 2005; Saar, 2011; Domenico and Palciauskas, 1973). One of the most relevant publications in the use of temperature to detect the SWI is Taniguchi (2000). He delineated the position of the SWI by observing the depth to which the vertical temperature gradient deviates from the expected geothermal gradient. However, his research is based on punctual temperature-depth profiles in several boreholes, thus, it does not show proper temporal variability. It seems the use of temperature for this purpose has been very limited, as most of the publications concentrate in the detection and quantification of SGD (Tirado-Conde et al., 2019; Befus et al., 2013; Henderson and Harvey, 2009; Michael, Mulligan, and Harvey, 2005; Land and Paull, 2001). The arrival of the Fiber Optic Distributed Temperature Sensing (FO-DTS) technology to the hydrogeology field, may be an incentive for the use of temperature as a tracer for the SWI dynamics.

FO-DTS provides simultaneously high spatial and temporal resolution measurements, overcoming the limitations of the above mentioned techniques. The FO-DTS is based on the relation between the temperature of a glass fiber and the energy contained in the back-scatter signal generated after shooting a laser through it (Selker et al., 2006). Depending on the manufacturer and model, a Distributed Temperature Sensor (DTS) can have an spatial resolution of up to 25 cm and a sampling interval of less than 10s. The absolute precision of the DTS depends on the accuracy of the calibration, while relative precision

depends on the DTS, being usually around 0.01°C (Selker et al., 2006). Several authors propose the use of FO-DTS to monitor the SGD by just lying the cable on the seeping surface (Hare et al., 2015; Henderson et al., 2008; Sebok et al., 2013), or focusing on the first few meters below surface (Vogt et al., 2010). None of them have used FO-DTS installed vertically in the subsurface with the purpose of detecting the SWI. Installing the cable vertically for several tens of meters below surface, allows to record temperature profiles in depths not affected by the atmospheric temperature conduction. These data may bring information about the dynamics of groundwater at the SWI, before it ex-filtrates in the form of SGD.

We propose to use Fiber Optic Distributed Temperature Sensing (FO-DTS) to monitor the dynamics of the SWI. To do so, we test the FO-DTS technology at the field scale by monitoring temperature continuously at the SWI. With this work, we aim to demonstrate the potential of combining temperature, as a natural tracer, and the FO-DTS, as measuring technique, to monitor the SWI. The combination should bring information about the SWI, at a broad range of temporal scales with high spatial resolution. With this research we hope to expand the coastal hydrogeologist tool box with a new technique to address the monitoring of multi-scale processes.

6.2 Field methods

6.2.1 Experimental site

A combination of traditional and recently developed groundwater monitoring techniques were installed in the Argentona experimental site in NW Spain (Chapter 2). The site is located in the unconsolidated aquifer formed by the fluvio-deltaic deposits of the Argentona catchment. The aquifer is composed by horizontal alternating sand and silt/clay layers, laying on top of a granitic bedrock. This layout creates several semi-confined aquifer levels. The site was equipped with seventeen piezometers screened two meters at different depths in order to capture the SWI (6.1a). Further information about the climatic context, geology and the site construction can be found in Chapter 2, as well as in the recent publications by (Palacios et al., 2020) and Martínez-Pérez et al. (2020). The overall objective of the experimental site was to test different instruments to monitor the SWI dynamics and improve methods for the quantification of the submarine groundwater discharge (Martinez-Perez et al., 2020; Martínez-Pérez et al., 2020).

Evolution of groundwater levels, electrical conductivity and temperature were continuously recorded in each well every 15 min. Conductivity - Temperature - Pressure sensors (CTD) were installed in several boreholes. We employed two different devises: the *3001 LTC Levelogger Junio* from *Solinst (Canada)* and the CTD- DIVER from *Schlumberger water services (USA)*. Only six well were equipped with CTDs, the rest were monitored with MINI-DIVERs (*Schlumberger water services (USA)*), which only offers temperature and pressure data. Each of these devises provides different temperature accuracy and resolution: (1) the *3001 LTC Levelogger Junio* from *Solinst (Canada)* provides an accuracy of $\pm 0.1^{o}$C and a resolution of 0.1^{o}C, (2) CTD- DIVER from *Schlumberger water services (USA)* provides a an accuracy of $\pm 0.1^{o}$C and a resolution of 0.01^{o}C, and (3) the MINI-DIVERs (*Schlumberger water services, USA*) provides a an accuracy of $\pm 0.1^{o}$C and a resolution of 0.01^{o}C.

Additionally, electrical conductivity was measured from groundwater samples. Groundwater sampling was performed eight times between January 2016 and October 2017 at thirteen of the seventeen boreholes.

Periodic Cross-Hole Vertical Electrical Tomography (CHERT) measurements were performed in order to capture spatial patterns of the SWI (Palacios et al., 2020). They found that CHERT decreases the uncertainly of the deeper measurements in comparison with superficial Electric Resistivity Tomography Methods. They performed sixteen measurements from July 2015 to September 2017. The collected data allowed to discern seasonal displacement of the SWI due to a long-term salinization process. We will use these data to discuss the FO-DTS experimental results and propose a conceptual model accordingly.

6.2.2 Permanent system for Fiber Optic Distributed Temperature Sensing

Fiber Optic cable was installed in all wells, and connected to a DTS, which was deployed continuously over a period of one year and a half with several interruptions. Single steel armoured Multi Mode fibre optic cable (*Brugg Kabel AG, Switzerland*) was installed between the PVC cashing and the aquifer materials (6.1b). As explained in Chapter 2, the cable was installed in a "U" shape so that the sticking out extremes of the cable could be connected between wells (6.1c). The glass fusions were done with a *Prolite-40 Fusion Splicer* (*PROMAX, Spain*) and an *EFC-22* fibre optic cutter (*Ericson, Sweden*). The cables of each borehole were connected, avoiding cuts (Chapter 2), forming two separate lines of continuous cable of around 950m long each (6.1a). At the end of the installation, each of them had a total of eight fusions in both directions.

The cable was deployed with an *Oryx +* (*Sensornet, UK*) DTS in a duplexed double ended configuration (6.1c). We decided to choose the double ended calibration (Giesen et al., 2012) over the single ended calibration (Hausner et al., 2011). Double- ended measurements are performed by doing a single-ended measurement through each end of a loop of cable with both ends of the fiber connected to the instrument (Tyler et al., 2009). This calibration method allows to calibrate the differential attenuation in the DTS signal without having to install additional calibration baths. Therefore, we only installed two calibration baths with different temperatures close to the DTS. Their temperature was used as reference to inverse the DTS raw signal into temperatures. The calibration of the DTS signal was performed independently to the calibration embedded in the DTS unit in order to reduce temperature error. To do so we followed the mothodology of Giesen et al. (2012). As explained in Chapter 4, both baths are homogenised with small pumps (*EHEIM Compact 300, EHEIM, Germany*), and monitored with *RBRsolo-T* high resolution temperature loggers (*RBR, Canada*). The warm bath was constructed by submerging at least 10 meters of cable in a 57 l portable cooler (*Igloo, USA*) filled of water kept with a 150W heater (*Sera, Germany*) at an average temperature of 38 °C. The cold bath was constructed with additional 10 m of cable submerged in a 40 l thermoelectric portable cooler (*MOBICOOL International Ltd, Hong Kong*) filled with water kept at an average temperature of 10 °C.

Additionally, a dynamic calibration was performed in order to minimize the effects of the long term operation of the system (Tyler et al., 2009). This approach consist in calibrating the parameters that relate the DTS raw signal to the temperature for each acquisition time, rather than relying in constant calibration parameters for a whole period. This type of calibration is mandatory for long-term FO-DTS applications, where multiple factors might affect the installation performance, and therefore the calibration parameters (Tyler et al., 2009).

The DTS model we employed offers a sampling distance of up to 0.5 m and a minimum integration time or sampling time of 10s. Since the resulting data needs to be averaged for at least two sampling locations, the final spatial resolution is 1m. Given the vertical heterogeneity of the site, we decided to choose the minimum sampling distance. The selection of the integration period is not trivial, as the temperature measurements become more accurate as sampling time increases (Tyler et al., 2009). We decide to set a sampling frequency of 15 min, with an integration time of 2 min. We set four integration periods of 2 min each, one forward and reverse for each fiber optic line, and a resting period of 4 min before the cycle restarts. This resting period is important to let the DTS process and store the data. The 15 min sampling patter allow us

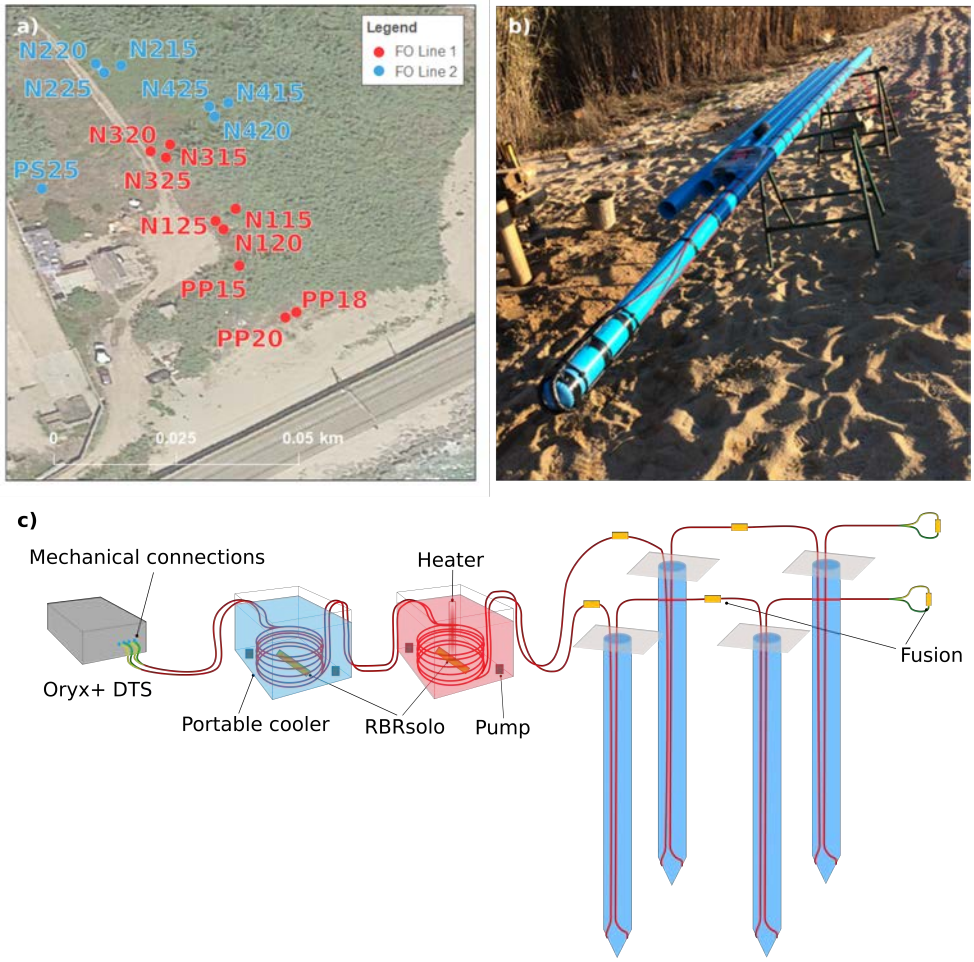

Figure 6.1: Schema depicting the experimental site. a) Map showing the location of all boreholes. In red boreholes which FO cable is interconnected forming line 1. In blue those boreholes forms line 2. b) Picture of the fiber optical cable attached to the PVC tube prior to installation. c) Schema of the FO-DTS installation.

to capture short term dynamics related, for example, to storm surges. 2 min is the maximum integration time that allows us to deploy the cable 4 times, within those 15 min, while maintaining a long enough resting period. The cable was deployed continuously between June 2016 and December 2017.

6.3 Results and discussion

A large temperature data-set was produced from the long term FO-DTS monitoring. Due to its complexity and interest in different aspects, we divide the results in three sections. First, we concentrate in analysing the practical problems arise from the long term operation of a DTS in the field and its accuracy as a monitoring technique. Secondly, we will analyse the long-term dynamics captured with the DTS. And finally, we present and discuss the captured short-term thermal dynamics of the SWI, in response to two very different meteorological events we were able to capture: a "cold drop", and a storm surge.

6.3.1 FO-DTS long-term reliability and accuracy

The permanent FO-DTS installation allowed us to continuously monitor the SWI temperature between June 2016 and December 2017 with a 15 min frequency. Unfortunately, this period was interrupted in several occasions due to different maintenance problems. In fact, long term operation of the DTS system proved to be a complicated task on its own.

We found that the adequate maintenance over a long period of the calibration baths is the most vulnerable piece of the whole process. The calibration baths are used in a double ended calibration to calculate the off-set of the temperatures. Therefore, they are determinant for the accuracy of the calibrated temperature. Therefore, errors might arise or increase when baths are badly maintain. This could be caused by a bad homogenization of the bath water, if the heater or cooler stop working, or if the thermometer monitoring their temperature fail. With our set-up, we succeed in maintaining well homogenized baths with differentiated temperatures over long periods of time. We, however, had problems with the water evaporating from the warm bath. This caused the cable to be partly exposed, thus reducing the length of the cable available for calibration, and inducing larger errors in the calibrated temperature. Moreover, the consumption of the thermometer's batteries for one of the baths did not allow to properly calibrate some sections of the data-set.

In conclusion, and as a consequence of the mentioned shortcomings, from the overall one year and a half only nine periods (2/3 of the total) of continues temperature data are available (Table 6.1). The intervals left out from the analysis represent (1) segments when electricity was not available, and (2) segments of time when one of the two thermometers installed in the calibration

baths was not working. The rest of the data-set was divided in periods of continuous data. Each period was calibrated separately, and the errors reported for each (Table 6.1).

There are several indicators to report the error associated to the temperature calibration. As proposed by (Hausner et al., 2011), the quality of the calibration is here reported through the Root Mean Square Error (RMSE) and Duplexing Error (Edup).

The RMSE, calculated with the calibration baths, is used to report the precision of the calibration process (Hausner et al., 2016). Table 6.1 provides the RMSE values for each calibrated period and duplexed FO line. Since the DTS was deployed through both ends of each FO-line, and because the line was duplexed, we hold four measurements of the same FO cable: Forward-1, Forward-2 (mirror of the F1), Reversed-1 and Reversed-2 (mirror of R1). As it can be observed, RMSE are systematically higher in line 2, than in line 1.

The Edup is calculated as the average of the difference between the duplexed calibrated temperatures. If calibration is properly done, both forward and reverse measurements should bring the same results. This value is meant to be an indication of the calibration consistency. Figure 6.2 presents the Edup for each period and FO-line. The distribution of the medians and the dispersion of the data is consistent between periods and FO-lines. Only the data corresponding to line 2 (indicated as Ch3) in the last three periods (P8, P9 and P10) presents larger dispersion. This increase in the error dispersion is probably also related to the larger MSRE for the same periods and line detailed in Table 6.1.

Duplexed errors are larger around the areas of the cable where high temperature changes is space occur (Hausner et al., 2011). This implies that in areas were large spatial temperature gradients occur, like in the first couple of meter below surface, errors will be large. We decided not to remove this segments from the Edup estimation, which might lead to the large dispersion observed in all the box plots. In any case, the higher dispersion affecting the three last periods of line 2 (P8, P9 and P10), is caused by a signal loss in the mechanical connection between the DTS and the fiber from line 2. This loss in signal increases the noise of the collected data - dispersion - decreasing the resolution of the instrument. Since the mean error of these three does not deviate much from the rest, we will consider these data keeping in mind their large dispersion when discussing the results.

Accuracy of the calibration is also reported by the mean bias of a validation reference section: a section of the cable at known uniform temperature that is not used for calibration (Hausner et al., 2016). Since we do not have an independent validation bath, we compare the calibrated data at the cable

Table 6.1: Double Ended calibration errors per sampling period. (DTS Ch: DTS Channel, RMSE: Root Mean Square Error taking as reference the calibration baths, F1: Forward 1, F2: Forward duplexed, R1: Reversed, R2: Reversed duplexed)

	Period		FO line	RMSE			
	Start	End		F1	F2	R1	R2
P1	10/06/2016	27/06/2016	1	0.04	0.04	0.05	0.04
			2	0.63	0.05	0.68	0.05
P2	30/06/2016	28/07/2016	1	0.05	0.04	0.05	0.04
			2	0.10	0.05	0.08	0.05
P3	28/07/2016	28/09/2016	1	0.04	0.04	0.04	0.04
			2	0.10	0.05	0.08	0.05
P4	22/10/2016	13/12/2016	1	0.05	0.05	0.05	0.05
			2	0.07	0.05	0.06	0.05
P5	14/01/2017	28/02/2017	1	0.04	0.07	0.04	0.07
			2	0.13	0.14	0.25	0.14
P6	28/02/2017	14/03/2017	1	0.05	0.05	0.04	0.05
			2	0.13	0.06	0.10	0.05
P8	19/09/2017	28/09/2017	1	0.04	0.04	0.04	0.04
			2	0.15	0.15	0.10	0.10
P9	28/09/2017	26/10/2017	1	0.04	0.04	0.04	0.04
			2	0.12	0.13	0.10	0.10
P10	26/10/2017	04/12/2017	1	0.05	0.05	0.05	0.05
			2	0.15	0.16	0.10	0.10

locations confronting the screened interval of each well, with the temperature recorder with the installed down-hole sensors. Since the high resolution temperature sensors (*RBRsolo*) are expected to be more reliable than the pressure-temperature sensors, two of these sensors were installed in two wells bellowing to each FO line, during periods 8, 9 and 10. We found that the temperature provided by the pressure sensors and the *RBRsolo* differ in up to 1 C. When both types of sensors are compared to the DTS data, the *RBRsolo* present smaller off-sets than with the pressure sensors (Figure 6.3). Therefore, it seems the DTS provides more accurate temperature measurements than the pressure sensors.

The errors between the temperature measured with the DTS and with the Pressure-Temperature sensors and *RBRsolo* respectively, could be due to

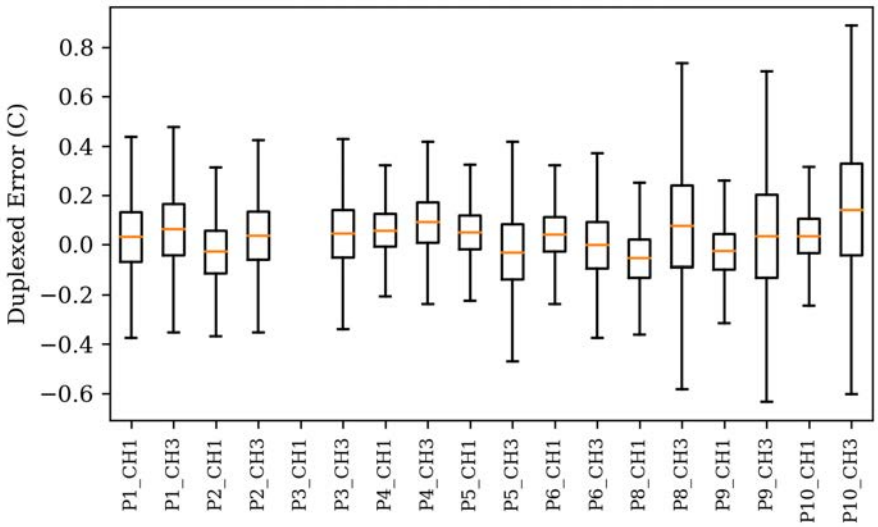

Figure 6.2: Duplexed error for each period and FO line (Table 6.1). Periods are indicated with the letter "P" and the FO lines with the letter "CH" indicating the DTS channel (Line 1 = Ch1 and Line 2 = Ch3)

various reasons. First, while the cable is installed between the PVC cashing and the soil, the sensors are hanging within the borehole space. This might lead to some off-set between both, sensors and DTS data, as discusses in Chapter 2. However, since the *RBRsolo* match quite well with the DTS data, this hypothesis seems unlikely. Another hypothesis could be that the pressure sensors present some drift in time. This can be observed in the slow increase in the error of temperature data from, for example, well N125 in Figure 6.3a. Unfortunately, the only data to validate the temperature obtained from the pressure-temperature sensors is the data obtained from the *RBRsolo*, which is only available for few months. This is not enough to explain the possible error drift in time in the pressure-temperature sensors.

Overall, temperature data recorded with the DTS match well with the high resolution temperature sensors (*RBRsolo*). It seems that the temperature measured with non specific temperature sensors present larger errors and probably some type of drift in time. However, we do not have enough independent data to confirm this hypothesis.

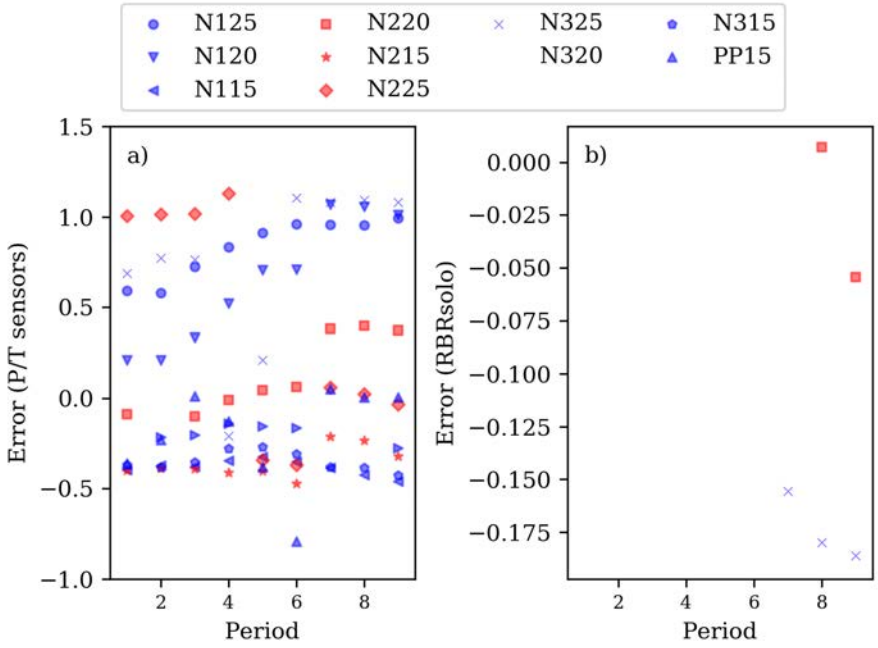

Figure 6.3: Verification DTS data with Pressure-Temperature sensors and *RBRsolo*. a) Mean error between temperature recorded with DTS and with Pressure sensors. b) Mean error between temperature recorded with DTS and with the *RBRsolo* (High precision thermometers). Blue indicates wells from Line 1 and Red indicates wells from line 2.

In conclusion, despite the described issues, the DTS allowed us to collect a large thermal data set on the SWI. Whenever possible, data was properly calibrated, as discussed based on analysis of the different types of calibration errors. Moreover, temperature recorded with the DTS shows good accuracy when compared with independent temperature measurements obtained with high precision thermometers (*RBRsolo*). Finally, we were able to explain the possible reasons behind the increasing error dispersion for some periods, and the lack of agreement between the DTS data and the pressure-temperature sensors. Keeping this issues in mind, the resulting data-set remains a valuable set of information about the thermal dynamics of the SWI we will analyse in the following sections.

6.3.2 Thermal response to hyper-annual fluctuations

Most relevant salinization processes occur in the course of years. In the Mediterranean area inter-annual recharge cycles produce annual recharge rates to vary between a 9 and a 26% Santoni. In response, SWI may move, inducing salinization or refreshing. During our study period there is an increasing in salinity, matching with the occurrence of one of these cycles. Between 2014 and 2017 groundwater levels at the inland well (borehole reference 08029-0094, Agencia Catalana del Agua - ACA) drop more than 0,5 m (data not shown). We monitored part of this hyper-annual trend (between June 2016 until December 2017) in groundwater levels and collected periodic groundwater samples to measure the salinity (Figure 6.4). Salinity indicates a progressive increase in concentrations in the wells opened at the most permeable layer (N120, N320 and N220) . The sustained increasing in salinity is only interrupted by a strong recharge event happening in October 2016. This recharge event produces an increase of groundwater levels in the inland piezometer (red line), and an pause in the increasing salinity trends of piezometers N320 and N220.

It is necessary to mention that the electrical conductivity measured in the field right after taking the sample (Figure 6.4 bottom) does not always compare well with that recorded by the CTDs (data not shown). There are several explanations for this. The most probable one is that, despite the purging of the borehole previous to taking the sample, the water collected is probably a mix of the groundwater quality surrounding the borehole screened interval. Given the length (2m) of the screen interval in comparison with the thickness of some aquifer layers (0.5m), this might affect the water quality of the sample. Still, we discarded the electrical conductivity measured with the CTDs for presenting too much noise and artefacts that could complicate the interpretation.

Several features loom when we observe the temperature changes along the study period (Figure 6.5). The first would be the temperature deviation from the expected geothermal gradient. Theoretical temperature distribution in depth can be estimated using the one-dimensional vertical conductive heat transport analytical solution propose by (Gröber, Erk, and Grigull, 1955; Stauffer et al., 2014). Considering thermal properties of a saturated sand, and an thermal amplitude of 10ºC, the effect of the thermal atmospheric annual oscillation is practically extinguished ($<$ 0.05 ºC) at 15 m depth. At 10 meters depth the effect is around 0.2 ºC. Therefore, below that point the effect of the geothermal gradient should be the dominant process controlling the temperature distribution. In contrast, the temperature profiles recorded in Argentona decrease with depth.

This cooling effect in the areas affected by saline groundwater is to a large

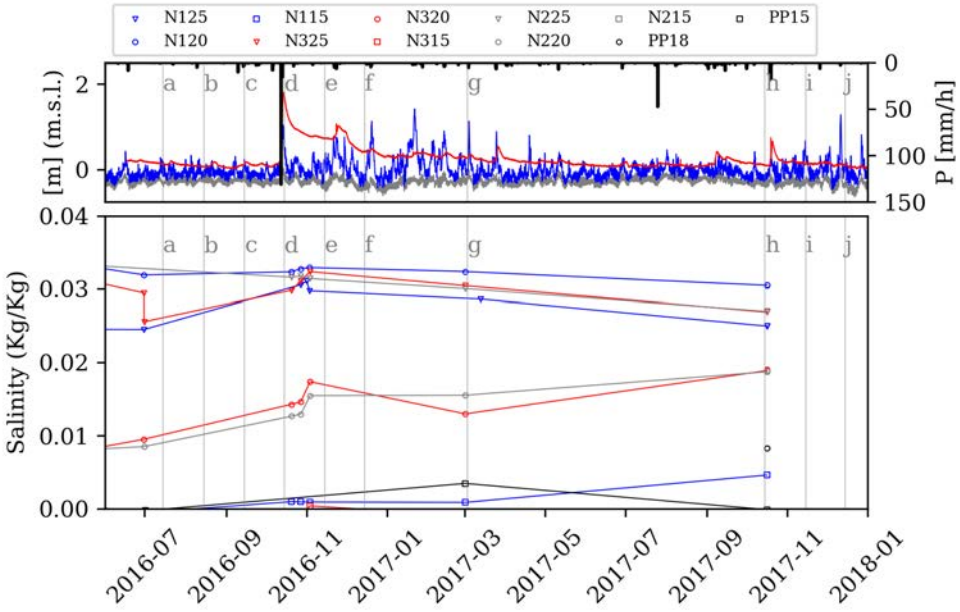

Figure 6.4: Salinity evolution in sampled groundwater. The top plot presents the elevation of the groundwater levels inland (red line), the mean sea level at Mataro port (grey line), the mean sea level including the waves effect (blue line) and the precipitation (black bars). The bottom plot present the salinity in Kg/Kg for several samples of groundwater distributed along the study period. Letters indicate the times of the temperature data showed in Figure 6.5 and 6.6.(Modified from Palacios et al. (2020))

extent what we expected, based on the numerical simulations discussed in the previous chapter. Mean temperature of the sea is lower than that of inland. We know that in general terms, the deeper piezometers are more salinized than the upper ones. Therefore, this decreasing in temperature must be related to the presence of saline groundwater from sea in with a larger or smaller mixing ratio. We well see further in the discussion that the effect of vertical heterogeneity produces anomalies in this increase of solutes and temperature with depth. Domenico and Palciauskas (1973) identify spatial redistribution of heat by moving ground water as one of the mechanisms that could lead to deviations in the geothermal gradient. This observation contradicts the hypothesis of (Taniguchi, 2000), who proposed that below the SWI, thus inside the saline groundwater body, groundwater flow is negligible.

The second feature that stands from these profiles is the change in temperature gradient bellow - 10 m. This is specially noticeable at -15 in well N125, at -15 m in well N325 and at - 17 m in well N225. This input correlates with a high permeable sandy layer located between 10-15 m depth (Chapter 3)(Martínez-Pérez et al., 2020). This layer is believed to behave as a preferential path for seawater intrusion, as observed in the CHERT data (Palacios et al., 2020), which might lead to a larger cooling. In fact, the low temperature anomaly is more prominent at the lower part of the layer (15 m depth), were saline water concentrates due to its higher density.

The identified temperature anomalies in the vertical profile for each piezometer suggest certain horizontal patterns that could be related to the saline distribution. This can be better observed by interpolating the thermal data between piezometers in a 2D vertical cross-section perpendicular to the sea (Figure 6.6). The interpolated profiles acknowledge the occurrence of a colder groundwater body seawards, which contrast with the permanently warmer water inland.

This body of colder groundwater evolves with time. The progressive salinization could be associated to the progressive cooling from the seaside of the profiles. At the same time, this progressive cooling seems to be interrupted by a period with increasing regional groundwater levels, which pushes the SWI seawards. This transient effect can be observed in the vertical profiles of Figure 6.5.

When mean sea levels overcome the groundwater levels, the SWI moves inland. Since the saline groundwater temperature is in equilibrium with the mean temperature of the sea, we shall see a cooling front moving towards inland. This is what we actually see from the numerical simulations presented in Chapter 5. This movement is concentrated at the mentioned permeable layer between -10 and -15 m. Horizontal flow is well known to affect vertical temperature distribution (Lu and Ge, 1996). Ziagos and Blackwell (1986) were able to reconstruct the vertical temperature distribution altered by a preferential path with larger temperature than the surroundings, by considering a horizontal input of warmer groundwater through a permeable layer. The Argentona site would be equivalent but with a cooling effect instead of warming, because of the effect of the sea. Therefore, Argentona thermal distribution is not always dominated by conduction processes or vertical discharge fluxes. On the contrary, horizontal groundwater fluxes through the horizontal permeable layers, control the transient thermal distribution of temperatures.

Additionally, occasional inputs of colder water through the surface are associated to wave over-topping. This can be observed in the first meters below the surface of the interpolated graph of March 2017 data in Figure 6.6. This

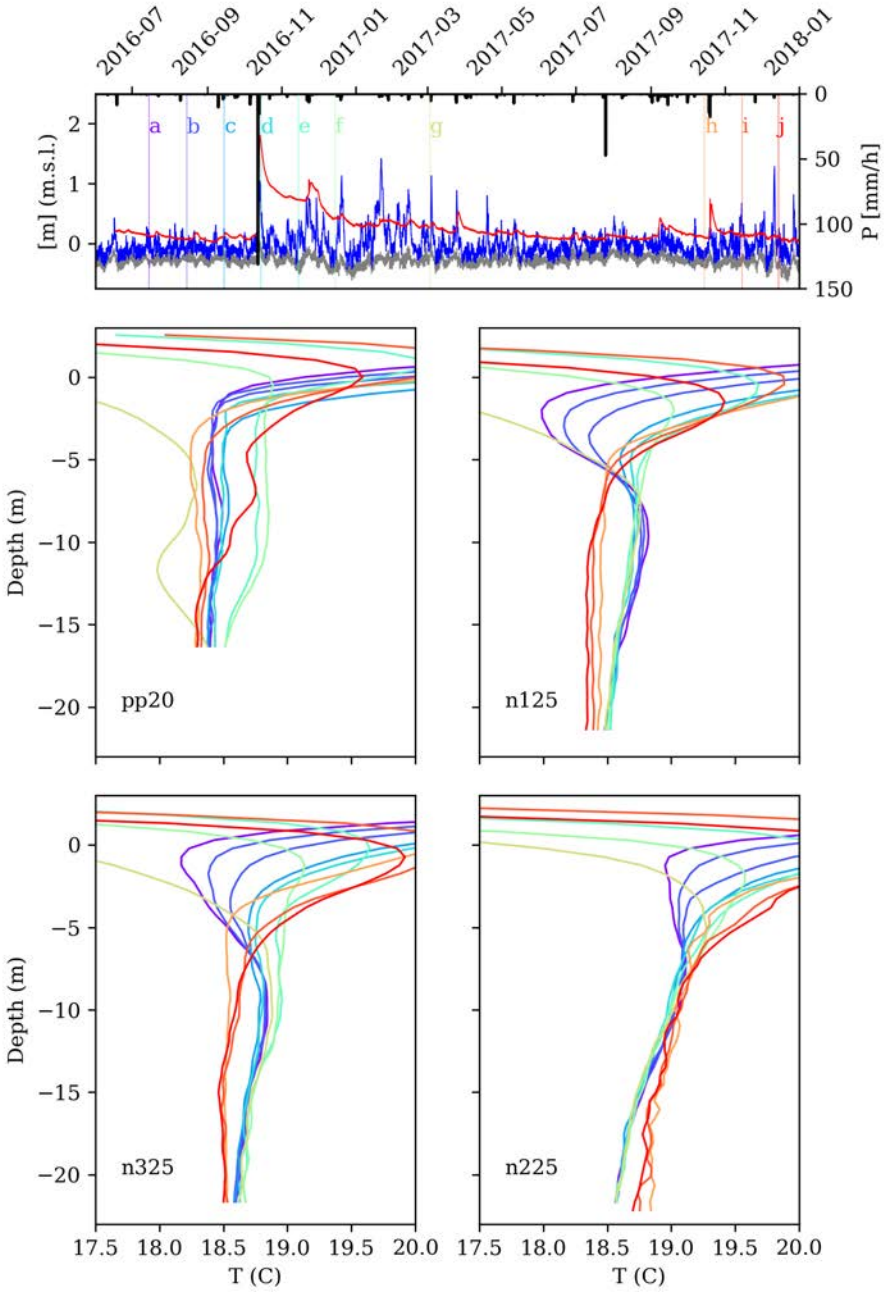

Figure 6.5: DTS profiles evolution along different piezometers DTS profiles evolution

phenomena is also mentioned by Palacios et al. (2020) as a possible explanation for the saline bulb that appears near the surface following periods with high waves in March 2017, what we call sea surge. The transient effects of this phenomena will explained in the following section.

Long term temperature distribution in space and time, correspond to the conceptual model developed in the previous chapter. Thus, temperature seems to be a good proxy of the seawater intrusion, reflecting the general long-term spatial and temporal patterns.

6.3.3 Thermal response to short-term meteorological events

FO-DTS allows to capture rapid meteorological phenomena effects in the SWI. In the Mediterranean coast there are significant rainfall events, called "cold drops", and storm surges. While the first usually take place during Autumn, the second usually take place between September and march. A "cold drops" occurs when a low pressure front with strong winds, push the sea towards the coast, increasing the sea level at the seashore in an unusual way. A storm surge occurs when the low temperatures of the high atmosphere reach areas where high temperatures of the sea are evaporating large quantities of vapour. In these cases, the water condenses rapidly falling in the form of torrential rains, which can cause flash floods. Both short-term meteorological phenomena can have a big impact on the aquifer, inducing large volumes of recharge or seawater intrusion.

Still their rapid occurrence is factor that complicates its monitoring with most of the traditional methods. However, using the permanent FO-DTS monitoring installation, we were able to capture these two different types of events: a storm surge event during Winter 2017 (Figure 6.4g) and an a "cold drop" events in Autumn 2017 (Figure 6.4h).

The storm surge

During the 3^{rd} of March 2017, a large increase in the mean sea level generated a quick pulse that pushed the SWI inland. In Figure 6.4 it can be observed that at the time indicated by the letter "g", mean sea level increases (grey line). Moreover, when wave height effect is added (blue line) the resulting sea level overcomes the groundwater elevation inland (red line). This indicates an inversion of the groundwater gradients towards inland. As can be observed through out the monitored period, there are few moments during the year when this occurs. In this case, there was almost no rain accompanying the event, therefore the reaction of the SWI can be attributed solely to the rising mean sea level at the coast.

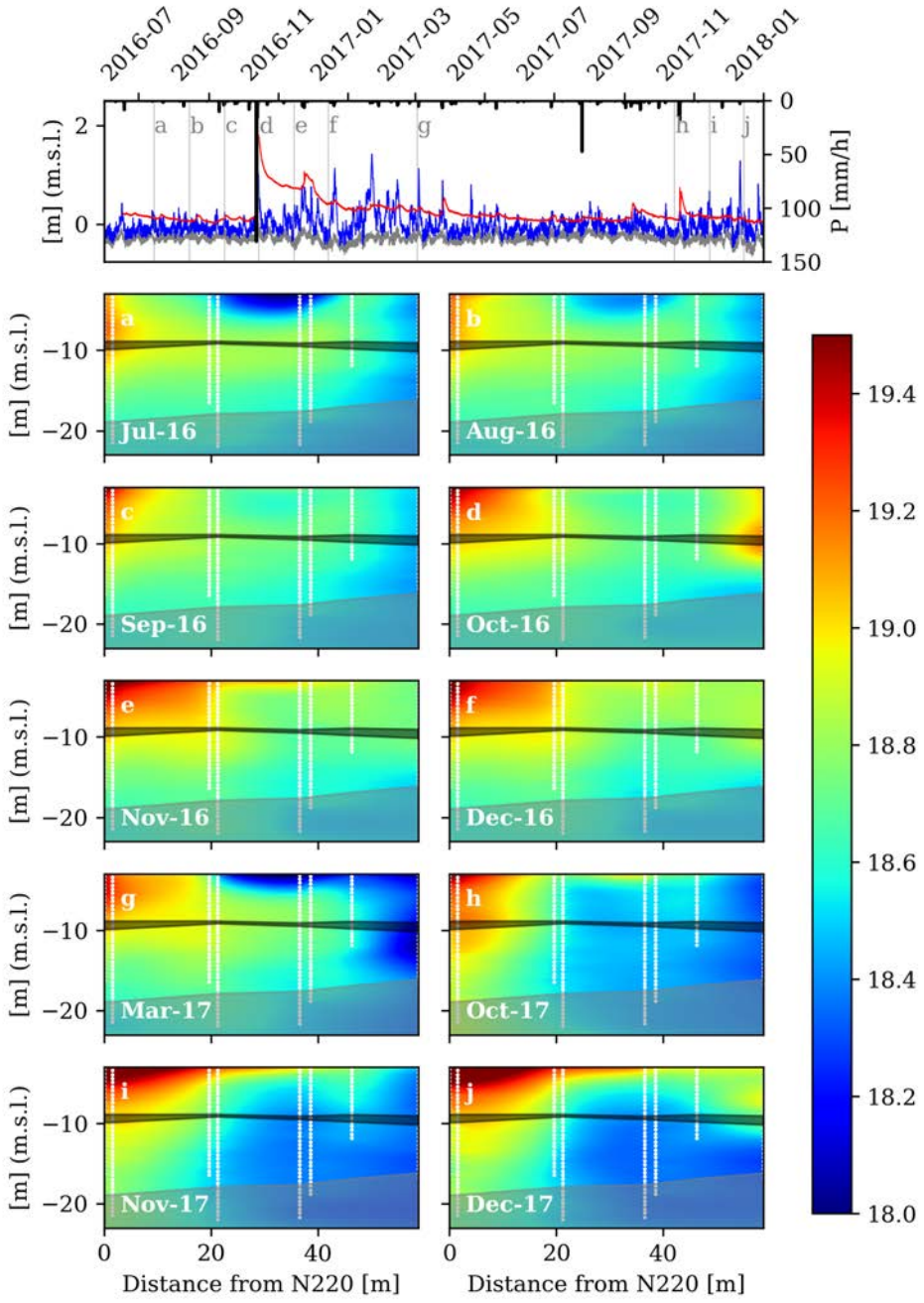

Figure 6.6: Thermal response to inter-annualprocesses

Figure 6.7 shows the hourly averaged temperature data for the period affected by the mentioned storm surge. The increase in the mean sea level is accompanied by a decrease in temperature at 14 m depth and a lowering of the shallow cold front at PP20 well, the closest to the sea. Both processes seem detached. The PP15 which depth only reaches the 15 m, only reflects the vertical movement of the shallow cold front. Additionally, electrical conductivity at the PP20 increases around 0.3 S/cm. The peak of the cooling coincides with the increase in electrical conductivity in the PP20, which reflect both processes are connected.

In light of these data, the storm surge event seems to trigger two parallel processes: (1) the advancing of the SWI front, and (2) the wave overtopping, which may lead to seawater infiltration through the top layer closer to the sea.

The progression of the cold front between -10 and -15 m is coherent with numerical simulations and the CHERT data (Palacios et al., 2020), where salinization, and thus cooling, occurs mainly through the high permeability layer at that depth. It also confirms the hypothesis that at such highly stratified aquifer temperature is controlled by horizontal fluxes rather than vertical ones.

Cooling of the upper 5 m depth matches with the CHERT data for that period recorded by Palacios et al. (2020). The CHERT revealed a salinization of the first 10 meters below surface starting in Winter 2017. This process corresponds to a period when several consecutive high wave events occurred, one of them described here. Therefore, it seems reasonable to expect that the cold water infiltrating through the top is the result of the wave overtopping. This assumption is highlighted by the fact that cooling only occurs in the piezometers closer to the coast line, PP15 and PP20. This process may contribute to the salinization of the aquifer, at least the shallow layers.

The thermal effect of occasional marine inundations is also documented by Vandenbohede and Lebbe (2011). In their case, temperature profiles affected by the saline recharge presented a general increase, as seawater in those latitudes presents higher mean temperature (11.75°C) than that of groundwater (10.2 °C). In our case, the superficial seawater temperature oscillates from a maximum of 30 °C to a minimum of 12,8 °C (data source: Puertos del Estado), while the groundwater at 15 meters depth remains constant at 18.5 °C. If storm surges tend to occur around January, there must be a colder fingerprint affecting the first meters of the inundated boreholes.

The "Cold drop"

During the 10^{th} October 2017, an intense rainfall event ("Cold drop") occurred in the area. This event produced the flooding of the ephemeral stream, which

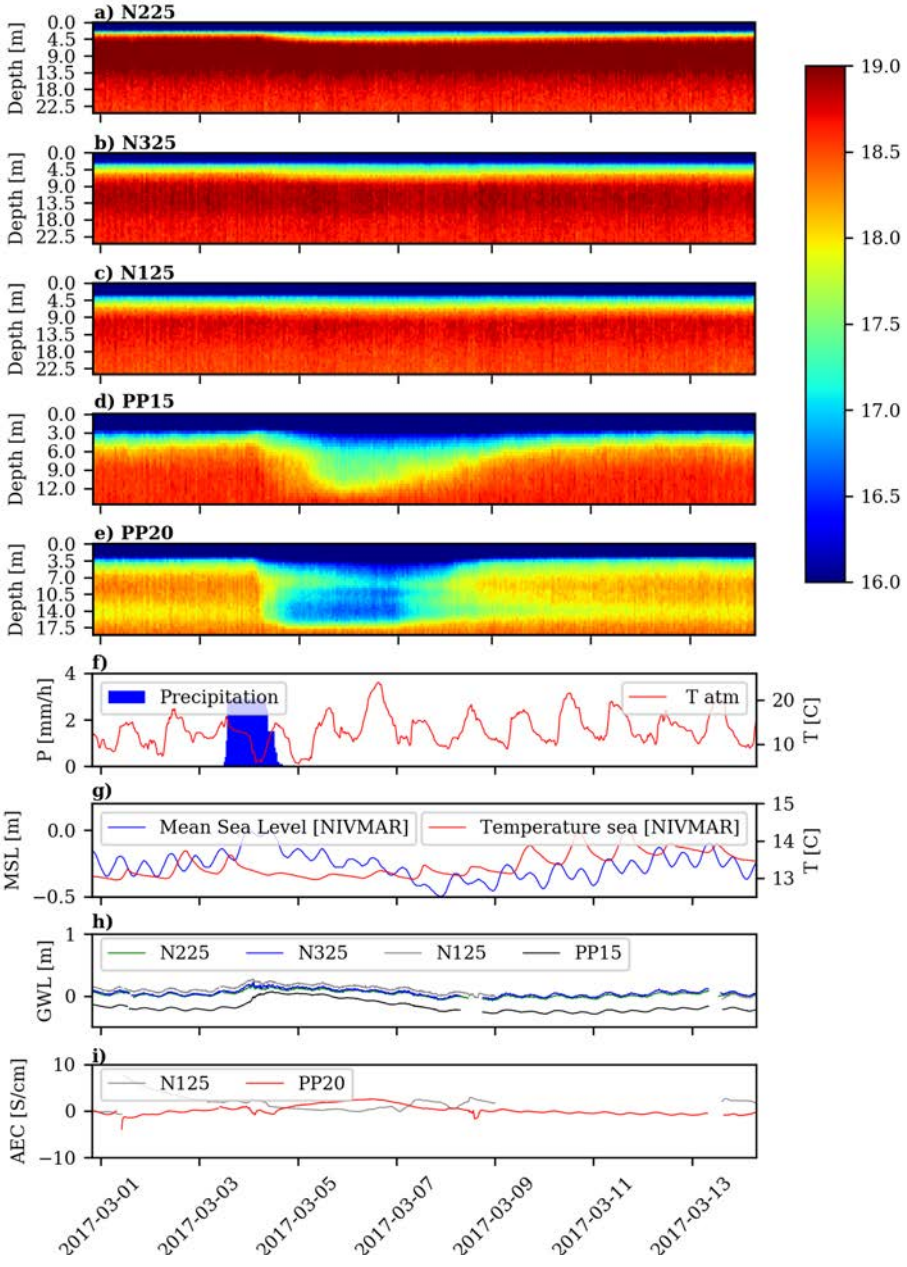

Figure 6.7: Response rainfall event in winter

otherwise remains dry. In Figure 6.4, indicated by the letter "h", we can observe that the rainfall generated a noticeable response of the groundwater levels indicating an intensive regional recharge and local recharge, due to the inundation, which increases the groundwater flux towards the sea. Unlike the storm surge event described above, this intensive recharge was not accompanied by large waves. Therefore, it is expected that the thermal response is mainly related to the intensive recharge and consecutive inundation of the ephemeral stream catchment.

Figure 6.8 shows the response of the temperature in depth and time for the deeper wells. What can be clearly seen in this figure, is the percolation of warmer water through the PP15. The inundation of the research site occurred while we were taking samples. This well remained open as we had to leave the site rapidly. Therefore, surface water percolated inside the well. Refreshing affects the initial response of wells N225 and PP18 (Figure 6.8i). However, after some time, both wells experiment an increase in the electrical conductivity. The causes of such an increase are not clear. An hypotheses could be that while groundwater levels increase in reaction to the recharge, sea level also increase producing a salinization of the deeper levels of the aquifer.

In this interpretation we are overlooking any 3D effect that may be affecting the way the temperature response to these short-term events. The presence of paleo-channels acting as preferential paths, the discontinuity of the identify clay layers, or the mechanical effects of the inundation are some of these potential factors we are not considering and should be evaluated in more detail.

6.4 Conclusions

Our experimental results indicate that temperature recorded with FO-DTS can be used to monitor the fresh-salt water interface dynamics. This technology provides high spatial and temporal resolution that has allowed us to identify not only long trends of the SWI, but also quick reactions to short-term meteorological events. This technology represents a new tool to study the SWI at at a great level of detail, in coastal areas where thermal contrast between fresh and salt groundwater allows so. This study is a good example of the generic advantages, limitations and drawbacks that a coastal hydrogeologist might encounter while using this technology to monitor seawater intrusion.

The DTS proved to provide more accurate measurements than the most commonly used pressure-temperature sensors. However, long term operation of a FO-DTS installation is a complex task. Mistakes in the maintenance of the calibration baths or the connections, may lead to a decrease in the thermal resolution during the calibration process. Still, the data-set produced during

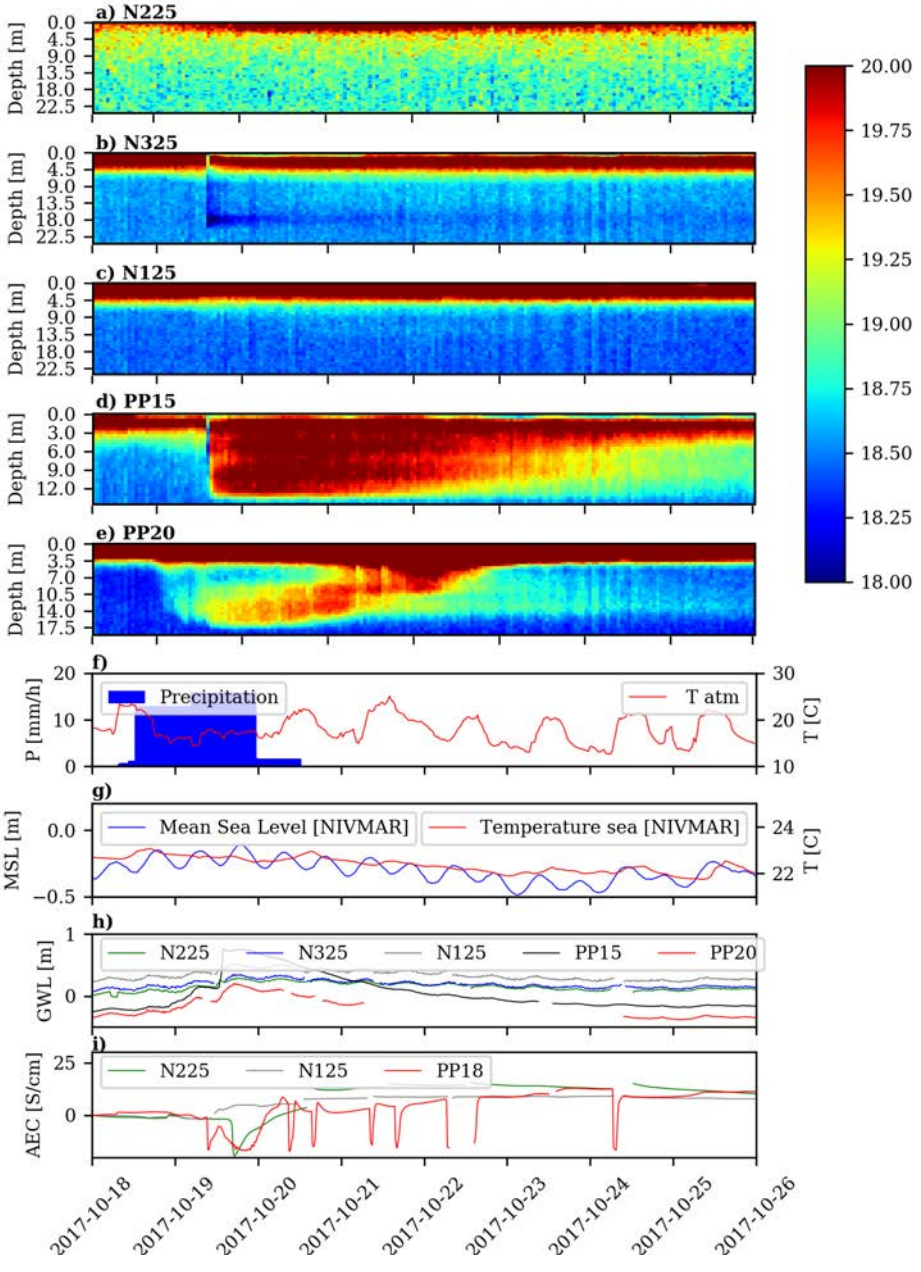

Figure 6.8: Response rainfall event in autumn

the monitoring period allowed us to study the thermal SWI dynamics at great spatial and temporal detail.

Long term dynamics of the interface were detected by the thermal contrast between both salt and fresh groundwater bodies. The thermal data confirms the conceptual model developed in the previous chapter, where saline groundwater presents lower temperatures than inland/fresh groundwater. Moreover, detailed analysis of the thermal profiles for each borehole reveal the predominant strata, in agreement with the available lithological descriptions (Martínez-Pérez et al., 2020)(under review) and geophysical data (Palacios et al., 2020)(in press).

The same installation allowed us to monitor short term dynamics. We found that salt water intrusion events triggered by increasing sea levels during storm surges, produce a thermal plume that can be tracked with the FO-DTS monitoring system. Effects related to the infiltration of saline or fresh water are more uncertain by just looking at the temperature. Still, temperature in those cases might be useful to describe the extent and persistence of the infiltrating water once the origin is known.

FO-DTS can be used for monitoring the fresh-salt water interface dynamics forcing a thermal contrast larger than the temperature resolution allowed by the FO-DTS system. The generated temperature data has a great potential to quantify groundwater fluxes or estimate hydraulic or thermal properties. Therefore, despite the limitations, FO-DTS technology opens a window to observe the SWI at a much greater detail than ever before.

Chapter 7

Conclusions

7.1 Main findings

This thesis aims to provide new approaches to the characterization of the SWI. To achieve this overall objective we built a new research site as part of the MEDISTRAES project (Mixing and DISpersion in the TRAnsport of Energy and Solutes), in which this thesis is framed. Several technologies were tested in the site to characterise in detail the SWI. As part of this work, in this dissertation we propose a new approach to extract drawdowns from measured heads during pumping test in coastal aquifers. We also explored the use of temperature and FO-DTS (Fiber Optics Distributed Temperature Sensing) in characterizing a coastal aquifer. With respect to this, two applications are proposed: first, an active FO-DTS application to measure groundwater fluxes, and second, the use of pasive FO-DTS to monitor the SWI (Seawater Intrusion).

The main findings of each chapter are summarized below:

- In Chapter 2, FO-DTS, CHERT (Cross-Hole Electric Resistivity Tomography) and TLIL (Time Lapse Induction Logging) were tested to characterise the SWI in two different snapshots. The CHERT data allowed for detail characterization of the position of the SWI. FO-DTS data roughly showed the position of the SWI based on the temperature contrast between inland and off-shore groundwater. And the TLIL allowed the identification of preferential flow paths at smaller scale than the other two techniques. The installation of the fiber optic cable outside the borehole casing, together with the CHERT electrodes, allowed to deploy any other tool inside the well. The combination of all three permitted the characterisation at various spatial scales, and discern possible dynamics.

- In Chapter 3, we used a new approach to remove natural head fluctuations and noise from a coastal aquifer pumping test data, so that

drawdowns could be extracted to ease interpretation. The quality of the trend and noise removal process was validated by comparing the pumping and recovery drawdowns and simulating the test with a numerical model. The interpretation of the resulting drawdown allowed to deduce a conceptual flow model and estimate hydraulic parameters, which are coherent with the existing hydrogeological knowledge about the site.

- In Chapter 4, we proposed a method to directly measure groundwater fluxes by heating a fiber optic cable and interpreting analytically the resulting heating curve. The groundwater fluxes could only be estimated at few points where temperature increase reached steady state. The measured flow rates were in agreement with independent estimates. However, further research would be needed to account for effects of the cable materials, cable set-up and aquifer heterogeneity.

- In Chapter 5, we discussed the use of temperature as a tracer for detecting SWI dynamics. To study coupled heat and solute transport at the SWI with two simplified numerical models at different scales. From these, we concluded that temperature can be used to characterise the position of the SWI, wherever there is a thermal contrast between the inland groundwater and the saline groundwater. Moreover, the anomalies in the vertical temperature profiles can be used to detect layers with active intrusion. In some cases, the shape of the anomaly can be related to the groundwater flux. Still, the connection between temperature and solute distribution is not straightforward.

- In Chapter 6, FO-DTS measurements obtained during a year and a half of measurements at the research site were analyzed. SWI dynamics at different time scales were identified through the temperature data. Long-term salinization at the most permeable layer could be identified which correlates with CHERT data. Short-term oscillations due to quick meteorological events (heavy rain events and sea surge) were also identified. The results provide a first insight into the potential of FO-DTS for coastal aquifer monitoring and confirm the theoretical framework we started to built in the previous chapter.

7.2 Overall conclusions

Along this document we have stated in several occasions that the lack of knowledge about the SWI dynamics is one of the most relevant obstacles towards

proper management of coastal aquifers. Several conclusions can be drawn from the results of this thesis to alleviate this problem.

Traditional methods may require a thoughtful review, in order to improve their applicability and reliability in coastal aquifers. This was the case we faced with the interpretation of the pumping test we performed in our research site. Pumping tests are widely used by hydrogeologist. Still their interpretation under complicated circumstances, like the ones we faced in Argentona, is not fully established. The same may happen with other techniques that we think completely established without giving it a second thought. Uncertainty in most used field techniques and methods may also hamper our study of the SWI.

Classic approaches, like the use of piezometers and downhole electrodes, could be extended by deploying several tools in the same piezometer. This multipurpose approach was used in our field site, providing simultaneous complementary data with a relatively small investment.

Other well-known approaches, like the use of temperature as a tracer, remain relatively unexplored in the coastal aquifers context. Although temperature is measured systematically by most down-hole sensors and its theory is well established, its used in coastal hydrogeology is limited, or at least has not been used to its full potential as we saw during this dissertation. We used natural and induce thermal contrast to obtain valuable information about the SWI and the properties of the aquifer. The use of temperature on its own, or better, in combination with traditional solutes-based techniques, may improve again our knowledge about the SWI dynamics, and thus about the SGD. In fact, interesting results about the SWI response to long-term and short-term events were obtained by monitoring temperature. Following this reasoning, the study of the SGD? may benefit from the use of other alternative or complementary magnitudes, like we think it does with temperature.

We tested recently developed technologies that can be used to chracterize costal aquiers and probe their potential for characterizing the SWI dynamics, which is one of the key knowledge gaps. During our research, we studied the use of FO-DTS, which has been used for many fields in hydrogeology, but not for coastal aquifers. Although, many questions remain unanswered, FO-DTS may be an alternative technology to increase the amount of spatial and temporal data about the SWI. The increase in data may broaden our view on the SWI, particularly those related to the transient processes. And this will contribute to improve our knowledge about its controlling factors.

Overall, this thesis provides some new methods for aquifer characterization, and in special for SWI characterization. Moreover, it provides detailed data about dynamics of a real case of SWI. And finally, it provides several conclusion about the thermal behaviour of coastal aquifers, which contribute to the general

knowledge about groundwater behaviour in coastal zones. But above all, it raises many questions, and highlights the necessity for further research on coastal hydrogeology.

7.3 Future research

Based on the thesis results, it is clear that further research is needed to improve characterization of coastal aquifers, in particular SWI dynamics. Traditional field methods need to be revised based on the new knowledge we have gained about the SWI, recent methods need to be improved and new ones need to be tested.

Rethinking of traditional field methods, like pumping tests, used in coastal hydrogeology may be a topic for interesting research. In relation to the interpretation of coastal aquifer pumping test data, advanced data processing tools like artificial neural networks, may be explored to ease processing of complex head data. Moreover, the monitoring of pumping test with new technology may provide complementary information to the classical measurement of groundwater levels.

FO-DTS is a recent technology that is becoming intensively researched and used in hydrogeology. Still, many questions remain unanswered about its reliability, accuracy, installation and operation in the field. Active FO-DTS has a great potential for groundwater flux quantification. Still, we found that the design of the heating, the installation of the cable or how to way to treat effects of the cable materials in the interpretation, are issues that need more researchh before this method can become a standard. Seamlessly, passive FO-DTS long term operating is difficult, so it is to treat properly the data.So, new ways to facilitate the implementation of this technology needs to be explored.

The use of FO-DTS is connected to the use of temperature as a tracer. We found temperature being underused in coastal aquifer applications, and especially in SWI monitoring. Further understanding of the connections between the solutes and heat transport at these environments may trigger the use of temperature as a tracer for coastal aquifer processes, allowing better understanding of the different processes (dynamics, geochemistry,etc) taking place in coastal aquifers. Physical and numerical models could be made for this purpose.

Finally, constantly new monitoring devices appear on the market. This is especially true in the fiber optics industry. Fiber Bragg gratings, distributed acoustic sensing, fiber optic chemical sensors or distributed measurement of magnetic fields, are some of the newest fiber optic sensors that are starting to be applied in environmental monitoring. It is therefore up to us to explore the

potential of all these new technologies to improve the knowledge on coastal aquifers.

Appendix A

Supplementary material Chapter 2

Table A.1: Groundwater electrical conductivities and temperatures measured in the 2 m screened interval of each piezometer except PP12 and PP15 that are completely screened.

Piezometers	**Electrical Conductivity (mS/cm)**		**Temperature (C)**	
	(16/06/2015)	**(10/09/2015)**	**(26/06/2015)**	**(10/09/2015)**
N115	1.60-2.16	1.56-2.08	19.02-19.70	18.97
N120	43.0-52.0	42.20-43.22	19.50-18.99	18.86
N125	39.6-44.4	35.09-35.72	18.91-18.84	18.79
N215	1.10-1.15	0.82-10.17	19.75-19.61	21.3-21.2
N220	8.45-14.06	12.30-21.7	19.47-19.37	20.4-20.4
N225	30.06-32.42	-	19.01-18.98	-
N315	1.64-1.72	1.45-1.46	19.14-19.19	10.29-11.29
N320	13.33-19.66	25.83-26.30	19.18-17.92	19.60-19.50
N325	36.34-41.81	38.99-39.55	19.1-19.03	19.03-19.98
PP20	8.07-45.33	8.60-39.17	20.11-18.87	23.2-19.6
PP15	2.24-3.11	2.24-2.78	19.3-19.07	18.8-18.9

Appendix B

Derivation of the analytical solution for the ideal case

The solution of Equation 4.1 for a unit heat pulse input is

$$T_1(x,y,t) = \frac{1}{2\pi C_b \sigma_x \sigma_y} \exp\left[-\frac{1}{2}\left(\left(\frac{x-v_T t}{\sigma_x}\right)^2 + \left(\frac{y}{\sigma_y}\right)^2\right)\right] \tag{B.1}$$

where $\sigma_x = \sqrt{2D_{TL}t/C_b}$, $\sigma_y = \sqrt{2D_{TT}t/C_b}$, and $v_T = q_x C_w/C_b$. This equation can be somewhat simplified by defining $t_{cd} = C_b(x^2/D_{TL} + y^2/D_{TT})$ and $x_c = 2D_{TL}/C_b v_T$

$$T_1(x,y,t) = \frac{1}{4\pi\sqrt{D_{TL}D_{TT}t}} e^{\frac{x}{x_c}} \exp\left[-\frac{1}{4}\left(\frac{t_{cD}}{t} + \frac{C_b v_T^2 t}{D_{TL}}\right)\right] \tag{B.2}$$

The solution for a continuous energy source can be obtained by convolution, which yields

$$T = \frac{P}{4\pi\sqrt{D_{TL}D_{TT}}} e^{\frac{x}{x_c}} \int_0^t \frac{1}{\tau} \exp\left[-\frac{1}{4}\left(\frac{t_{cD}}{\tau} + \frac{2v_T\tau}{x_c}\right)\right] d\tau \tag{B.3}$$

We transform variables by choosing $s = t_{cD}/4\tau$, so that $d\tau/\tau = -ds/s$. With this transformation, Equation B.3 becomes:

$$T = \frac{P}{4\pi\sqrt{D_{TL}D_{TT}}} e^{\frac{x}{x_c}} \int_\infty^{t_{cD}/4t} \frac{1}{s} \exp\left[-s - \frac{v_T t_{cD}}{8x_c s}\right] ds \tag{B.4}$$

Exchanging the integral limits, we get:

$$T = \frac{P}{4\pi\sqrt{D_{TL}D_{TT}}} e^{\frac{x}{x_c}} W_H\left(\frac{t_{cD}}{4t}, \sqrt{\frac{v_T t_{cD}}{2x_c}}\right) \tag{B.5}$$

Where is known in well hydraulics literature Hantush and Jacob (1955) well function, defined as:

$$W_H(a,b) = \int_a^\infty \frac{1}{s} \exp\left[-s - \frac{b^2}{4s}\right] ds \tag{B.6}$$

The log-derivative of T is

$$\frac{dT}{dlnt} = \frac{P}{\pi\sqrt{D_{TL}D_{TT}}} e^{\frac{x}{x_c}} \frac{t}{t_{cD}} \exp\left[-\frac{t_{cD}}{4t} - \frac{v_t t}{2x_c}\right] \tag{B.7}$$

Or, assuming dispersivities to be zero

$$T(x,y,t) = \frac{P}{4\pi\lambda} e^{\frac{q_x C_w x}{2\lambda}} W_H(u,v) \tag{B.8a}$$

$$u = \frac{C_b r^2}{4\lambda t} \tag{B.8b}$$

$$v = \frac{q_x C_w r}{2\lambda} \tag{B.8c}$$

Appendix C

Parabolic distribution of temperatures under horizontal constant flow rate

Equation 5.6 shows the temporal evolution of the temperature in porous media. Neglecting dispersion gives:

$$C_b \frac{\partial T}{\partial t} = \nabla \cdot (\lambda \nabla T) - \nabla \cdot (C_w T \mathbf{q}) \tag{C.1}$$

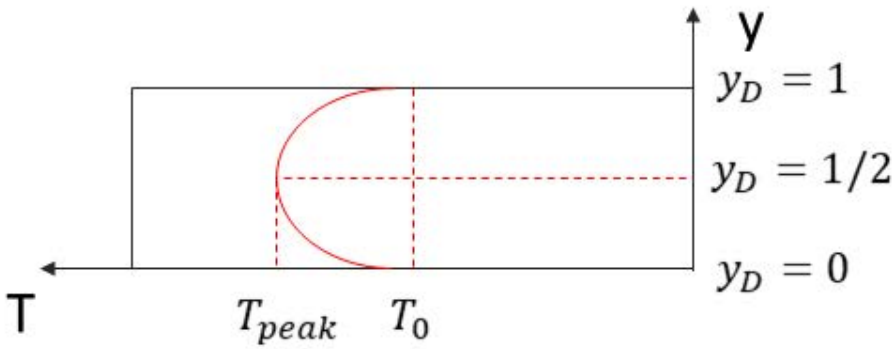

Figure C.1: Schematic of parabolic distribution of temperatures under horizontal constant flow rate

For isotropic conditions for the thermal conductivity (λ), 2D domain and steady state this equation can be written as:

$$\frac{\partial^2 T}{\partial x^2}\frac{\lambda}{C_w} + \frac{\partial^2 T}{\partial y^2}\frac{\lambda}{C_w} - \mathbf{q}\frac{\partial T}{\partial x} = 0 \tag{C.2}$$

If we assume that the temperature varies linearly along the x-axis ($\frac{\partial^2 T}{\partial x^2} = 0$) and we introduce the dimensionless variables $x_D = \frac{x}{L_x}$ and $y_D = \frac{y}{L_y}$ (where L_x and L_y represent the characteristic lengths of the problem), we obtain the following partial differential equation representing the vertical parabolic shape of the temperature:

$$\frac{\partial^2 T}{\partial y_D^2} = \frac{qC_w L_y^2}{\lambda L_x}\frac{\partial T}{\partial x_D} \tag{C.3}$$

Since $\frac{\partial T}{\partial x_D}$ and q are assumed constant, $\frac{\partial^2 T}{\partial y^2}$ is constant as well, and the above expression can be directly integrated by setting the following boundary conditions:

$$T(y_D = 0) = T(y_D = L_y) = T_0 \tag{C.4}$$

where T_0 is the background temperature. Therefore, the vertical distribution of the temperature is given by:

$$T(y_D) = \frac{1}{2}y_D^2\left(\frac{qC_w L_y^2}{L_x\lambda}\frac{\partial T}{\partial x_D}\right) - \frac{1}{2}y_D\left(\frac{qC_w L_y^2}{L_x\lambda}\frac{\partial T}{\partial x_D}\right) + T_0 \tag{C.5}$$

Considering that $T(y_D = 1/2) = Tpeak$ (Figure C.1, we can calculate q as:

$$q = \frac{8(Tpeak - T_0)L_x\lambda}{\frac{\partial T}{\partial x_D}L_y^2 C_w} \tag{C.6}$$

Bibliography

Abarca, Elena et al. (2013). "Transient groundwater dynamics in a coastal aquifer: The effects of tides, the lunar cycle, and the beach profile". In: *Water Resources Research* 49.5, pp. 2473–2488. ISSN: 00431397. DOI: 10.1002/wrcr.20075.

Agarwal, Ram G. (2004). "A new method to account for producing time effects when drawdown type curves are used to analyze pressure buildup and other test data". In: *SPE Reprint Series* 57 PART 1, pp. 93–112. ISSN: 08910901. DOI: 10.2523/9289-ms.

Agencia Catalana de L'Aigua (2009). "Maresme 18. Fitxa de Caracterització, análisis de pressions, impactes i análisis del risc d'incompliment". In: *Fitxes de Caracterització inicial, pressions i Impactes de les Masses d'Aigua Subterrànies (IMPRESS, 2004)*. Barcelona. Chap. 18. URL: http://aca-web.gencat.cat/aca/appmanager/aca/aca?{_}nfpb=true{\&}{_}pageLabel=P25400181961268046736218{\&}{_}nfls=false.

Alcolea, Andrés et al. (2007). "Inverse modeling of coastal aquifers using tidal response and hydraulic tests". In: *Ground Water* 45.6, pp. 711–722. ISSN: 0017467X. DOI: 10.1111/j.1745-6584.2007.00356.x.

Alcolea, Andrés et al. (2019). "Science of the Total Environment Hydrogeological modelling for the watershed management of the Mar Menor coastal lagoon (Spain)". In: *Science of the Total Environment* 663, pp. 901–914. ISSN: 0048-9697. DOI: 10.1016/j.scitotenv.2019.01.375. URL: https://doi.org/10.1016/j.scitotenv.2019.01.375.

Almeida, C. and J. J. L. Mendonça (2017). "Pumping test analysis in confined aquifers subjected to tidal fluctuations". In: *Journal of Clinical Investigation* 104.1, pp. 1846–1857. ISSN: 0873-948X. URL: http://www.lneg.pt/iedt/unidades/16/paginas/26/30/90.

Amaranto, A. et al. (2019). "A Spatially Enhanced Data-Driven Multimodel to Improve Semiseasonal Groundwater Forecasts in the High Plains Aquifer, USA". In: *Water Resources Research* 55.7, pp. 5941–5961. ISSN: 19447973. DOI: 10.1029/2018WR024301.

Andersen, Martin Søgaard et al. (2005). "Geochemical processes and solute transport at the seawater/freshwater interface of a sandy aquifer". In: *Geochimica et Cosmochimica Acta* 69.16, pp. 3979–3994. ISSN: 00167037. DOI: 10.1016/j.gca.2005.03.017. URL: http://www.sciencedirect.com/science/article/pii/S0016703705002516.

Anderson, Mary P. (2005). "Heat as a ground water tracer". In: *Ground Water* 43.6, pp. 951–968. ISSN: 0017467X. DOI: 10.1111/j.1745-6584.2005.00052.x.

Anwar, N., C. Robinson, and D.A. Barry (2014). "Influence of tides and waves on the fate of nutrients in a nearshore aquifer: Numerical simulations". In: *Advances in Water Resources* 73, pp. 203–213. ISSN: 03091708. DOI: 10.1016/j.advwatres.2014.08.015. URL: http://www.sciencedirect.com/science/article/pii/S0309170814001821https://linkinghub.elsevier.com/retrieve/pii/S0309170814001821.

Badaruddin, Sugiarto, Adrian D. Werner, and Leanne K. Morgan (2015). "Water table salinization due to seawater intrusion". In: *Water Resources Research* 51.10, pp. 8397–8408. ISSN: 0043-1397. DOI: 10.1002/2015WR017098. URL: https://onlinelibrary.wiley.com/doi/abs/10.1002/2015WR017098.

Bakker, Mark et al. (2015). "An active heat tracer experiment to determine groundwater velocities using fiber optic cables installed with direct push equipment". In: *Water Resources Research*, pp. 2760–2772. DOI: 10.1002/2014WR016632.Received.

Bandos, T. V. et al. (2011). "Improving parameter estimates obtained from thermal response tests: Effect of ambient air temperature variations". In: *Geothermics* 40.2, pp. 136–143. ISSN: 03756505. DOI: 10.1016/j.geothermics.2011.02.003. URL: http://dx.doi.org/10.1016/j.geothermics.2011.02.003.

Banks, Eddie W., Margaret a. Shanafield, and Peter G. Cook (2014). "Induced Temperature Gradients to Examine Groundwater Flowpaths in Open Boreholes". In: *Groundwater* 52.6, pp. 943–951. ISSN: 17456584. DOI: 10.1111/gwat.12157.

Barker, J A (1988). *A Generalized Radial Flow Model for Hydraulic Tests in Fractured Rock*. Tech. rep. 10, pp. 1796–1804.

Beaujean, J. et al. (2014). "Calibration of seawater intrusion models: Inverse parameter estimation using surface electrical resistivity tomography and borehole data". In: *Water Resources Research* 50.8, pp. 6828–6849. ISSN: 00431397. DOI: 10.1002/2013WR014020. URL: http://doi.wiley.com/10.1002/2013WR014020.

Becker, Matthew W, Brian Bauer, and Adam Hutchinson (2013). "Measuring Artificial Recharge with Fiber Optic Distributed Temperature Sensing". In: 51.5, pp. 670–678. DOI: 10.1111/j.1745-6584.2012.01006.x.

Befus, Kevin M. et al. (2013). "Heat transport dynamics at a sandy intertidal zone". In: *Water Resources Research* 49.6, pp. 3770–3786. ISSN: 00431397. DOI: 10.1002/wrcr.20325.

Bellmunt, F. et al. (2016). "Capability of cross-hole electrical configurations for monitoring rapid plume migration experiments". In: *Journal of Applied Geophysics* 124, pp. 73–82. ISSN: 09269851. DOI: 10.1016/j.jappgeo.2015.11.010.

Bense, V. F. et al. (2016). "Distributed Temperature Sensing as a downhole tool in hydrogeology". In: *Water Resources Research* 52.12, pp. 9259–9273. ISSN: 19447973. DOI: 10.1002/2016WR018869. arXiv: 2014WR016527 [10.1002].

Bense, Victor F. et al. (2017). "Interpreting Repeated Temperature-Depth Profiles for Groundwater Flow". In: *Water Resources Research* 53.10, pp. 8639–8647. ISSN: 19447973. DOI: 10.1002/2017WR021496.

Bone, Sharon E. et al. (2007). "Has submarine groundwater discharge been overlooked as a source of mercury to coastal waters?" In: *Environmental Science and Technology* 41.9, pp. 3090–3095. ISSN: 0013936X. DOI: 10.1021/es0622453.

Boulton, NS (1954). "Unsteady radial flow to a pumped well allowing for delayed yield from storage". In: *International Association of Scientific Hydrology* 37, pp. 472–477. URL: http://hydrologie.org/redbooks/a037/037048.pdf.

Bourdet, D. et al. (1983). "New Set of Type Curves Simplifies Well Test Analysis." In: *World Oil* 196.6, pp. 1–7. ISSN: 00438790.

Bravo, Hector R., Feng Jiang, and Randall J. Hunt (2002). "Using groundwater temperature data to constrain parameter estimation in a groundwater flow model of a wetland system". In: *Water Resources Research* 38.8, pp. 28–1–28–14. ISSN: 0043-1397. DOI: 10.1029/2000wr000172.

Bredehoeft, J. D. and I. S. Papaopulos (1965). "Rates of vertical groundwater movement estimated from the Earth's thermal profile". In: *Water Resources Research* 1.2, pp. 325–328. ISSN: 19447973. DOI: 10.1029/WR001i002p00325.

Briggs, Martin A. et al. (2016). "Actively heated high-resolution fiber-optic-distributed temperature sensing to quantify streambed flow dynamics in zones of strong groundwater upwelling". In: *Water Resources Research* 52.7, pp. 5179–5194. ISSN: 00431397. DOI: 10.1002/2015WR018219. URL: http://doi.wiley.com/10.1002/2015WR018219.

Brovelli, A., X. Mao, and D. A. Barry (2007). "Numerical modeling of tidal influence on density-dependent contaminant transport". In: *Water Resources Research* 43.10, pp. 1–15. ISSN: 00431397. DOI: 10.1029/2006WR005173.

Calvache, M. L. et al. (2015). "Evaluation of analytical methods to study aquifer properties with pumping tests in coastal aquifers with numerical modelling (Motril-salobreña aquifer)". In: *Water Resources Management* 30.2, pp. 559–575. ISSN: 15731650. DOI: 10.1007/s11269-015-1177-6.

Camporese, M. et al. (2011). "Assessment of local hydraulic properties from electrical resistivity tomography monitoring of a three-dimensional synthetic tracer test experiment". In: *Water Resources Research* 47.12, pp. 1–15. ISSN: 00431397. DOI: 10.1029/2011WR010528.

Carrera, Jesus and Shlomo P Neuman (1986). "Estimation of Aquifer Parameters Under Transient and Steady State Conditions: 3. Application to Synthetic and Field Data". In: *Water Resources Research* 22.2, pp. 228–242. ISSN: 19447973. DOI: 10.1029/WR022i002p00199.

Carslaw, H.S. and J.C. Jaeger (1959). *Conduction of heat in soils*. Second. Great Britain: Oxford University Press.

Cassiani, Giorgio et al. (2006). "A saline trace test monitored via time-lapse surface electrical resistivity tomography". In: *Journal of Applied Geophysics* 59.3, pp. 244–259. ISSN: 09269851. DOI: 10.1016/j.jappgeo.2005.10.007.

Cerdà-Domènech, Marc et al. (2017). "Constraining the temporal variations of Ra isotopes and Rn in the groundwater end-member: Implications for derived SGD estimates". In: *Science of the Total Environment* 595, pp. 849–857. ISSN: 18791026. DOI: 10.1016/j.scitotenv.2017.03.005.

Chapuis, Robert P., Christian Bélanger, and Djaouida Chenaf (2006). "Pumping test in a confined aquifer under tidal influence". In: *Ground Water* 44.2, pp. 300–305. ISSN: 0017467X. DOI: 10.1111/j.1745-6584.2005.00139.x.

Cho, Hyung Mi et al. (2018). "Radium tracing nutrient inputs through submarine groundwater discharge in the global ocean". In: *Scientific Reports* 8.1, pp. 4–10. ISSN: 20452322. DOI: 10.1038/s41598-018-20806-2. URL: http://dx.doi.org/10.1038/s41598-018-20806-2.

Coleman, Thomas I. et al. (2015). "Groundwater flow characterization in a fractured bedrock aquifer using active DTS tests in sealed boreholes". In: *Journal of Hydrology* 528, pp. 449–462. ISSN: 00221694. DOI: 10.1016/j.jhydrol.2015.06.061. URL: http://dx.doi.org/10.1016/j.jhydrol.2015.06.061.

Cooper, H. H. and C. E. Jacob (1946). "A generalized graphical method for evaluating formation constants and summarizing well???field history". In: *Eos, Transactions American Geophysical Union* 27.4, pp. 526–534. ISSN: 23249250. DOI: 10.1029/TR027i004p00526.

Coppola, Emery A. et al. (2005). "A neural network model for predicting aquifer water level elevations". In: *Ground Water* 43.2, pp. 231–241. ISSN: 0017467X. DOI: 10.1111/j.1745-6584.2005.0003.x.

Council of the European Union (2009). *Protocol on integrated Coastal Zone Management in the Mediterranean*. URL: http://data.europa.eu/eli/prot/2009/89/oj.

Custodio, Emilio (2017). *Salinización de las aguas subterráneas en los acuíferos costeros mediterráneos e insulares españoles*. Barcelona, pp. 1–852. ISBN: 9788498806878.

Dale, Ryan K. and Douglas C. Miller (2007). "Spatial and temporal patterns of salinity and temperature at an intertidal groundwater seep". In: *Estuarine, Coastal and Shelf Science* 72.1-2, pp. 283–298. ISSN: 02727714. DOI: 10.1016/j.ecss.2006.10.024.

Davis, S. N. et al. (1985). *Ground-water traces*. Worthington, Ohio: National Water Well Association, p. 200.

Debnath, Palash et al. (2015). "Delineating seasonal porewater displacement on a tidal flat in the Bay of Bengal by thermal signature: Implications for submarine groundwater discharge". In: *Journal of Hydrology* 529, pp. 1185–1197. ISSN: 00221694. DOI: 10.1016/j.jhydrol.2015.09.029. URL: http://dx.doi.org/10.1016/j.jhydrol.2015.09.029.

Delsman, Joost R. et al. (2018). "Large-scale, probabilistic salinity mapping using airborne electromagnetics for groundwater management in Zeeland, the Netherlands". In: *Environmental Research Letters* 13.8. ISSN: 17489326. DOI: 10.1088/1748-9326/aad19e.

Denchik, Nataliya et al. (2014). "Near-surface CO2 leak detection monitoring from downhole electrical resistivity at the CO2 Field Laboratory, Svelvik Ridge (Norway)". In: *International Journal of Greenhouse Gas Control* 28, pp. 275–282. ISSN: 17505836. DOI: 10.1016/j.ijggc.2014.06.033.

Domenico, Patrick A. and VV Palciauskas (1973). "Theoretical Analysis of Forced Convective Heat Transfer in Regional Ground-Water Flow". In: *Geological Society of America Bulletin* 84.December, pp. 3803–3814. ISSN: 0016-7606. DOI: 10.1130/0016-7606(1973)84<3803:TAOFCH>2.0.CO;2.

Dror, Ishai et al. (2003). "Salt-pump mechanism for contaminant intrusion into coastal aquifers". In: *Science* 300.5621, p. 950. ISSN: 00368075. DOI: 10.1126/science.1080075.

Drost, Walter et al. (1968). "Point dilution methods of investigating ground water flow by means of radioisotopes". In: *Water Resources Research* 4.1, pp. 125–146. ISSN: 19447973. DOI: 10.1029/WR004i001p00125.

Duque, Carlos et al. (2016). "Estimating groundwater discharge to surface waters using heat as a tracer in low flux environments: The role of thermal

conductivity". In: *Hydrological Processes* 30.3, pp. 383–395. ISSN: 10991085. DOI: 10.1002/hyp.10568.

Fahs, Marwan et al. (2018). "A Generalized semi-analytical solution for the dispersive Henry problem: Effect of stratification and anisotropy on seawater intrusion". In: *Water (Switzerland)* 10.2. ISSN: 20734441. DOI: 10.3390/w10020230.

Feng, Qinggao and Hongbin Zhan (2016). "Integrated aquitard-aquifer flow with a mixed-type well-face boundary and skin effect". In: *Advances in Water Resources* 89, pp. 42–52. ISSN: 03091708. DOI: 10.1016/j.advwatres.2016.01.003. URL: http://dx.doi.org/10.1016/j.advwatres.2016.01.003.

Ferroud, Anouck, Silvain Rafini, and Romain Chesnaux (2019). "Using flow dimension sequences to interpret non-uniform aquifers with constant-rate pumping-tests: A review". In: *Journal of Hydrology X* 2, p. 100003. ISSN: 25899155. DOI: 10.1016/j.hydroa.2018.100003. URL: https://doi.org/10.1016/j.hydroa.2018.100003.

Fidelibus, Maria Dolores and Antonio Pulido-Bosch (2019). "Groundwater temperature as an indicator of the vulnerability of Karst coastal aquifers". In: *Geosciences (Switzerland)* 9.1, pp. 1–22. ISSN: 20763263. DOI: 10.3390/geosciences9010023.

Folch, Albert et al. (2020). "Combining Fiber Optic (FO-DTS), Cros Hole ERT and time lapse formation electrical conductivity to characterize and monitor a coastal aquifer". In: *Journal of Hydrology*. DOI: (Underreview).

Forster, C. and L. Smith (1989). "The influence of groundwater flow on thermal regimes in mountainous terrain: a model study". In: *Journal of Geophysical Research* 94.B7, pp. 9439–9451. ISSN: 01480227. DOI: 10.1029/JB094iB07p09439.

Franco, R. de et al. (2009). "Monitoring the saltwater intrusion by time lapse electrical resistivity tomography: The Chioggia test site (Venice Lagoon, Italy)". In: *Journal of Applied Geophysics* 69.3-4, pp. 117–130. ISSN: 09269851. DOI: 10.1016/j.jappgeo.2009.08.004. URL: http://dx.doi.org/10.1016/j.jappgeo.2009.08.004.

Freifeld, B. M. et al. (2008). "Ground surface temperature reconstructions: Using in situ estimates for thermal conductivity acquired with a fiber-optic distributed thermal perturbation sensor". In: *Geophysical Research Letters* 35.14, pp. 3–7. ISSN: 00948276. DOI: 10.1029/2008GL034762.

Garing, C. et al. (2013). "Geochemical investigations of saltwater intrusion into the coastal carbonate aquifer of Mallorca, Spain". In: *Applied Geochemistry* 39, pp. 1–10. ISSN: 08832927. DOI: 10.1016/j.apgeochem.2013.09.011. URL: http://dx.doi.org/10.1016/j.apgeochem.2013.09.011.

Giambastiani, Beatrice M.S. et al. (2017). "Coastal aquifer response to extreme storm events in Emilia-Romagna, Italy". In: *Hydrological Processes* 31.8, pp. 1613–1621. ISSN: 10991085. DOI: 10.1002/hyp.11130.

Giesen, Nick van de et al. (2012). "Double-ended calibration of fiber-optic raman spectra distributed temperature sensing data". In: *Sensors (Switzerland)* 12.5, pp. 5471–5485. ISSN: 14248220. DOI: 10.3390/s120505471.

Goebel, Meredith, Adam Pidlisecky, and Rosemary Knight (2017). "Resistivity imaging reveals complex pattern of saltwater intrusion along Monterey coast". In: *Journal of Hydrology* 551, pp. 746–755. ISSN: 00221694. DOI: 10.1016/j.jhydrol.2017.02.037. URL: http://dx.doi.org/10.1016/j.jhydrol.2017.02.037.

Green, Timothy R. et al. (2011). "Beneath the surface of global change: Impacts of climate change on groundwater". In: *Journal of Hydrology* 405.3-4, pp. 532–560. ISSN: 00221694. DOI: 10.1016/j.jhydrol.2011.05.002. URL: http://www.sciencedirect.com/science/article/pii/S0022169411002988.

Gröber, H., S. Erk, and U. Grigull (1955). *Grundgesetze der Wärmeübertragung*. rev. Berlin: Springer.

Guillén, Jorge et al. (2018). "Coastal oceanographic signatures of heat waves and extreme events of dense water formation during the period 2002-2012 (Barcelona, NW Mediterranean)". In: *Scientia Marina* 82.4, pp. 189–206. ISSN: 18868134. DOI: 10.3989/scimar.04766.26A.

Günther, Thomas, Carsten Rücker, and Klaus Spitzer (2006). "Three-dimensional modelling and inversion of dc resistivity data incorporating topography - II. Inversion". In: *Geophysical Journal International* 166.2, pp. 506–517. ISSN: 0956540X. DOI: 10.1111/j.1365-246X.2006.03011.x.

Halford, Keith J. (2006). "Documentation of a Spreadsheet for Time-Series Analysis and Drawdown Estimation". In: *Scientific Investigations Report* 2006-5024, pp. 1–38.

Halford, Keith J et al. (2012). "Advanced methods for modeling water-levels and estimating drawdowns with SeriesSEE, an Excel add-in". In: *Techniques and Methods* July, p. 42. DOI: 10.3133/tm4F4. URL: http://pubs.er.usgs.gov/publication/tm4F4.

Hantush, M. S. (1956). "Analysis of data from pumping test in leaky aquifers". In: *J. Geophys. Res.* 64.6, pp. 1043–1052.

Hantush, M. S. and C. E. Jacob (1955). "Non-steady radial flow in an infinite leaky aquifer". In: *Eos, Transactions American Geophysical Union* 36.1, pp. 95–100. ISSN: 23249250. DOI: 10.1029/TR036i001p00095.

Hare, Danielle K. et al. (2015). "A comparison of thermal infrared to fiber-optic distributed temperature sensing for evaluation of groundwater discharge to

surface water". In: *Journal of Hydrology* 530, pp. 153–166. ISSN: 00221694. DOI: 10.1016/j.jhydrol.2015.09.059. URL: http://dx.doi.org/10.1016/j.jhydrol.2015.09.059.

Hausner, Mark B. et al. (2011). "Calibrating single-ended fiber-optic raman spectra distributed temperature sensing data". In: *Sensors* 11.11, pp. 10859–10879. ISSN: 14248220. DOI: 10.3390/s111110859.

Hausner, Mark B et al. (2016). "Interpreting Variations in Groundwater Flows from Repeated Distributed Thermal Perturbation Tests". In: *Groundwater* 54.4, pp. 559–568. ISSN: 0017467X. DOI: 10.1111/gwat.12393. URL: http://doi.wiley.com/10.1111/gwat.12393.

Heiss, James W. and Holly A. Michael (2014). "Saltwater-freshwatermixing dynamics in a sandy beach aquifer over tidal, spring-neap, and seasonal cycles". In: *Water Resour. Res* 51, pp. 341–358. ISSN: 00431397. DOI: 10.1002/2013WR014979.Reply. arXiv: 2014WR016527 [10.1002].

Henderson, R D and C F Harvey (2009). "Investigation of aquifer-estuary interaction using wavelet analysis of fiber-optic temperature data". In: 36.December 2008, pp. 1–6. DOI: 10.1029/2008GL036926.

Henderson, Rory D et al. (2008). "Characterizing Submarine Ground-Water Discharge Using Fiber-Optic Distributed Temperature Sensing and Marine Electrical Resistivity". In: *Sageep* 4, pp. 1–11. DOI: 10.4133/1.2963319.

Henderson, Rory D. et al. (2010). "Marine electrical resistivity imaging of submarine groundwater discharge: sensitivity analysis and application in Waquoit Bay, Massachusetts, USA". In: *Hydrogeology Journal* 18.1, pp. 173–185. ISSN: 1431-2174. DOI: 10.1007/s10040-009-0498-z. URL: http://links.isiglobalnet2.com/gateway/Gateway.cgi?GWVersion=2{\&}SrcAuth=mekentosj{\&}SrcApp=Papers{\&}DestLinkType=FullRecord{\&}DestApp=WOS{\&}KeyUT=000273479600013{\%}5Cnpapers2://publication/doi/10.1007/s10040-009-0498-zhttp://link.springer.com/10.1007/s10040-009-049.

Henry, H.R. and J.B. Hilleke (1972). *Exploration of multiphase fluid flow in a saline aquifer system affected by geothermal heating. (Final report)*. Tech. rep. Alabama Univ., University (USA). DOI: DI-14-08-0001-12681.

Hidalgo, Juan J., Jesús Carrera, and Marco Dentz (2009). "Steady state heat transport in 3D heterogeneous porous media". In: *Advances in Water Resources* 32.8, pp. 1206–1212. ISSN: 03091708. DOI: 10.1016/j.advwatres.2009.04.003. URL: http://dx.doi.org/10.1016/j.advwatres.2009.04.003.

Huizer, S. et al. (2017). "Monitoring and simulation of salinity changes in response to tide and storm surges in a sandy coastal aquifer system". In:

Water Resources Research 53.8, pp. 6487–6509. ISSN: 19447973. DOI: 10.1002/2016WR020339.

IOC-UNESCO and UNEP (2016). "Large Marine Ecosystems: Status and Trends". In: *Transboundary Waters Assessment Programme*. Vol. 4. Nairobi: United Nations Environment Programme (UNEP). ISBN: 9782831711577. DOI: 10.1126/science.299-a.

Irvine, Dylan J. et al. (2017). "Groundwater flow estimation using temperature-depth profiles in a complex environment and a changing climate". In: *Science of the Total Environment* 574, pp. 272–281. ISSN: 18791026. DOI: 10.1016/j.scitotenv.2016.08.212. URL: http://dx.doi.org/10.1016/j.scitotenv.2016.08.212.

Jaaskelainen, Mikko (2010). "Temperature monitoring of geothermal energy wells". In: *Fourth European Workshop on Optical Fibre Sensors*. ISBN: 9780819480835. DOI: 10.1117/12.868156.

Jamin, P. et al. (2015). "Contribution of the finite volume point dilution method for measurement of groundwater fluxes in a fractured aquifer". In: *Journal of Contaminant Hydrology* 182, pp. 244–255. ISSN: 18736009. DOI: 10.1016/j.jconhyd.2015.09.002. URL: http://dx.doi.org/10.1016/j.jconhyd.2015.09.002.

Jiao, Jimmy and Vincent Post (2019). *Coastal Hydrogeology*. I. Cambridge University Press. ISBN: 9781139344142. DOI: https://doi.org/10.1017/9781139344142.

Keery, John et al. (2007). "Temporal and spatial variability of groundwater-surface water fluxes: Development and application of an analytical method using temperature time series". In: *Journal of Hydrology* 336.1-2, pp. 1–16. ISSN: 00221694. DOI: 10.1016/j.jhydrol.2006.12.003.

Kim, Guebuem, Jong Sun Kim, and Dong Woon Hwang (2011). "Submarine groundwater discharge from oceanic islands standing in oligotrophic oceans: Implications for global biological production and organic carbon fluxes". In: *Limnology and Oceanography* 56.2, pp. 673–682. ISSN: 00243590. DOI: 10.4319/lo.2011.56.2.0673.

Kim, Kue-Young, Chul-Min Chon, and Ki-Hwa Park (2007). "A simple method for locating the fresh water-salt water interface using pressure data." In: *Ground water* 45.6, pp. 723–8. ISSN: 0017-467X. DOI: 10.1111/j.1745-6584.2007.00349.x. URL: http://www.ncbi.nlm.nih.gov/pubmed/17973750.

Klepikova, Maria V. et al. (2011). "A methodology for using borehole temperature-depth profiles under ambient, single and cross-borehole pumping conditions

to estimate fracture hydraulic properties". In: *Journal of Hydrology* 407.1-4, pp. 145–152. ISSN: 00221694. DOI: 10.1016/j.jhydrol.2011.07.018. URL: http://dx.doi.org/10.1016/j.jhydrol.2011.07.018.

Klepikova, Maria V. et al. (2014). "Passive temperature tomography experiments to characterize transmissivity and connectivity of preferential flow paths in fractured media". In: *Journal of Hydrology* 512, pp. 549–562. ISSN: 00221694. DOI: 10.1016/j.jhydrol.2014.03.018. URL: http://dx.doi.org/10.1016/j.jhydrol.2014.03.018.

Koestel, Johannes et al. (2008). "Quantitative imaging of solute transport in an unsaturated and undisturbed soil monolith with 3-D ERT and TDR". In: *Water Resources Research* 44.12, pp. 1–17. ISSN: 00431397. DOI: 10.1029/2007WR006755.

Konikow, Leonard F. and Eloise Kendy (2005). "Groundwater depletion: A global problem". In: *Hydrogeology Journal* 13.1, pp. 317–320. ISSN: 14312174. DOI: 10.1007/s10040-004-0411-8.

Kruseman, G.P., N.A. de Ridder, and J.M. Verweij (1994). *Analysis and Evaluation of Pumping Test Data*. 2nd ed. Wageningen: International Institute for Land Reclamation and Improvement. ISBN: 9070754207.

Kue-Young et al. (2008). "Multi-depth monitoring of electrical conductivity and temperature of groundwater at a multilayered coastal aquifer: Jeju Island, Korea". In: *HYDROLOGICAL PROCESSES* 2274.November 2008, pp. 2267–2274. ISSN: 08856087. DOI: 10.1002/hyp. URL: http://jamsb.austms.org.au/courses/CSC2408/semester3/resources/ldp/abs-guide.pdf.

Land, Lewis A. and Charles K. Paull (2001). "Thermal gradients as a tool for estimating groundwater advective rates in a coastal estuary: White Oak River, North Carolina, USA". In: *Journal of Hydrology* 248.1-4, pp. 198–215. ISSN: 00221694. DOI: 10.1016/S0022-1694(01)00405-X.

Langevin, Christian D., Alyssa M. Dausman, and Michael C. Sukop (2010). "Solute and heat transport model of the Henry and Hilleke laboratory experiment". In: *Ground Water* 48.5, pp. 757–770. ISSN: 0017467X. DOI: 10.1111/j.1745-6584.2009.00596.x.

Levi, Eldad et al. (2008). "Spatial delineation of groundwater salinity using deep time domain electromagnetic geophysical measurements: A feasibility study". In: *Water Resources Research* 44.12, pp. 1–14. ISSN: 00431397. DOI: 10.1029/2007WR006459. URL: http://doi.wiley.com/10.1029/2007WR006459.

Li, Shaoheng et al. (2019). "Vertical groundwater flux estimation from borehole temperature profiles by a numerical model, RFLUX". In: *Hydrological Processes* 33.11, pp. 1542–1552. ISSN: 10991085. DOI: 10.1002/hyp.13420.

Liu, G., S. Knobbe, and J. J. Butler (2013). "Resolving centimeter-scale flows in aquifers and their hydrostratigraphic controls". In: *Geophysical Research Letters* 40.6, pp. 1098–1103. ISSN: 00948276. DOI: 10.1002/grl.50282.

Lu, Ning and Shemin Ge (1996). "Effect of horizontal heat and fluid flow on the vertical temperature distribution in a semiconfining layer". In: *Water Resources Research* 32.5, pp. 1449–1453. ISSN: 00431397. DOI: 10.1029/95WR03095.

Mamer, Ethan A and Christopher S Lowry (2013). "Locating and quantifying spatially distributed groundwater / surface water interactions using temperature signals with paired fiber-optic cables". In: 49, pp. 7670–7680. DOI: 10.1002/2013WR014235.

Martínez, M. L. et al. (2007). "The coasts of our world: Ecological, economic and social importance". In: *Ecological Economics* 63.2-3, pp. 254–272. ISSN: 09218009. DOI: 10.1016/j.ecolecon.2006.10.022.

Martínez-Pérez, Laura et al. (2020). "Conceptual and methodological surprises in the characterization of the Mediterranean coastal aquifer of Argentona". In: *HESS*. DOI: (Underreview).

Martinez-Perez, Laura et al. (2020). "Questioning the traditional paradigm for seawater intrusion: evidence from salinity profiles". In: *Journal of Hydrology*. DOI: (Underreview).

Mastrocicco, M. et al. (2012). "The Importance of Data Acquisition Techniques in Saltwater Intrusion Monitoring". In: *Water Resources Management* 26.10, pp. 2851–2866. ISSN: 09204741. DOI: 10.1007/s11269-012-0052-y.

McDaniel, Adam et al. (2018). "Long-term district-scale geothermal exchange borefield monitoring with fiber optic distributed temperature sensing". In: *Geothermics* 72.September 2017, pp. 193–204. ISSN: 03756505. DOI: 10.1016/j.geothermics.2017.11.008. URL: https://doi.org/10.1016/j.geothermics.2017.11.008.

Medina, A. and J. Carrera (1996). "Coupled estimation of flow and solute transport parameters". In: *Water Resources Research* 32.10, pp. 3063–3076. ISSN: 00431397. DOI: 10.1029/96WR00754.

Medina, Agustín and Jesús Carrera (2003). "Geostatistical inversion of coupled problems: Dealing with computational burden and different types of data". In: *Journal of Hydrology* 281.4, pp. 251–264. ISSN: 00221694. DOI: 10.1016/S0022-1694(03)00190-2.

Meier, Peter M, Jesús Carrera, and Xavier Sánchez-Vila (1998). "An evaluation of Jacob's method for the interpretation of pumping tests in heterogeneous formations". In: *Water Resources Research* 34.5, pp. 1011–1025. ISSN: 00431397. DOI: 10.1029/98WR00008.

Michael, Holly A., Ann E. Mulligan, and Charles F. Harvey (2005). "Seasonal oscillations in water exchange between aquifers and the coastal ocean". In: *Nature* 436.7054, pp. 1145–1148. ISSN: 00280836. DOI: 10.1038/nature03935.

Michael, Holly A et al. (2017). "Science, society, and the coastal groundwater squeeze". In: *Water Resources Research* 53.4, pp. 2610–2617. ISSN: 00431397. DOI: 10.1002/2017WR020851.

Moore, Willard S (1999). "The subterranean estuary: a reaction zone of ground water and sea water". In: *Marine Chemistry* 65.1-2, pp. 111–125. ISSN: 03044203. DOI: 10.1016/S0304-4203(99)00014-6. URL: http://www.sciencedirect.com/science/article/pii/S0304420399000146https://linkinghub.elsevier.com/retrieve/pii/S0304420399000146.

Moore, Willard S. (2010). "The Effect of Submarine Groundwater Discharge on the Ocean". In: *Annual Review of Marine Science* 2.1, pp. 59–88. ISSN: 1941-1405. DOI: 10.1146/annurev-marine-120308-081019.

Morrow, F. J., M. R. Ingham, and J. A. McConchie (2010). "Monitoring of tidal influences on the saline interface using resistivity traversing and cross-borehole resistivity tomography". In: *Journal of Hydrology* 389.1-2, pp. 69–77. ISSN: 00221694. DOI: 10.1016/j.jhydrol.2010.05.022. URL: http://dx.doi.org/10.1016/j.jhydrol.2010.05.022.

Muller, Kerstin et al. (2010). "Imaging and characterization of solute transport during two tracer tests in a shallow aquifer using electrical resistivity tomography and multilevel groundwater samplers". In: *Water Resources Research* 46.3, pp. 1–23. ISSN: 00431397. DOI: 10.1029/2008WR007595.

Neuman, Shlomo P. (1972). "Theory of flow in unconfined aquifers considering delayed response of the water table". In: *Water Resources Research* 8.4, pp. 1031–1045. ISSN: 19447973. DOI: 10.1029/WR008i004p01031.

Neuman, Shlomo P. and Paul A. Witherspoon (1972). "Field determination of the hydraulic properties of leaky multiple aquifer systems". In: *Water Resources Research* 8.5, pp. 1284–1298. ISSN: 19447973. DOI: 10.1029/WR008i005p01284.

Neumann, Barbara et al. (2015). "Future coastal population growth and exposure to sea-level rise and coastal flooding - A global assessment". In: *PLoS ONE* 10.3. ISSN: 19326203. DOI: 10.1371/journal.pone.0118571.

Nguyen, F. et al. (2009). "Characterization of seawater intrusion using 2D electrical imaging". In: *Near Surface Geophysics* 7.5-6, pp. 377–390. ISSN: 15694445. DOI: 10.3997/1873-0604.2009025.

Niroshana Gunawardhana, Luminda and So Kazama (2009). "Tidal effects on aquifer thermal regime: An analytical solution for coastal ecosystem management". In: *Journal of Hydrology* 377.3-4, pp. 377–390. ISSN: 00221694.

DOI: 10.1016/j.jhydrol.2009.08.035. URL: http://dx.doi.org/10.1016/j.jhydrol.2009.08.035.

O'Connor, Alison E. et al. (2015). "Geochemistry of redox-sensitive trace elements in a shallow subterranean estuary". In: *Marine Chemistry* 172. ISSN: 03044203. DOI: 10.1016/j.marchem.2015.03.001.

Olivella, S. et al. (1996). "Numerical formulation for a simulator (CODE_BRIGHT) for the coupled analysis of saline media". In: *Engineering Computations (Swansea, Wales)* 13.7, pp. 87–112. ISSN: 02644401. DOI: 10.1108/02644409610151575.

Oude Essink, G. H.P., E. S. Van Baaren, and P. G.B. De Louw (2010). "Effects of climate change on coastal groundwater systems: A modeling study in the Netherlands". In: *Water Resources Research* 46.10, pp. 1–16. ISSN: 00431397. DOI: 10.1029/2009WR008719.

Palacios, Andrea et al. (2020). "Time-lapse cross-hole electrical resistivity tomography (CHERT) for monitoring seawater intrusion dynamics in a Mediterranean aquifer". In: *Hydrology and Earth System Sciences Discussions* September, pp. 1–30. ISSN: 1027-5606. DOI: 10.5194/hess-2019-408.

Pauw, P. S. et al. (2017). "Groundwater salinity patterns along the coast of the Western Netherlands and the application of cone penetration tests". In: *Journal of Hydrology* 551, pp. 756–767. ISSN: 00221694. DOI: 10.1016/j.jhydrol.2017.04.021.

Perri, M. T. et al. (2012). "A saline tracer test monitored via both surface and cross-borehole electrical resistivity tomography: Comparison of time-lapse results". In: *Journal of Applied Geophysics* 79, pp. 6–16. ISSN: 09269851. DOI: 10.1016/j.jappgeo.2011.12.011. URL: http://dx.doi.org/10.1016/j.jappgeo.2011.12.011.

Perzlmaier, S et al. (2006). "Integral seepage monitoring on open channel embankment dams by the DFOT heat pulse method". In: *Proceedings of the 74th Annual Meeting, International Commitee on Large Dams*, pp. 1–14.

Perzlmaier, Sebastian et al. (2004). "Distributed Fiber Optic Temperature Measurements in Hydraulic Engineering – Prospects of the Heat-up Method (Submitted and accepted at ICOLD Annual Meeting in Seoul 2004)". In: pp. 1–16.

Petelet-Giraud, Emmanuelle et al. (2016). "Coastal groundwater salinization: Focus on the vertical variability in a multi-layered aquifer through a multi-isotope fingerprinting (Roussillon Basin, France)." In: *The Science of the total environment* 566-567, pp. 398–415. ISSN: 1879-1026. DOI: 10.1016/j.scitotenv.2016.05.016. URL: http://www.sciencedirect.com/science/article/pii/S0048969716309214.

Pezard, Philippe A. et al. (2015). "On Baseline Determination and Gas Saturation Derivation from Downhole Electrical Monitoring of Shallow Biogenic

Gas Production". In: *Energy Procedia* 76, pp. 555–564. ISSN: 18766102. DOI: 10.1016/j.egypro.2015.07.910. URL: http://dx.doi.org/10.1016/j.egypro.2015.07.910.

Pitrak, M., S. Mares, and M. Kobr (2007). "A simple borehole dilution technique in measuring horizontal ground water flow". In: *Ground Water* 45.1, pp. 89–92. ISSN: 0017467X. DOI: 10.1111/j.1745-6584.2006.00258.x.

Pollock, Leland W. and William D. Hummon (1971). "Cyclic Changes in Interstitial Water Content, Atmospheric Exposure, and Temperature in a Marine Beach". In: *Limnology and Oceanography* 16.3, pp. 522–535. ISSN: 19395590. DOI: 10.4319/lo.1971.16.3.0522.

Pool, María, Vincent E.A. Post, and Craig T. Simmons (2014). "Effects of tidal fluctuations on mixing and spreading in coastal aquifers: Homogeneous case". In: *Water Resources Research* 50, pp. 6910–6926.

Post, V. E A (2005). "Fresh and saline groundwater interaction in coastal aquifers: Is our technology ready for the problems ahead?" In: *Hydrogeology Journal* 13.1, pp. 120–123. ISSN: 14312174. DOI: 10.1007/s10040-004-0417-2.

Post, Vincent and Elena Abarca (2010). *Préface: Interaction eau salée eau douce dans les aquifères côtiers*. DOI: 10.1007/s10040-009-0561-9.

Ramos, Gustavo et al. (2017). "A stable computation of log-derivatives from noisy drawdown data". In: *Water Resources Research* 53.9, pp. 7904–7916. ISSN: 19447973. DOI: 10.1002/2017WR020811.

Rau, Gabriel C. et al. (2014). "Heat as a tracer to quantify water flow in near-surface sediments". In: *Earth-Science Reviews* 129, pp. 40–58. ISSN: 00128252. DOI: 10.1016/j.earscirev.2013.10.015. URL: http://dx.doi.org/10.1016/j.earscirev.2013.10.015.

Raymond, J. et al. (2011). "Numerical analysis of thermal response tests with a groundwater flow and heat transfer model". In: *Renewable Energy* 36.1, pp. 315–324. ISSN: 09601481. DOI: 10.1016/j.renene.2010.06.044. URL: http://dx.doi.org/10.1016/j.renene.2010.06.044.

Re, V. et al. (2014). "Identifying the effects of human pressure on groundwater quality to support water management strategies in coastal regions: A multi-tracer and statistical approach (Bou-Areg region, Morocco)". In: *Science of The Total Environment* 500-501, pp. 211–223. ISSN: 00489697. DOI: 10.1016/j.scitotenv.2014.08.115.

Read, T. et al. (2014). "Active-distributed temperature sensing to continuously quantify vertical flow in boreholes". In: *Water Resources Research* 50.5, pp. 3706–3713. ISSN: 19447973. DOI: 10.1002/2014WR015273. arXiv: 2014WR016527 [10.1002].

Reiter, M. (2001). "Using precision temperature logs to estimate horizontal and vertical groundwater flow components". In: *Water Resources Research* 37.3, pp. 663–674. ISSN: 00431397. DOI: 10.1029/2000WR900302.

Renard, Philippe, Damian Glenz, and Miguel Mejias (2009). "Understanding diagnostic plots for well-test interpretation". In: *Hydrogeology Journal* 17.3, pp. 589–600. ISSN: 14312174. DOI: 10.1007/s10040-008-0392-0.

Rodellas, Valentí et al. (2015). "Submarine groundwater discharge as a major source of nutrients to the Mediterranean Sea". In: *Proceedings of the National Academy of Sciences* 112.13, pp. 3926–3930. ISSN: 0027-8424. DOI: 10.1073/pnas.1419049112. URL: http://www.pnas.org/lookup/doi/10.1073/pnas.1419049112.

Rodellas, Valentí et al. (2017). "Using the radium quartet to quantify submarine groundwater discharge and porewater exchange". In: *Geochimica et Cosmochimica Acta* 196, pp. 58–73. ISSN: 00167037. DOI: 10.1016/j.gca.2016.09.016.

Rosenberry, Donald O. et al. (2016). "Combined use of thermal methods and seepage meters to efficiently locate, quantify, and monitor focused groundwater discharge to a sand-bed stream". In: *Water Resources Research* 52.6, pp. 4486–4503. ISSN: 00431397. DOI: 10.1002/2016WR018808. URL: http://doi.wiley.com/10.1002/2016WR018808.

Rücker, Carsten, Thomas Günther, and Florian M. Wagner (2017). "pyGIMLi: An open-source library for modelling and inversion in geophysics". In: *Computers and Geosciences* 109.January, pp. 106–123. ISSN: 00983004. DOI: 10.1016/j.cageo.2017.07.011. URL: https://doi.org/10.1016/j.cageo.2017.07.011.

Rufí-Salís, Martí et al. (2019). "Influence of land use changes on submarine groundwater discharge". In: *Environmental Research Communications* 1.3, p. 031005. DOI: 10.1088/2515-7620/ab1695.

Russo, Stefano Lo and Glenda Taddia (2010). "Advective heat transport in an unconfined aquifer induced by the field injection of an open-loop groundwater heat pump". In: *American Journal of Environmental Sciences* 6.3, pp. 253–259. ISSN: 1553345X. DOI: 10.3844/ajessp.2010.253.259.

Saar, Martin O (2011). "Review : Geothermal heat as a tracer of large-scale groundwater fl ow and as a means to determine permeability fi elds". In: pp. 31–52. DOI: 10.1007/s10040-010-0657-2.

Sánchez-Úbeda, Juan Pedro et al. (2016). "Filtering methods in tidal-affected groundwater head measurements: Application of harmonic analysis and continuous wavelet transform". In: *Advances in Water Resources* 97, pp. 52–72. ISSN: 03091708. DOI: 10.1016/j.advwatres.2016.08.016. URL: https://linkinghub.elsevier.com/retrieve/pii/S030917081630392X.

Santos, Isaac R. et al. (2009). "Tidal pumping drives nutrient and dissolved organic matter dynamics in a Gulf of Mexico subterranean estuary". In: *Geochimica et Cosmochimica Acta* 73.5, pp. 1325–1339. ISSN: 00167037. DOI: 10.1016/j.gca.2008.11.029. URL: http://dx.doi.org/10.1016/j.gca.2008.11.029.

Sebok, E. et al. (2013). "High-resolution distributed temperature sensing to detect seasonal groundwater discharge into Lake Væng, Denmark". In: *Water Resources Research* 49.9, pp. 5355–5368. ISSN: 00431397. DOI: 10.1002/wrcr.20436.

Selker, Frank and John Selker (2018). "Investigating Water Movement Within and Near Wells Using Active Point Heating and Fiber Optic Distributed Temperature Sensing". In: *Sensors* 18.4, p. 1023. ISSN: 1424-8220. DOI: 10.3390/s18041023. URL: http://www.mdpi.com/1424-8220/18/4/1023.

Selker, John S. et al. (2006). "Distributed fiber-optic temperature sensing for hydrologic systems". In: *Water Resources Research* 42.12, n/a–n/a. ISSN: 00431397. DOI: 10.1029/2006WR005326. URL: http://doi.wiley.com/10.1029/2006WR005326.

Shanafield, M. et al. (2018). "Fiber-optic Sensing for Environmental Applications: Where We've Come From- and What's Possible?" In: *Water Resources Research*. ISSN: 00431397. DOI: 10.1029/2018WR022768. URL: http://doi.wiley.com/10.1029/2018WR022768.

Shirahata, Katsushi et al. (2016). "Digital filters to eliminate or separate tidal components in groundwater observation time-series data". In: *Japan Agricultural Research Quarterly* 50.3, pp. 241–252. ISSN: 00213551. DOI: 10.6090/jarq.50.241.

Simon, Nataline et al. (2020). "A comparison of different methods to estimate the effective spatial resolution of FO-DTS measurements achieved during sandbox experiments". In: *Sensors (Switzerland)* 20.2. ISSN: 14248220. DOI: 10.3390/s20020570.

Singha, K. et al. (2015). "Advances in interpretation of subsurface processes with time-lapse electrical imaging". In: *Hydrological Processes* 29.6, pp. 1549–1576. ISSN: 10991085. DOI: 10.1002/hyp.10280.

Slomp, Caroline P. and Philippe Van Cappellen (2004). "Nutrient inputs to the coastal ocean through submarine groundwater discharge: Controls and potential impact". In: *Journal of Hydrology* 295.1-4, pp. 64–86. ISSN: 00221694. DOI: 10.1016/j.jhydrol.2004.02.018.

Smolen, James J and Alex van der Spek (2003). *Distributed Temperature Sensing: A DTS Primer for Oil & Gas Production*. Tech. rep.

Spiteri, Claudette et al. (2008). "Flow and nutrient dynamics in a subterranean estuary (Waquoit Bay, MA, USA): Field data and reactive transport modeling". In: *Geochimica et Cosmochimica Acta* 72.14, pp. 3398–3412. ISSN: 00167037. DOI: 10.1016/j.gca.2008.04.027. URL: http://www.sciencedirect.com/science/article/pii/S0016703708002317.

Srivastava, Rajesh and Amando Guzman-Guzman (1998). "Practical Approximations of the Well Function". In: *Ground Water* 36.5. URL: https://doi.org/10.1111/j.1745-6584.1998.tb02203.x.

Stallman, R. W. (1965). "Steady one-dimensional fluid flow in a semi-infinite porous medium with sinusoidal surface temperature". In: *Journal of Geophysical Research* 70.12, pp. 2821–2827. ISSN: 0148-0227. DOI: 10.1029/JZ070i012p02821.

Stauffer, Fritz et al. (2014). *Thermal Use of Shallow Groundwater*. I. Taylor & Francis Group, LLC, p. 265. ISBN: 978-1-4665-6019-2.

Su, Huaizhi et al. (2016). "Distributed optical fiber-based theoretical and empirical methods monitoring hydraulic engineering subjected to seepage velocity". In: *Optical Fiber Technology* 31, pp. 111–125. ISSN: 10685200. DOI: 10.1016/j.yofte.2016.05.008. URL: http://dx.doi.org/10.1016/j.yofte.2016.05.008.

Taniguchi, Makoto (1993). "Evaluation of Vertical Groundwater Fluxes and Thermal Properties of Aquifers Based on Transient Temperature-Depth Profile". In: 29.7, pp. 2021–2026.

— (2000). "Evaluations of the saltwater-groundwater borehole temperature in a coastal region". In: *Geophysical Research Letters* 27.5, pp. 713–716.

Taniguchi, Makoto, Tomotoshi Ishitobi, and Jun Shimada (2006). "Dynamics of submarine groundwater discharge and freshwater-seawater interface". In: *Journal of Geophysical Research: Oceans* 111.1, pp. 1–9. ISSN: 21699291. DOI: 10.1029/2005JC002924.

Taniguchi, Makoto, Jeffrey V. Turner, and Anthony J. Smith (2003). "Evaluations of groundwater discharge rates from subsurface temperature in Cockburn Sound, Western Australia". In: *Biogeochemistry* 66.1-2, pp. 111–124. ISSN: 01682563. DOI: 10.1023/B:BIOG.0000006099.50469.b3.

Taniguchi, Makoto et al. (2019). "Submarine Groundwater Discharge: Updates on Its Measurement Techniques, Geophysical Drivers, Magnitudes, and Effects". In: *Frontiers in Environmental Science* 7.October, pp. 1–26. ISSN: 2296665X. DOI: 10.3389/fenvs.2019.00141.

Theis, Charles V. (1935). "The relation between the lowering of the Piezometric surface and the rate and duration of discharge of a well using groundwater storage". In: *Eos, Transactions American Geophysical Union* 16.2, pp. 519–

524. ISSN: 23249250. DOI: 10.1029/TR016i002p00519. arXiv: arXiv:1011.1669v3.

Tirado-Conde, Joel et al. (2019). "Evaluation of temperature profiling and seepage meter methods for quantifying submarine groundwater discharge to coastal lagoons: Impacts of saltwater intrusion and the associated thermal regime". In: *Water (Switzerland)* 11.8. ISSN: 20734441. DOI: 10.3390/w11081648.

Tombe, Bas F. des et al. (2019). "Estimation of the Variation in Specific Discharge Over Large Depth Using Distributed Temperature Sensing (DTS) Measurements of the Heat Pulse Response". In: *Water Resources Research* 55.1, pp. 811–826. ISSN: 19447973. DOI: 10.1029/2018WR024171.

Trabucchi, Michela, Jesús Carrera, and Daniel Fernàndez-Garcia (2018). "Generalizing Agarwal's Method for the Interpretation of Recovery Tests Under Non-Ideal Conditions". In: *Water Resources Research* 54.9, pp. 6393–6407. ISSN: 00431397. DOI: 10.1029/2018WR022684. URL: http://doi.wiley.com/10.1029/2018WR022684.

Trezzi, Giada et al. (2017). "Assessing the role of submarine groundwater discharge as a source of Sr to the Mediterranean Sea". In: *Geochimica et Cosmochimica Acta* 200, pp. 42–54. ISSN: 00167037. DOI: 10.1016/j.gca.2016.12.005.

Tsang, Chin-Fu, Perter Hufschmied, and Frank V. Hale (1990). "Determination of Fracture Inflow Parameters With a Borehole Fluid Conductivity Logging Method". In: *Water Resources Research* 26.4, pp. 561–578.

Tyler, Scott W. et al. (2009). "Environmental temperature sensing using Raman spectra DTS fiber-optic methods". In: *Water Resources Research* 45, pp. 1–11. ISSN: 0043-1397. DOI: 10.1029/2008WR007052.

UNEP/MAP (2015). *SUMMARY ACTIVITY REPORT 2009-2015 STRATEGIC PARTNERSHIP FOR THE MEDITERRANEAN SEA Together for the Mediterranean*. Tech. rep. Athens: UNEP/MAP.

Vallejos, A., F. Sola, and A. Pulido-Bosch (2014). "Processes Influencing Groundwater Level and the Freshwater-Saltwater Interface in a Coastal Aquifer". In: *Water Resources Management* 29.3, pp. 679–697. ISSN: 09204741. DOI: 10.1007/s11269-014-0621-3.

Vandenbohede, A., P. G.B. de Louw, and P. J. Doornenbal (2014). "Characterizing preferential groundwater discharge through boils using temperature". In: *Journal of Hydrology* 510, pp. 372–384. ISSN: 00221694. DOI: 10.1016/j.jhydrol.2014.01.006. URL: http://dx.doi.org/10.1016/j.jhydrol.2014.01.006.

Vandenbohede, Alexander and Luc Lebbe (2011). "Heat transport in a coastal groundwater flow system near De Panne, Belgium". In: *Hydrogeology Journal* 19.6, pp. 1225–1238. ISSN: 14312174. DOI: 10.1007/s10040-011-0756-8.

Vandenbohede, Alexander, A. Louwyck, and L. Lebbe (2009). "Conservative solute versus heat transport in porous media during push-pull tests". In: *Transport in Porous Media* 76.2, pp. 265–287. ISSN: 01693913. DOI: 10.1007/s11242-008-9246-4.

Vargas-Yáñez, M. et al. (2017). "Updating temperature and salinity mean values and trends in the Western Mediterranean: The RADMED project". In: *Progress in Oceanography* 157.August, pp. 27–46. ISSN: 00796611. DOI: 10.1016/j.pocean.2017.09.004. URL: http://dx.doi.org/10.1016/j.pocean.2017.09.004.

Vogt, Tobias et al. (2010). "Estimation of seepage rates in a losing stream by means of fiber-optic high-resolution vertical temperature profiling". In: *Journal of Hydrology* 380.1-2, pp. 154–164. ISSN: 0022-1694. DOI: 10.1016/j.jhydrol.2009.10.033. URL: http://dx.doi.org/10.1016/j.jhydrol.2009.10.033.

Wagner, Valentin et al. (2013). "Geothermics Analytical approach to groundwater-influenced thermal response tests of grouted borehole heat exchangers". In: *Geothermics* 46, pp. 22–31. ISSN: 0375-6505. DOI: 10.1016/j.geothermics.2012.10.005. URL: http://dx.doi.org/10.1016/j.geothermics.2012.10.005.

Werner, Adrian D. (2017). "On the classification of seawater intrusion". In: *Journal of Hydrology* 551, pp. 619–631. ISSN: 00221694. DOI: 10.1016/j.jhydrol.2016.12.012. URL: http://dx.doi.org/10.1016/j.jhydrol.2016.12.012.

Werner, Adrian D. et al. (2013). "Seawater intrusion processes, investigation and management: Recent advances and future challenges". In: *Advances in Water Resources* 51, pp. 3–26. DOI: 10.1016/j.advwatres.2012.03.004.

Wilson, Keith (1983). "Beach sediment temperature variations through depth and time". In: *Estuarine, Coastal and Shelf Science* 17.5, pp. 581–586. ISSN: 02727714. DOI: 10.1016/0272-7714(83)90010-0.

Windom, Herbert L. et al. (2006). "Submarine groundwater discharge: A large, previously unrecognized source of dissolved iron to the South Atlantic Ocean". In: *Marine Chemistry* 102.3-4, pp. 252–266. ISSN: 03044203. DOI: 10.1016/j.marchem.2006.06.016. URL: http://www.sciencedirect.com/science/article/pii/S0304420306001198.

Yates, D.N. (1996). "An Integrated Water Balance Model for Climate Impact Assessment of River Basin Runoff". In: *International Journal of Water Resources Development* 12(2), pp. 121–140. DOI: 10.1080/07900629650041902.

Zarroca, Mario et al. (2014). "Delineating coastal groundwater discharge processes in a wetland area by means of electrical resistivity imaging, 224Ra and 222Rn". In: *Hydrological Processes* 28.4, pp. 2382–2395. ISSN: 08856087. DOI: 10.1002/hyp.9793.

Zhou, Pengpeng, Xiaojuan Qiao, and Xiaolei Li (2017). "Numerical modeling of the effects of pumping on tide-induced groundwater level fluctuation and on the accuracy of the aquifer's hydraulic parameters estimated via tidal method: a case study in Donghai Island, China". In: *Journal of Hydroinformatics* 19.4, pp. 607–619. ISSN: 1464-7141. DOI: 10.2166/hydro.2017.089. URL: https://iwaponline.com/jh/article/19/4/607-619/3659.

Ziagos, J. P. and D. D. Blackwell (1986). "A model for the transient temperature effects of horizontal fluid flow in geothermal systems". In: *Journal of Volcanology and Geothermal Research* 27.3-4, pp. 371–397. ISSN: 03770273. DOI: 10.1016/0377-0273(86)90021-1.